Title
Device architecture and characterization of organic and hybrid perovskite photovoltaic

Author
Yang, Yang

Publication Date
2015

Peer reviewed|Thesis/dissertation

UNIVERSITY OF CALIFORNIA

Los Angeles

Device architecture and characterization of organic and hybrid perovskite photovoltaic

A dissertation submitted in partial satisfaction of the

requirements for the degree Doctor of Philosophy

in Materials Science and Engineering

by

Yang Yang

2015

ABSTRACT OF THE DISSERTATION

Device architecture and characterization of organic and hybrid perovskite photovoltaic
by

Yang Yang

Doctor of Philosophy in Materials Science and Engineering

University of California, Los Angeles, 2015

Professor Yang Yang, Chair

Photovoltaic (PV), which converts sunlight into electricity, is a promising solution to the energy and environmental crisis we are facing right now. In this dissertation, we are focusing on next generation semiconductors as the photoactive materials, i.e. organic and orgainic/inorganic hybrid perovskite semiconductors, to achieve cost effective and energy efficient solar cell technology.

Organic semiconductor always shows narrow absorption compared with the conventional inorganic semiconductors, which is one of the limiting factors of the organic photovoltaic (OPV). In the second chapter, we solve this problem by employing the multi-absorber bulk heterojunction (BHJ) device architecture, in which different polymer absorbers are blended together to cover panchromatic absorption. A comparison study reveals the working mechanism of this novel device, and the material selection rule is summarized. Eventually, the 8.7% power conversion efficiency is realized in ternary BHJ solar cell. Besides the narrow absorption, the organic BHJ layer is usually very thin (~100 nm) due to its limited carrier mobility, hence the absorption is insufficient in the

photoactive layer. In the third chapter, we utilize the plasmonic effect of the metal nanoparticle to enhance the absorption of the OPVs. The addition of spectrally tuned SiO_2-Au nanorods leads to improved photocurrent and device efficiency. On the other hand, the narrow absorption of organic materials also creates new device possibility that traditional semiconductor can't deliver. One of the good examples is the visibly semitransparent solar cell. In the fourth chapter, we develop this idea by engineering transparent top electrode and incorporate photonic distributed bragg reflector to further improve the device efficiency without compromising the visible transparency.

Organic/inorganic hybrid perovskite semiconductor attracts incredible attentions in the past few years. It originates from the excitonic semiconductor family but delivers superior photovoltaic device performance than the typical excitonic solar cell e.g. dye sensitized solar cells and organic solar cells. However, the photophysics of this type of material is still mysterious in many aspects. In the fifth chapter, we try to understand its photophysical property by some basic characterization methods. We discover that the photo excitations in this materials varies with different crystal size. Besides, we observe the photoluminescence lifetime and intensity improve dramatically after exposing to the moisture. The improved photophysical property eventually results in greatly enhanced photovoltaic device performance. In addition to the solar cell, we successfully demonstrates the ultra high photodetectivity based on the perovskite materials, the results are included in sixth chapter.

The dissertation of Yang Yang is approved.

Dwight C. Streit

Eric Pei-Yu Chiou

Yang Yang, Committee Chair

University of California, Los Angeles

2015

Table of Contents

List of Figures

List of tables

Acknowledgments

The dissertation and the work were completed with the selfless support and guidance of many. I would like to express my deep appreciation to them and my sincere wish that even though the dissertation has come to a conclusion our friendships continue to thrive.

Firstly, I sincerely thank Prof. Yang Yang, my Ph.D. research advisor, for the opportunity to participate the extraordinary research in his group. His guidelines of taking challenge in research as well as solving the real-world problem, not only encourage my Ph.D. research but also build up my scientific tasty, which I will pass to my students if I become a faculty one day.

I also would like to thank my committee members, Prof. Dwight Streit , Prof. Eric Pei-Yu Chiou, and Prof. Mark Goorsky, for their mentorship.

I thank Dr. Wei lek Kwan, my junior mentor when I was doing the summer research intern in YYlab. I am lucky to meet such a role model in the early stage of my voyage. I also thank lots of former group member who helped and inspired me, Dr. Ankit kumar, Dr. Jun Yang, Dr. Srinivas Sista, Dr. Lei Bao, Dr. Hsiang-Yu Chen and so many others.

I also want to thank Prof. Yongfang Li in Chinese Academy Sciences for giving me the opportunity to join his group during 2009 to 2010. I spend a really happy year in Beijing and learned a lot of Chemistry knowledge from him and the senior students in his group: Dr. Yi Yang, Dr. Guangjin Zhao, and Dr. Haizheng Zhong and many others. It is a valuable experience for me to prepare for my Ph.D. study later in UCLA.

I will never forget and thank those senior group members in the YY Lab during my Ph.D. career: Dr. Gang Li, Dr. Ziruo Hong, Dr. Jingbi You, Dr.You Seung Rim, Dr. Min Cai, Dr. Zheng Xu, Dr. Rui Zhu, Dr. Qi Chen, Dr. Huanping Zhou, Dr. Chengyang Jiang, Dr. Shirong Lu, Dr. Youjun He, Dr. Lijun Huo, Dr. Wenbing Yang, Dr. Choong-Heui Chung, Dr. Peter Li, Dr. Kitty Cha, Dr.Samuel Duan, Dr. Brion Bob, Dr. Letian Dou, Dr. Wan-Ching Hsu, Dr. Eric Richard, Dr. Jing Gao and Ms. Renee.

I am glad that we have the chance to share the joys and hard times together with my fellow colleges: Tze-Bing Song, Chia-Jung Hsu, Johnny Chen, Steve, Shenglin Ye, Lei Meng, Peter Sun Jase Chang, Golden Chen, and all the others. I wish them the best of their career and life.

I feel grateful to have many caring friends and my roommates that we share so many unforgettable moments together.

At last, I thank my parents, my grandparents, my aunts, my uncles, my brothers and sisters, and my family members. I would not have reached this step without their belief in me.

VITA

2005.9-2009.7 B.E. in Electrical Engineering (System and Control), Minor in advanced honor class of engineering (Chu kochen honors college), Zhejiang University, Hangzhou, Zhejiang, China.

2008.7-2008.9

2009.2-2009.6 CSST-UCLA visiting student, Department of Materials Science and Engineering, University of California, Los Angeles, CA, USA. (Advisor : Prof.Yang Yang)

2009.8-2010.7 Research Intern, Institute of Chemistry, Chinese Academy of Sciences, Beijing, China. (Advisor : Prof. Yongfang Li)

2010.9-2015.3 Graduate Student Researcher, Department of Materials Science and Engineering, University of California, Los Angeles, CA, USA. (Advisor : Prof.Yang Yang)

Publications

1. You Seung Rim,⊥ **Yang (Micheal) Yang**⊥, Sang-Hoon Bae⊥, Huajun Chen, Jaemyung Kim, Chao Li, Paul S. Weiss, Mark S. Goorsky, and Yang Yang. "Ultra-High and Broad Spectral Photodetectivity of Organic–Inorganic Hybrid Phototransistor for Transparent Wearable Electronics" *In preparation*. (⊥Equal-author contributors)

2. **Yang (Michael) Yang**, Qi Chen, Chun-Chiang Kuo, Tze-Bin Song, Yao-Tsung Hsieh, Lei Meng, Jingbi You, Ziruo Hong, Huanping, Zhou, Yang Yang. "Metal/dielectric/metal transparent top electrode for semitransparent perovskite and perovskite/CIGS 4-terminal tandem solar cells" *In preparation*.

3. **Yang (Michael) Yang,** Ziruo Hong, Pengyu Sun, Yang Yang "Smart photon management for visibly transparent organic solar cells " *In preparation*

4. **Yang (Michael) Yang**, Wei Chen, Letian Dou, Wei-Hsuan Chang, Hsin-Sheng Duan, Brion Bob, Gang Li, and Yang Yang. "High-performance multiple-donor bulk heterojunction solar cells." *Nature Photonics* (2015).

5. Chang, Wei-Hsuan, Lei Meng, Letian Dou, Jingbi You, Chun-Chao Chen, **Yang (Michael) Yang**, Eric Patrick Young, Gang Li, and Yang Yang. "A Selenophene Containing Benzodithiophene-alt-thienothiophene Polymer for Additive-Free High Performance Solar Cell." *Macromolecules* (2015).

6. Song, Tze-Bin, Qi Chen, Huanping Zhou, Song Luo, **Yang (Michael) Yang**, Jingbi You, and Yang Yang. "Unraveling film Transformations and device performance of planar perovskite solar cells." *Nano Energy* (2015)

7. Dou, Letian,⊥ **Yang (Micheal) Yang**,⊥ Jingbi You, Ziruo Hong, Wei-Hsuan Chang, Gang Li, and Yang Yang. "Solution-processed hybrid perovskite photodetectors with high detectivity." *Nature communications* 5 (2014). **(⊥Equal-author contributors)**

8. You, Jingbi, **Yang (Michael) Yang**, Ziruo Hong, Tze-Bin Song, Lei Meng, Yongsheng Liu, Chengyang Jiang et al. "Moisture assisted perovskite film growth for high performance solar cells." *Applied Physics Letters* 105, no. 18 (2014): 183902.

9. Liu, Yongsheng, Ziruo Hong, Qi Chen, Wei-Hsuan Chang, Huanping Zhou, Tze-Bin Song, Eric Young, **Yang (Michael) Yang,** Jingbi You, Yang Yang et al. "Integrated Perovskite/Bulk-Heterojunction toward Efficient Solar Cells." *Nano letters* (2014).

10. Song, Tze-Bin, Yu Chen, Choong-Heui Chung, **Yang (Michael) Yang**, Brion Bob, Hsin-Sheng Duan, Gang Li, King-Ning Tu, Yu Huang, and Yang Yang. "Nanoscale joule heating and electromigration enhanced ripening of silver nanowire contacts." *ACS nano* 8, no. 3, 2804-2811. (2014)

11. You, Jingbi, Ziruo Hong, **Yang (Michael) Yang,** Qi Chen, Min Cai, Tze-Bin Song, Chun-Chao Chen et al. "Low-temperature solution-processed perovskite solar cells with high efficiency and flexibility." *ACS nano* (2014).

12. Lee, Dong-Hyun, **Yang (Michael) Yang**, Jingbi You, Eric Richard, and Gang Li. "Immiscible solvents enabled nanostructure formation for efficient polymer photovoltaic cells." *Nanotechnology* 25, no. 29 (2014): 295401.

13. Jankovic, Vladan, ⊥ **Yang (Michael) Yang**⊥, Jingbi You, Letian Dou, Yongsheng Liu, Puilam Cheung, Jane P. Chang, and Yang Yang. "Active layer-incorporated, spectrally tuned Au/SiO2 core/shell nanorod-based light trapping for organic photovoltaics." *ACS nano* 7, no. 5 3815-3822. (2013) **(⊥Equal-author contributors)**

14. Liu, Yongsheng, **Yang (Michael) Yang**, Chun-Chao Chen, Qi Chen, Letian Dou, Ziruo Hong, Gang Li, and Yang Yang. "Solution-Processed Small Molecules Using

Different Electron Linkers for High-Performance Solar Cells." *Advanced Materials* 25, no. 33 4657-4662. (2013)

15. Liu, Yongsheng, Chun-Chao Chen, Ziruo Hong, Jing Gao, **Yang (Michael) Yang**, Huanping Zhou, Letian Dou, Gang Li, and Yang Yang. "Solution-processed small-molecule solar cells: breaking the 10% power conversion efficiency." *Scientific reports* 3 (2013).

16. **Yang, Yang**, Haizheng Zhong, Zelong Bai, Bingsuo Zou, Yongfang Li, and Gregory D. Scholes. "Transition from Photoconductivity to Photovoltaic Effect in P3HT/CuInSe2 Composites." *The Journal of Physical Chemistry C* 116, no. 13 7280-7286. (2012)

17. Chen, Dugang, **Yang Yang**, Cheng Zhong, Zhengran Yi, Fei Wu, Li Qu, Yu Li, Yongfang Li, and Jingui Qin. "Synthesis and photovoltaic properties of two-dimensional D-A copolymers with conjugated side chains." *Journal of Polymer Science Part A: Polymer Chemistry* 49, no. 17 3852-3862. (2011)

18. Zhang, Zhi-Guo, **Yang Yang**, Siyuan Zhang, Jie Min, Jing Zhang, Maojie Zhang, Xia Guo, and Yongfang Li. "Effect of acceptor substituents on photophysical and photovoltaic properties of triphenylamine–carbazole alternating copolymers." *Synthetic Metals* 161, no. 13 1383-1389. (2011)

19. Zhang, Maojie, Haijun Fan, Xia Guo, **Yang Yang**, Shanshan Wang, Zhi-Guo Zhang, Jing Zhang, Xiaowei Zhan, and Yongfang Li. "Synthesis and photovoltaic properties of copolymers based on bithiophene and bithiazole."*Journal of Polymer Science Part A: Polymer Chemistry* 49, no. 12 2746-2754. (2011)

20. Deng, Dan, **Yang Yang,** Jing Zhang, Chang He, Maojie Zhang, Zhi-Guo Zhang, Zhanjun Zhang, and Yongfang Li. "Triphenylamine-containing linear DAD molecules with benzothiadiazole as acceptor unit for bulk-heterojunction organic solar cells." *Organic Electronics* 12, no. 4 614-622. (2011)

21. Zhang, Maojie, Xia Guo, **Yang Yang**, Jing Zhang, Zhi-Guo Zhang, and Yongfang Li. "Downwards tuning the HOMO level of polythiophene by carboxylate substitution for high open-circuit-voltage polymer solar cells." *Polymer Chemistry* 2, no. 12 2900-2906. (2011)

22. Zhang, Zhi-Guo, Yi-Liang Liu, **Yang Yang**, Keyue Hou, Bo Peng, Guangjin Zhao, Maojie Zhang, Xia Guo, En-Tang Kang, and Yongfang Li. "Alternating copolymers of carbazole and triphenylamine with conjugated side chain attaching acceptor groups: synthesis and photovoltaic application." *Macromolecules* 43, no. 22 9376-9383. (2010)

Chapter 1 Introduction of organic and hybrid perovskite solar cells

1.1 Background of organic solar cells

Photovoltaic (PV), which converts sunlight into electricity, is a promising solution to the energy and environmental crisis we are facing right now. Up to now, various inorganic semiconducting materials based PVs dominates the market. However, this technology is not fully replacing the rigid-electricity due to its high cost. While on the other hand，there has been growing interest in organic-based PV (OPV) technology in recent years. Organic semiconductors show great promise owing to its possibility of producing lightweight, flexible, easily manufactured, and inexpensive solar cells.[1,2]

Brief history of the OPV research: The first promising OPV device was reported in1986 by Tang *et al.* with bi-layer structure. [3] A thin layers of p-type small molecules (copper phthalocyanine) and n-type molecules (perylenediimide derivative) were thermally evaporated as two layer heterojunction sandwiched between two electrodes. It is found that the charge separation at the donor-acceptor interface was very efficient. The device shows an overall power conversion efficiency (PCE) of ~1%. [3] Later in the early 1990s, Heeger, Sariciftci *et al*. [4] firstly discovered efficient electron transfer from polymer to fullerene. The photo-induced electron transfer from the conjugated polymer donor (MEH-PPV) to fullerene acceptor (C60) was found to be~ 50 fs, it opened new possibility of using conjugated polymers as the donor and fullerenes as the acceptor in the OPV devices.[4] Due to the short lifetime and limited diffusion length of the exciton, the active layer must be thin enough to ensure the electron and hole can be separately collected before recombination. To overcome the limitation, the bulk heterojunction (BHJ) structure made

from a mixing of p- and n-type materials was invented by Sariciftci and Heeger in a 1992 patent, [5] followed by two important papers by Heeger *et al*. and Friend *et al*., respectively. [6,7]. Much efficient solar cell was achieved by adopting this structure, since it overcomes the limitation of the limited diffusion length of the holes and electrons. After that the BHJ has become the standard OPV architecture and the morphology control of the donor acceptor phase separation is one of the key research directions in this filed. In the recent ten years, the OPV device efficiency is largely pushed through new materials designs. [8-11] The tandem solar cell device employing two BHJ devices vertically stacked together also create new possibility to further improve the state of art of the OPV technology. [12,13]

OPV Working mechanism. The common device geometry and energy band configuration are illustrated in Figure 1.1.

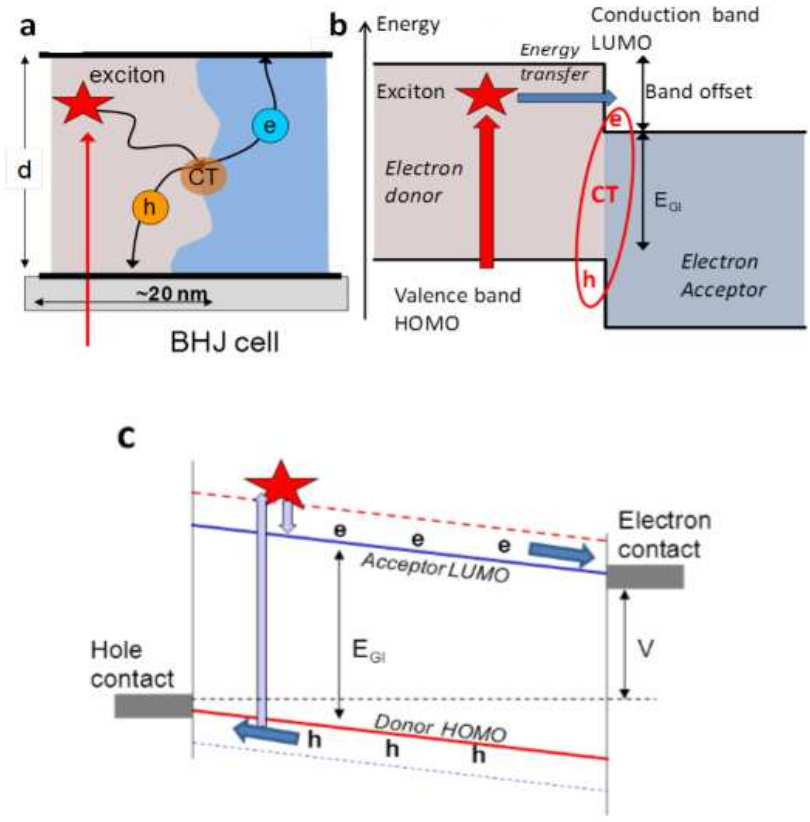

Figure 1-1 Basic geometry and electronic stricture of the BHJ cell. (a) The nanoscale phase-separated domain morphology showing exciton absorption leading to the charge transfer state that separates into mobile electrons and holes. (b) The same process illustrated in an energy diagram showing the band offset between the donor and acceptor materials. (c) Schematic of solar cell current fl ow at voltage bias V. Figure reproduced with permission from: ref. 14, ©2013 WILEY-VCH Verlag GmbH & Co. KGaA, Weinheim

The optically excited excitons in the organic semiconductor are too tightly bound with exciton binding energy far beyond the characteristic thermal energy at room temperature (26 meV). The exciton can't be dissociated into free electrons and holes by thermal excitation unless they are close to the donor acceptor interface. The interface band gap E_{GI} is defined as the energy difference between the valence band (or HOMO) of the donor and the conduction band (or LUMO) of the acceptor. Provided that E_{GI} is less than the exciton energy, it is energetically favorable for the exciton to be separated into an electron in the acceptor and a hole remaining in the donor. This intermediate state is known as the charge transfer (CT) state, from which free electrons and holes are generated eventually. An important unresolved question is how small an energy difference between the exciton energy and E_{GI} can maintain efficient charge separation, since the energy difference represents a significant loss of cell efficiency. [14] It is not clear whether the tightly bound excitons reach the donor/acceptor interface by exciton diffusion or by energy transfer, however in either case, their range is only a few 10 s of nanometers. Therefore, the BHJ structure is essential to achieve the high efficiency OPVs, and the nanoscale phase separation is critical. Fortunately, such sophisticated phase separation occurs spontaneously in a wide range of OPV materials. The exciton reaches the donor acceptor interface within 1 ps,[14] and the geminate recombination is almost completely suppressed. One of the major unsolved question of OPV mechanism is what is the driving for charger dissociation from CT states to free carriers.[14] There are several relevant works report that

mobile free carriers are produced by hot-exciton dissociation. Excitations at energies much higher than the optical band gap may be an important route for dissociation of the bound electron–hole pair.[15,16] Nevertheless, Salleo and co-workers also demonstrated that photo carrier generation in the relaxed CT state is just as efficient as in the higher energy states. [17] It indicates that the charge carriers tend to be separated, not bound at equilibrium.[18] However, the charge generation process in OPVs is still under debating, and it is one of the fundamental mystery in this field.

1.2 Background of hybrid perovskite solar cells

The recent advent of organometallic lead halide perovskite solar cells has produced some of the most rapid growth in cell performance of any material in photovoltaic history.[19-21] The unique properties of these absorber layers provide a number of advantages in optoelectronic applications that in many ways originate from the nature of the perovskite lattice.[22-24] The exclusive use of widely available elements and the capacity for film deposition through either solution or vacuum-based methods is an indication of the tremendous potential of these compounds to completely redefine the way that materials are designed and chosen for electronic device applications. The scope of this review is to summarize the notable achievements in hybrid perovskite film formation: 1) Film formation methods, 2) Techniques to tune film properties, and 3) Cell architecture, performance, and optimization. Perovskite materials follow the general formula ABX3 and adopt the same crystal structure as calciumtitanate. In this arrangement, the ‘A’ and ‘B’ cations coordinate with 12 and 6 ‘X’ anions, forming cuboctahedral and octahedral geometries, respectively (shown in Figure 1.2).

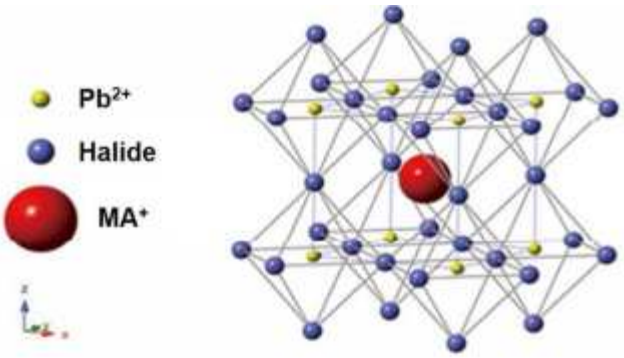

Figure 1-2 Chemical structure of the organic/inorganic hybrid halide perovskite

The tendency of a compound toward perovskite formation can be estimated using the Goldschmidt tolerance factor,8 although determining the chemical and thermal stability of the resulting structure invariably requires more detailed analysis. The perovskite material family exhibits a wide range of electronic behavior including piezoelectric, thermoelectric, semiconducting, and superconducting properties depending on the specifics of the measured material. In the early 1990s, Mitzi and coworkers made an extensive investigation into the optoelectronic properties of organometallic halide perovskites, where the 'A' sites are occupied by organic cations, the 'B' sites are occupied by group IV cations (Sn, Pb), and the 'X' sites are occupied by group VII anions (Cl, Br, I).[25-28] Lead halide perovskite solar cells are rapidly approaching 20% power conversion efficiency (PCE) after only 5 years of concerted development, an achievement that required decades of effort for conventional materials. [19-21] The most successful perovskite materials thus far are variations on the compound CH3NH3PbX3 (X=Cl, Br, I), which exhibits the most attractive properties of ideal PV absorbers: 1) Strong optical absorption due to s-p anti-bonding coupling; 2) High electron and hole mobilities and diffusion lengths; 3) Superior structural defect tolerance and shallow point defects; and 4) Low surface recombination

velocity and benign grain boundary effects.[29-32] The hybrid organic-inorganic nature of halide perovskites has allowed this class of materials to capitalize on the previous development of Dye-Sensitized Solar Cells (DSSCs), organic photovoltaics, and other thin film material systems.[33-36] In a typical cell architecture, a perovskite absorber layer with a thickness of several hundred nanometers is sandwiched between an electron and hole transport layer (ETL and HTL).[37-39] When the device is illuminated, carriers are created in the absorber, extracted by the ETL and HTL and collected at the appropriate electrodes. The work required for establishing a rational guide for fabricating high quality absorber layers is still underway, and is made more difficult by the unique characteristics of perovskite films in the context of their materials chemistry and physics. Additional efforts related to connecting the structure and composition of perovskite absorbers to their electronic properties and device performance are particularly valuable in enhancing our understanding of how to process and deposit films formed from this material family.

1.3 References

1. S. Gunes, H. Neugebauer, N. S. Sariciftci, Chem. Rev. 2007, 107, 1324..

2. T. A. Skotheim, J. Reynolds, Conjugated Polymers: Processing and Applications, CRC Press, 2007.

3. C. W. Tang, Appl. Phys. Lett. 1986, 48, 183

4. N. S. Sariciftci, L. Smilowitz, A. J. Heeger, F. Wudl, Science 1992, 258 , 1474.

5. A. J. Heeger, N. S. Sariciftci, Patent US 1992/5331183 A.

6. G. Yu, J. Gao, J. C. Hummelen, F. Wudl, A. J. Heeger, Science 1995, 270 , 1789.

7. J. J. M. Halls, C. A. Walsh, N. C. Greenham, E. A. Marseglia, R. H. Friend, S. C. Moratti, A. B. Holmes, Nature 1995, 376, 498.

8. C.-Y. Chang, C.-E. Wu, S.-Y. Chen, C. Cui, Y.-J. Cheng, C.-S. Hsu,Y.-L. Wang, Y. Li, Angew. Chem. Int. Ed. 2011, 50, 9386

9. Liang, Yongye, Zheng Xu, Jiangbin Xia, Szu-Ting Tsai, Yue Wu, Gang Li, Claire Ray, and Luping Yu, Advanced Materials 2010, 22, 20, 135-138.

10. Jingbi You, Letian Dou, Ken Yoshimura, Takehito Kato, Kenichiro Ohya, Tom Moriarty, Keith Emery, Chun-Chao Chen, Jing Gao, Gang Li and Yang Yang Nature Communications 2013, 4, 1446.

11. Letian Dou, Wei-Hsuan Chang, Jing Gao, Chun-Chao Chen, Jingbi You and Yang Yang; Advanced Materials 2013, 25, 825-831.

12. Letian Dou, Jingbi You, Jun Yang, Chun-Chao Chen, Youjun He, Seiichiro Murase, Tom Moriarty, Keith Emery, Gang Li and Yang Yang; Nature Photonics 2012, 6, 180-185.

13. Jingbi You, Letian Dou, Ziruo Hong, Gang Li, Yang Yang; Progress in Polymer Science 2013, 38, 1909-1928.

14. L. Dou, J. You, Z. Hong, Z. Xu, G. Li, R. A. Street, Y. Yang, Adv. Mater. 2013, 25, 6642.

15. Grancini, G., Maiuri, M., Fazzi, D., Petrozza, A., Egelhaaf, H. J., Brida, D.,& Lanzani, G. (2013). Nature materials, 12(1), 29-33.

16. Gélinas, S., Rao, A., Kumar, A., Smith, S. L., Chin, A. W., Clark, J., & Friend, R. H. (2014). Science, 343(6170), 512-516.

17. Vandewal, K., Albrecht, S., Hoke, E. T., Graham, K. R., Widmer, J., Douglas, J. D., & Salleo, A. (2014). Nature materials, 13(1), 63-68.

18. Song, Y., Clafton, S. N., Pensack, R. D., Kee, T. W., & Scholes, G. D. (2014). Nature communications, 5.

19. http://www.nrel.gov/ncpv/images/efficiency_chart.jpg.

20. H. J. Snaith, J. Phys. Chem. Lett., 2013, 4, 3623-3630.

21. M. A. Green, K. Emery, Y. Hishikawa, W. Warta and E. D. Dunlop, Prog. Photovoltaics., 2014, 22, 1-9.

22. S. Sun, T. Salim, N. Mathews, M. Duchamp, C. Boothroyd, G. Xing, T. C. Sum and Y. M. Lam, Energy Environ. Sci., 2014, 7, 399-407. 5.

23. C. Wehrenfennig, M. Liu, H. J. Snaith, M. B. Johnston and L. M. Herz, J. Phys. Chem. Lett., 2014, 5, 1300-1306.

24. G. Xing, N. Mathews, S. Sun, S. S. Lim, Y. M. Lam, M. Grätzel, S. Mhaisalkar and T. C. Sum, Science, 2013, 342, 344-347.

25. Z. Ku, Y. Rong, M. Xu, T. Liu and H. Han, Sci. Rep., 2013, 3, 3132.

26. J. Mats and L. Peter, J. Phys.: Condens. Matter, 2008, 20, 264001.

27. D. V. Taylor and D. Damjanovic, Appl. Phys. Lett., 2000, 76, 1615-1617.

28. J. Hejtmánek, Z. Jirák, M. Maryško, C. Martin, A. Maignan, M. Hervieu and B. Raveau, Phys. Rev. B, 1999, 60, 14057-14065.

29. W.-J. Yin, T. Shi and Y. Yan, Adv. Mater., 2014, 26, 4653-4658.

30. H. J. Snaith and M. Gratzel, Adv. Mater., 2007, 19, 3643-3647.

31. J. Even, L. Pedesseau and C. Katan, Proc. SPIE, Photonics Sol. Energy Syst. V, 91400Y (May 15, 2014).

32. J. Kim, S.-H. Lee, J. H. Lee and K.-H. Hong, J. Phys. Chem. Lett., 2014, 5, 1312-1317.

33. P. Docampo, S. Guldin, T. Leijtens, N. K. Noel, U. Steiner and H. J. Snaith, Adv. Mater., 2014, 34, 4013-4030.

34. K. L. Chopra, P. D. Paulson and V. Dutta, Prog. Photovoltaics, 2004, 12, 69-92.

35. L. Dou, J. You, Z. Hong, Z. Xu, G. Li, R. A. Street and Y. Yang, Adv. Mater., 2013, 25, 6642-6671.

36. H. Zhou, Weeen.-C. Hsu, H.-S. Duan, B. Bob, W. Yang, T.-B. Song, C.-J. Hsu and Y. Yang, Energy Environ. Sci., 2013, 6, 2822-2838.

37. S. Lv, L. Han, J. Xiao, L. Zhu, J. Shi, H. Wei, Y. Xu, J. Dong, X. Xu, D. Li, S. Wang, Y. Luo, Q. Meng and X. Li, Chem. Commun., 2014, 50, 6931-6934.

38. J. M. Ball, M. M. Lee, A. Hey and H. J. Snaith, Energy Environ. Sci., 2013, 6, 1739-1743.

39. A. Marchioro, J. Teuscher, D. Friedrich, M. Kunst, R. van de Krol, T. Moehl, M. Gratzel and J.-E. Moser, Nat. Photonics, 2014, 8, 250-255

Chapter 2 Multi-absorber Bulk heterojunction solar cells

Broadening the absorption bandwidth of polymer solar cells by incorporating multiple absorber donors into the bulk-heterojunction (BHJ) active layer is an attractive means of resolving the narrow absorption of organic semiconductors. However, this leads to a much more complicated system, and previous efforts have met with limited success. In this manuscript, several dual-donor and multi-donor BHJ polymer solar cells based on a material pool with different absorption ranges and preferred molecular structures were studied. The study shows clearly that compatible polymer donors can coexist harmoniously, but the mixing of incompatible polymers can lead to severe molecular disorder and limit the device performance. These results provide guidance for the general use of multiple-donor BHJ to overcome the absorption limitation, achieve both high performance and fabrication simplicity for organic solar cell.

2.1 Objective and experimental design

Polymer photovoltaic cells have shown great potential as a means to harvest solar energy in a highly processable and cost-effective manner[1-5]. Typical organic solar cells consist of a mixture of a polymer (or organic small molecule) donor and C-60 derivative acceptor as the photo-active layer. In bulk-heterojunction (BHJ) organic solar cells, the absorbed incident photons generate tightly bound electron-hole pairs, which are then dissociated into electrons and holes at the nearby donor/acceptor interface. The electrons and holes are then transported to their respective electrodes[6-8].

Research efforts in the last decade or so have significantly improved organic solar cell performance[9-14], and power conversion efficiency (PCE) values beyond 10% have recently been achieved[15-16]. Over the years, significant research efforts have been put into developing low band gap polymers to extend the absorption and harvest more solar energy. Nevertheless, unlike the continuous band structure of inorganic semiconductors like Si, the molecular orbital energy level of organic or polymeric semiconductor is narrow, which makes it challenging to obtain the panchromatic absorption coverage with a single organic semiconductor**.** (Figure.2.1)

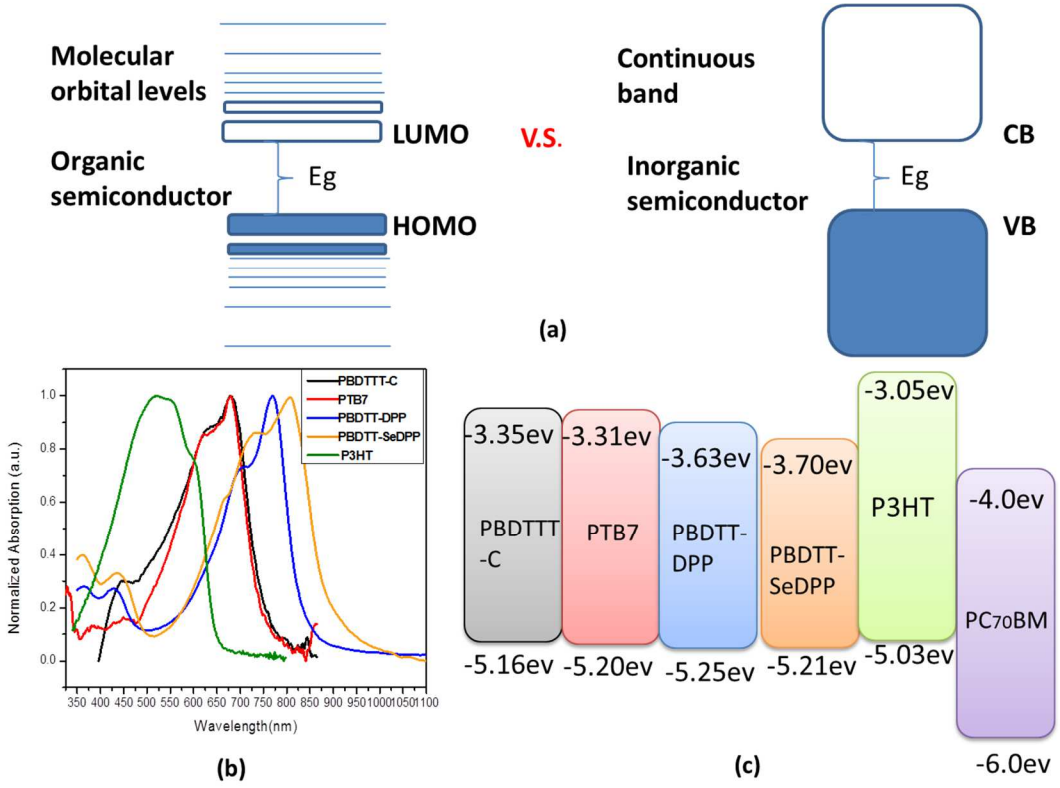

Figure 2-1 Band structure, band position, and absorption spectrum of the model materials used. (a) General schematic of band structure of organic/polymeric and inorganic semiconductors; (b) absorption spectra and (c) energy band diagrams of the material pool.

This is one of the reasons that polymer solar cells invariably exhibit low short circuit current (Jsc), compared with commercial inorganic solar cells. In addition, it has been very

difficult to achieve as high an external quantum efficiency (EQE) in low band gap polymer systems (E_g < 1.4 eV) as in traditional polymer systems such as poly(3-hexyl thiophene) (P3HT) with reported EQE values of over 70%[17]. Even with their imperfect characters, this rich set of low band gap polymers are very valuable in improving state-of-art polymer solar cells if we can design OPV devices with multiple compatible polymers to expand the absorption range while at the same time maintaining other key parameters, such as open circuit voltage (Voc) and fill factor (FF).

Unfortunately, very few successful ternary BHJ polymer photovoltaic cell structures have been reported that surpass the efficiency of their corresponding binary BHJ devices[23]. The ideal scenario is that the multiple polymers will work independently. However, in reality the interactions between the two polymers are inevitable due to their different chemical and physical natures. These unfavorable interactions might function as "morphological traps" and recombination centers, which lead to reduced photovoltaic performance in the complex multiple-donor BHJ system. Recent progress in the development of new photovoltaic materials has made available a wide pool of high performance donor polymers with different absorption ranges that have widely used in OPV research, for example: poly[4,8-bis-substituted-benzo[1,2-b:4,5-b0]dithiophene-2,6-diyl-alt-4-substituted-thieno[3,4-b]thiophene-2,6-diyl] (PBDTTT-C) with E_g =1.60eV; poly{2,6-4,8-di(5ethylhexylthienyl) benzo[1,2-b;3,4-b] dithiophene-alt-5-dibutyloctyl-3,6-bis(5-bromothiophen-2-yl)pyrrolo[3,4-c]pyrrole-1,4-dione} (PBDTT-DPP) with E_g =1.46 eV; poly{4,6-(2-ethylhexyl-3-fluorothieno[3,4-b]thiophene-2-carboxylate)alt-2,6(4,8-bis(2-ethylhexyloxy)benzo[1,2-b:4,5-b]dithiophene)} (PTB7) with E_g = 1.62 eV; (poly{2,6′-4,8-di(5-ethylhexylthienyl) benzo[1,2-b;3,4-b]dithiophene-alt-2,5-bis(2-

butyloctyl)-3,6-bis(selenophene-2-yl)pyrrolo[3,4-c]pyrrole-1,4-dione} (PBDTT-SeDPP) with E_g = 1.38 eV and P3HT with E_g = 1.90 eV[10,18,19,20,21,22]. The chemical structures are shown in Figure 2.2.

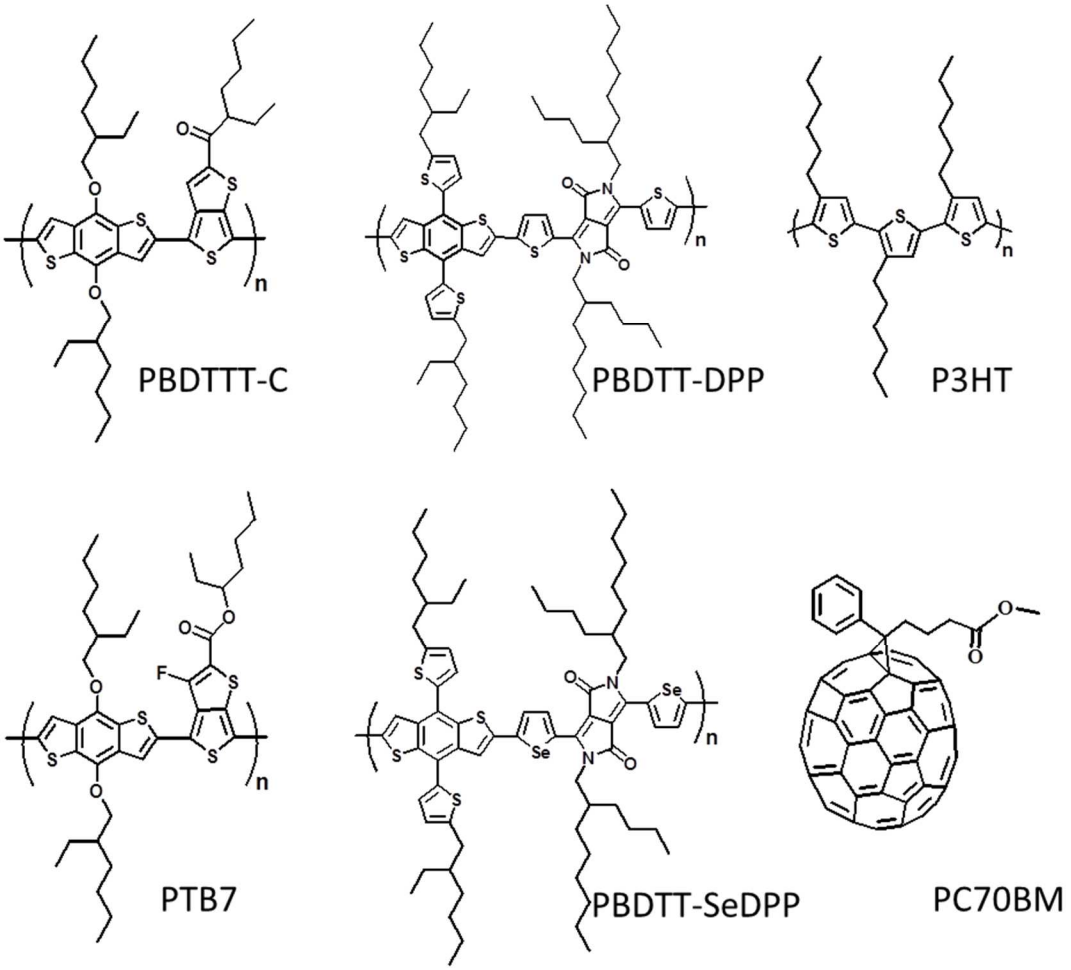

Figure 2-2 Molecular structures of the materials pool in this study

It is well known that different high performance polymers have their own preferred morphologies in the active layer, including molecular orientation with respect to the substrate, crystallinity, domain size and so on. For instance, regio-regular P3HT tends to form edge-on lamellae in P3HT:PCBM films and exhibits much higher crystallinity compared with most other donor polymers, both of which are associated with its high

photovoltaic performance[17,24]. On the other hand, in many of the newer high performance donor polymers such as thienothiophene (TT) and benzo-dithiophene (BDT), BDT and N-alkylthieno[3,4-c]pyrrole-4,6-dione (TPD) based co-polymers[19,25,26,27], the preferred orientation to the substrate is face-on[19,27,28]. This packing orientation is considered to be more advantageous to hole transportation in the vertical diode configuration such as photovoltaic[28,29]. In addition, most of them show significantly more amorphous character in their films than P3HT[28]. We speculate that two blended polymers with compatible physical natures (including molecular orientation, crystallinity and so on) lead to less interference when forming the morphology of the bulk heterojunction active layers. Intuitively, the compatible physical property might strongly relate with the similarity of the chemical structures.

In this work, we focus on identifying key parameter(s) for designing multi-polymer/fullerene derivative blends based on their individual structure-property relationships. The ternary polymer blend/fullerene systems studied here each have both a high band gap polymer and a low band gap polymer in order to cover a boarder section of the solar spectrum. Figure 2.1 and Figure 2.2 show the model materials in this study, all of which have previously been reported as high performance photovoltaic materials featuring different absorption ranges and different molecular stacking preferences. For example, PBDTTT-C and P3HT both have demonstrated high EQE and PCE values, but one prefers edge-on and the other one prefers face-on orientation. These photovoltaic materials have been reported with good device performance, but substantially different processing methods. Choosing a solvent that is compatible with each material represents a particularly difficult challenge. PBDTTT-C and PTB7 generally work best when deposited from

chlorobenzene (CB) with efficiencies of 6.58% and 7.4% respectively, with their performance slightly reduced when processed in dichlorobenzene (DCB)[10,20]. However, polymer PBDTT-DPP and PBDTT-SeDPP are not sufficiently soluble in CB to form uniform films, so they are normally processed from DCB[18,22]. To balance these ideal processing differences and set up an appropriate baseline, all the BHJ devices discussed here are fabricated using DCB as a solvent.

In the material pool shown in Figure 2.1, RR-P3HT has an absorption edge 650nm, and is expected to be spectrally matched to PBDTT-DPP and PBDTT-SeDPP. The devices with blended polymers present a much broader photocurrent response (Figure 2.3), but do not produce an overall enhancement of photocurrent due to significant reductions in EQE.

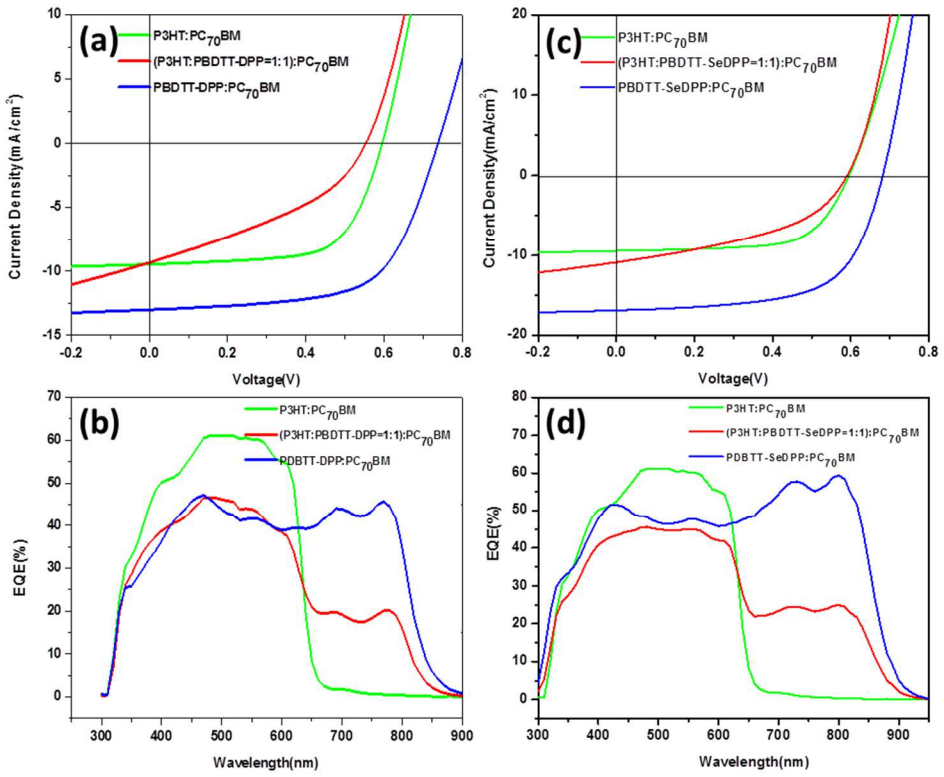

Figure 2-3 J-V and EQE characterization of (P3HT:PBDTT-DPP):PC70BM and (P3HT:PBDTT-SeDPP):PC70BM ternary BHJ solar cell systems. (a) J-V curve of the (P3HT:PBDTT-DPP):PC70BM ternary BHJ solar cell system measured under one sun conditions (100mW/cm2);

(b) EQE measurement of the (P3HT:PBDTT-DPP):PC70BM ternary BHJ solar cell system; (c) J-V curve of the (P3HT:PBDTT-SeDPP):PC70BM ternary BHJ solar cell system measured under one sun conditions (100mW/cm2); (d) EQE measurement of the (P3HT:PBDTT-SeDPP):PC70BM ternary BHJ solar cell system.

Additionally, the fill factor decreased markedly from ~65% to less than 40% in the mixed polymer device. In other word, the addition of absorption doesn't translate into the addition of photovoltaic device performance. These results are not surprising, photovoltaic device employing blended donors have produced even worse performance in many circumstances: result obtained from another low band gap polymers PBDTT-SeDPP, and RR-P3HT ternary BHJ solar cells are also summarized in Figure 2.3 **,** the device performance of these two unsuccessful ternary systems are summarized in Table 2.1.

	Voc (V)	Jsc (mA/cm^2)	FF (%)	PCE(%) Max./Avg.
P3HT:$PC_{70}BM$	0.59	9.5	65.6	3.8/3.8
(P3HT:PBDTT-DPP=1:1):$PC_{70}BM$	0.55	9.4	37.2	1.9/1.8
PBDTT-DPP:$PC_{70}BM$	0.74	13.0	64.2	6.2/6.0
(P3HT:PBDTT-SeDPP=1:1):$PC_{70}BM$	0.59	10.9	42.8	2.8/2.0
PBDTT-SeDPP:$PC_{70}BM$	0.68	16.9	62.9	7.2/7.1

Table 2-1 Device performance of (P3HT:PBDTT-DPP):PC70BM, and (P3HT:PBDTT-SeDPP):PC70BM BHJ ternary solar cell systems.

Our strategy to improve the performance of multiple polymer systems is to optimize the compatibility of the individual donor materials, allowing them to work more like independent cells. The molecular compatibility of two or more polymers can be intuitively expected to correlate with various structural similarities. In the pool of available model

materials, PBDTTT-C, PBDTT-DPP, PTB7, and PBDTT-SeDPP, all have the rigid, planar benzodithiophene (BDT) unit in their backbone. Face-on with respect to the substrate is the preferred orientation for these polymers in deposited active layers.

2.2 Outcomes of device performance

Taking both molecular compatibility and absorption characteristics into consideration, a ternary blending system using PBDTTT-C:PBDTT-DPP as donors was studied. Figure 2.4(a) and Figure 2.4(b) show the device results of the (PBDTTT-C:PBDTT-DPP):$PC_{70}BM$ ternary BHJ solar cells, along with its two binary BHJ solar cells as control devices. Individual PBDTTT-C:$PC_{70}BM$ and PBDTT-DPP:$PC_{70}BM$ solar cells have optimized power conversion efficiency values of 6.4% and 6.2%, respectively. The EQE spectrum of the ternary BHJ device of (PBDTTT-C:PBDTT-DPP=1:1):$PC_{70}BM$ distinctively shows the combined photoresponse of both polymer donors, and as a result the overall photocurrent increases to 15.7mA/cm^2, surpassing each binary reference system. Surprisingly, the ternary BHJ photovoltaic devices still maintain a very high FF of 65%.

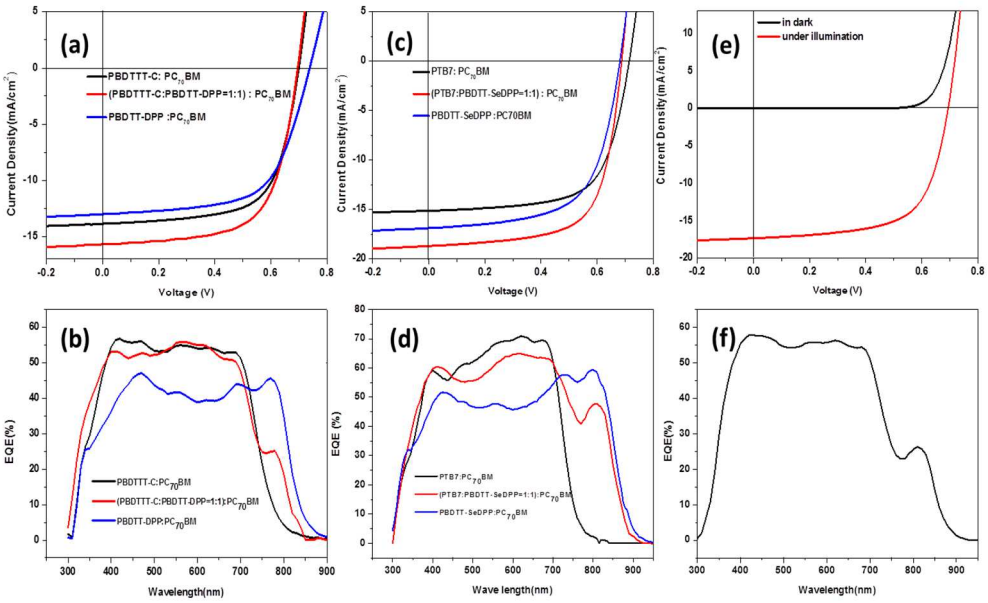

Figure 2-4 J-V and EQE characterization of (PDBTTT-C:PBDTT-DPP):PC70BM and (PTB7:PBDTT-SeDPP):PC70BM ternary BHJ solar cell systems. (a) J-V curve of the (PBDTTT-C:PBDTT-DPP):PC70BM ternary BHJ solar cell system measured under one sun conditions (100mW/cm2); (b) EQE measurement of the (PBDTTT-C:PBDTT-DPP):PC70BM ternary BHJ solar cell system; (c) J-V curve of the (PTB7:PBDTT-SeDPP):PC70BM ternary BHJ solar cell system measured under one sun conditions (100mW/cm2); (d) EQE measurement of the (PTB7:PBDTT-SeDPP):PC70BM ternary BHJ solar cell system; (e) J-V curve of (PBDTTT-C:PBDTT-DPP:PTB7:PBDTT-SeDPP):PC70BM multi-donor BHJ measured under one sun (100mW/cm2) and dark conditions ; (f) EQE measurement of the multi-donor system.

The optimized ternary solar cells outperform the reference binary cells at certain blending ratios (Table 2.2), specifically 3:1 and 1:1 inhere.

	Voc (V)	Jsc (mA/Jsccm^2)	FF (%)	PCE(%) Max./Avg.
PBDTTT-C:$PC_{70}BM$	0.70	14.1	64.0	6.4/6.3
(PBDTTT-C:PBDTT-DPP=3:1):$PC_{70}BM$	0.70	15.7	65.6	7.2/7.2
(PBDTTT-C:PBDTT-DPP=1:1):$PC_{70}BM$	0.70	15.6	64.9	7.1/7.0
(PBDTTT-C:PBDTT-DPP=1:3):$PC_{70}BM$	0.72	13.1	65.0	6.2/6.1
PBDTT-DPP:$PC_{70}BM$	0.74	13.0	64.2	6.2/6.0
PTB7:$PC_{70}BM$	0.72	15.1	66.3	7.2/7.0

(PTB7:PBDTT-SeDPP=3:1):$PC_{70}BM$	0.69	16.2	70.0	7.8/7.7
(PTB7:PBDTT-SeDPP=1:1):$PC_{70}BM$	0.69	18.7	67.4	8.7/8.5
(PTB7:PBDTT-SeDPP=1:3):$PC_{70}BM$	0.69	17.9	62.4	7.7/7.7
PBDTT-SeDPP:$PC_{70}BM$	0.68	16.9	62.9	7.2/7.1
(PBDTTT-C:PBDTT-DPP:PTB7:PBDTT-SeDPP =1:1:1:1):$PC_{70}BM$	0.70	17.3	64.6	7.8/7.6

Table 2-2 Device Performance of the (PDBTTT-C:PBDTT-DPP):$PC_{70}BM$ ternary BHJ solar cellsystem,and device performance of the (PTB7:PBDTT-SeDPP):$PC_{70}BM$ ternary BHJ solar cell system.

Bearing in mind the knowledge obtained from the ternary BHJ photovoltaic systems discussed above, we have further applied this model to a separate ternary blends containing PTB7 and PBDTT-SeDPP. PTB7 has a similar molecular structure and "face-on" molecular orientation to that of PBDTTT-C, and its absorption edge is blue shifted by roughly 10 nm, but the overall photovoltaic performance is better[10,20]. PBDTT-SeDPP is an improved form of PBDTT-DPP, with its absorption edge red shifted by 50 nm to roughly a 900 nm onset[22]. These properties of PTB7 and PBDTT-SeDPP will enable us to observe the effect more clearly (less absorption overlap) and are expected to make them even better ternary blend polymer solar cell system. The ternary (PTB7:PBDTT-SeDPP=1:1):$PC_{70}BM$ device produced an efficiency of 8.7%, which is significantly higher than that of those made from its individual donor materials. For comparison, the PTB7:$PC_{70}BM$ binary BHJ solar cell produced 7.2% efficiency, and the PBDTT-SeDPP:$PC_{70}BM$ binary BHJ solar cell achieved 7.2% as well(both binary cell used DCB as solvent), which gave the blended donor devices a 21% relative enhancement in PCE with respect to the binary cell(see Figure 2.4 (c) and Figure 2.4 (d)). The ternary BHJ photovoltaic outperformed each binary BHJ

photovoltaic at three different polymer blending ratios – 25%, 50% and 75% PBDTT-SeDPP (Table 2.2). The D/A ratio in all of the devices was 1:2. It worth mentioning that the ternary BHJ photovoltaic device can be expected to further improve by optimizing the D/A ratio and by changing the solvent or using a co-solvent system, since the optimized solvents for PTB7 and PBDTT-SeDPP are different as mentioned in the previous section. Since both the PBDTTT-C:PBDTT-DPP and PTB7:PBDTT-SeDPP systems appear to provide good structural compatibility and device performance, if the scenario is correct, it should enable an efficient BHJ polymer solar cell with any two blended polymers. Indeed, preliminary results show that PBDTTT-C:PBDTT-SeDPP and PBT7:PBDTT-DPP ternary BHJ solar cells deliver reasonably good device performance as well. (Figure 2.5, Figure 2.6).

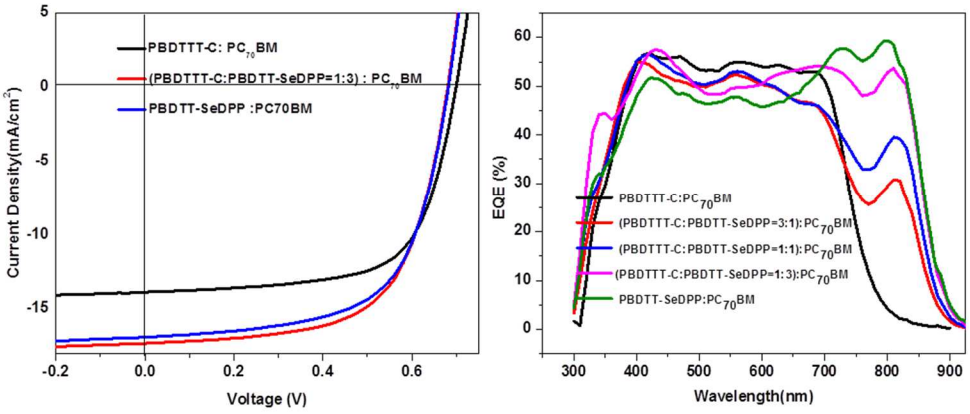

Figure 2-5 J-V and EQE characterization of (PBDTTT-C:PBDTT-SeDPP):$PC_{70}BM$ and (PBDTTT-C:PBDTT-SeDPP):$PC_{70}BM$ ternary BHJ solar cell systems. (a) J-V curve of the (PBDTTT-C:PBDTT-SeDPP):$PC_{70}BM$ ternary BHJ solar cell system measured under one sun conditions (100mW/cm^2); (b) EQE measurement of the (PBDTTT-C:PBDTT-SeDPP):$PC_{70}BM$ ternary BHJ solar cell system;

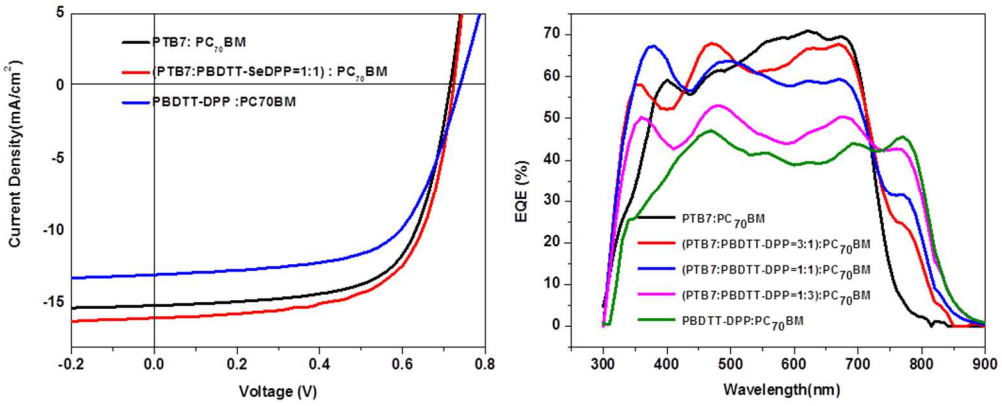

Figure 2-6 J-V and EQE characterization of (PTB7:PBDTT-DPP):$PC_{70}BM$ and (PTB7:PBDTT-DPP):$PC_{70}BM$ ternary BHJ solar cell systems. (a) J-V curve of the (PTB7:PBDTT-DPP):$PC_{70}BM$ ternary BHJ solar cell system measured under one sun conditions (100mW/cm^2); (b) EQE measurement of the (PTB7:PBDTT-DPP):$PC_{70}BM$ ternary BHJ solar cell system;

Furthermore, A four-donor BHJ solar cell presented the very reasonable performance of 7.8% efficiency, with EQE values close to those of the constituent polymers (Figure 2.4(e)&(f)). The results conceptually indicate that mixing two or even more donor materials into one BHJ is possible as long as they exhibit sufficient structural compatibility.

2.3 Electrical characterization

Clearly, the dramatically different results of different dual polymer BHJ systems infer that structurally compatible polymers can efficiently coexist, while using structurally incompatible polymers, such as P3HT and PBDTT-DPP or PBDTT-SeDPP, appears to have the opposite effect, ultimately causing severe reductions in device performance. To better understand the working mechanism as well as the differing photovoltaic device performance in different ternary BHJ systems. We further applied transient techniques to characterize the charge transport property and the recombination dynamics.

Charge transport is critical to organic photovoltaic device performance, especially in polymer solar cells with multiple donors. Unfavorable interactions between different polymers within the active layer can easily inhibit charge transport capabilities and hence limit device efficiency. Figure 2.7 shows the electrical-field dependent CELIV photocurrent transient characteristics of the binary and its corresponding ternary systems.

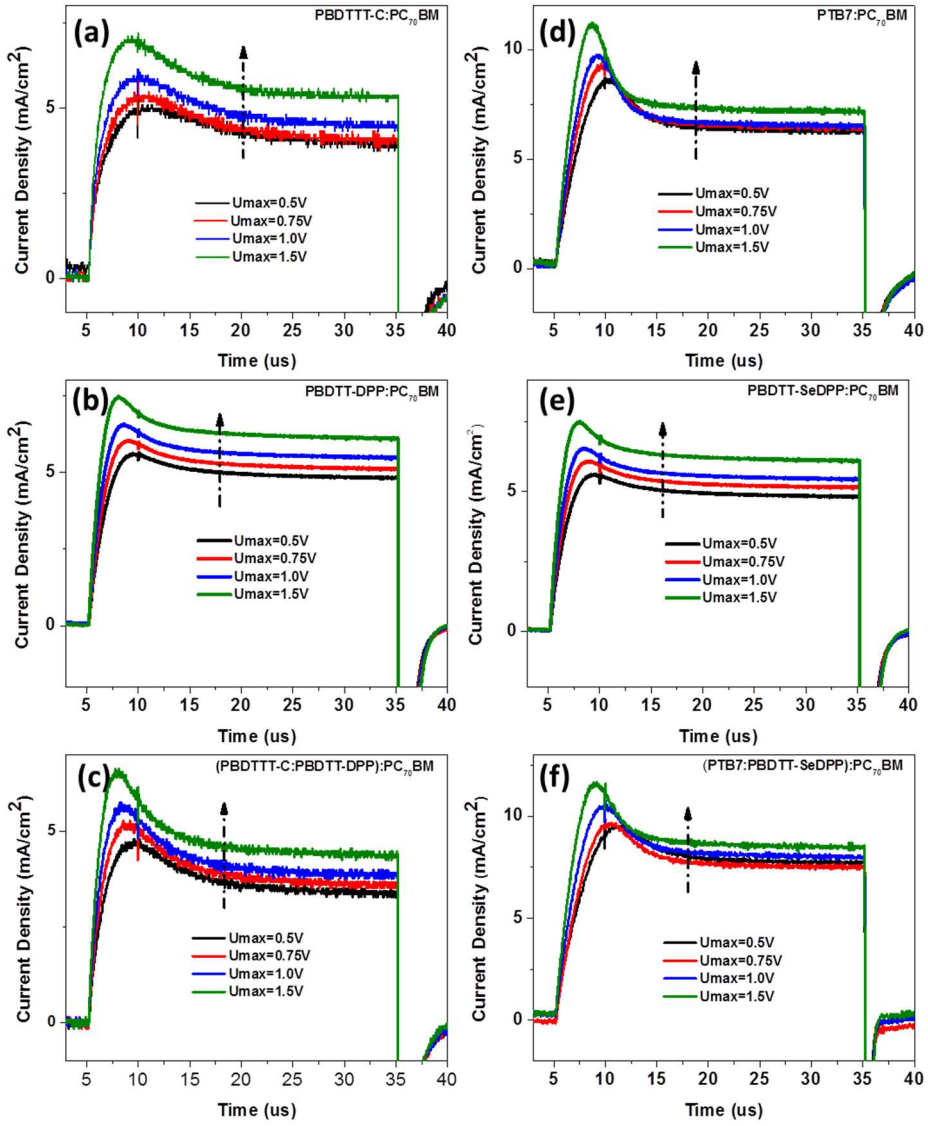

Figure 2-7 Photo-CELIV (Charge Extraction by Linearly Increasing Voltage) measurements of (PDBTTT-C:PBDTT-DPP):$PC_{70}BM$ and (PTB7:PBDTT-SeDPP):$PC_{70}BM$ ternary BHJ solar cell systems. Photo-CELIV transient of (a) PBDTTT-C:$PC_{70}BM$; (b) PBDTT-DPP:$PC_{70}BM$; (c)

(PBDTTT-C:PBDTT-DPP):$PC_{70}BM$; (d) PTB7:$PC_{70}BM$; (e) PBDTT-SeDPP:$PC_{70}BM$; (f) (PTB7:PBDTT-SeDPP):$PC_{70}BM$ with different applied electrical field. All the tannery BHJ devices have the same blending ratio of 1:1.

The effective charge carrier mobility of the organic film with moderate conductivity can be estimated based on the following equation (1).[30, 31]

$$\mu = \frac{2d^2}{3At_{max}^2\left[1 + 0.36\frac{\Delta j}{j(0)}\right]} \quad \text{if } \Delta j \leq j(0) \tag{1}$$

Where μ is the mobility, d is the thickness of the BHJ active layer, t_{max} is the time when the extracted current reaches its maximum value, A is the slope of the extraction voltage ramp, j_0 is the dark capacitive current, and Δj is the transient current peak height, as shown in Figure 2.8.

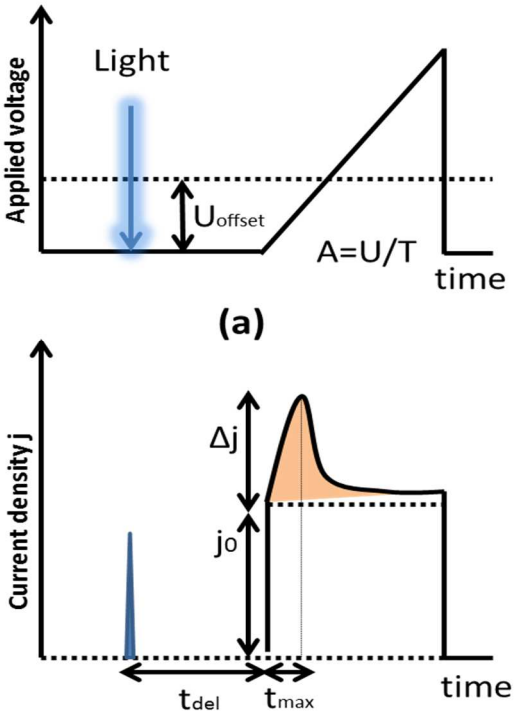

Figure 2-8 Schematic illustration and experimental setup of Photo-CELIV (Charge Extraction by Linearly Increasing Voltage) measurement.

The mobility values of the effective charge carriers in the (PBDTTT-C:PBDTT-DPP=1:1):$PC_{70}BM$ ternary system was 9.6 x 10^{-5} cm^2/Vsec, which was comparable to PBDTT-DPP:$PC_{70}BM$ device's mobility (9.7 x 10^{-5} cm^2/Vsec), and even slightly higher than the other binary reference PBDTTT-C:$PC_{70}BM$ device (4.0 x 10^{-5} cm^2/Vsec). In the other compatible ternary BHJ solar cell system, the (PTB7:PBDTT-SeDPP=1:1):$PC_{70}BM$ ternary system has an effective carrier mobility of 6.5 x 10^{-5} cm^2/Vsec, comparable to its corresponding binary systems with PTB7:$PC_{70}BM$ device (5.4 x 10^{-5} cm^2/Vsec) and PBDTT-SeDPP:$PC_{70}BM$ device (9.2 x 10^{-5} cm^2/Vsec). It indicates that the transport property within the structurally compatible ternary BHJ solar cell is not interrupted if not enhanced.

On the other hand, in devices made from the incompatible ternary BHJ system containing P3HT and PBDTT-DPP or PBDTT-SeDPP, a very different CELIV pattern was observed as shown in Figure 2.9. Both (P3HT:PBDTT-DPP):$PC_{70}BM$ and (P3HT:PBDTT-SeDPP):$PC_{70}BM$ ternary systems showed a much broader current transient peak, which implied the charge transport inside those BHJs was much more dispersive. The t_{max} of these unfavorable ternary BHJ solar cells were larger, accordingly, the effective carrier mobility was at least one order lower than their corresponding binary references. The electrical field dependent carrier mobility was also studied by varying the highest extraction voltage. As seen in Figure 2.9 (f), the carrier mobility of the incompatible ternary BHJ device incorporated with P3HT and low band gap polymers is one order lower than the compatible ternary BHJ devices. Besides, they exhibit stronger positive field dependence, which usually indicates an electronic disordering character. The dramatically different charge transport property within different ternary BHJ solar cell systems explains

the different fill factors observed from these devices.

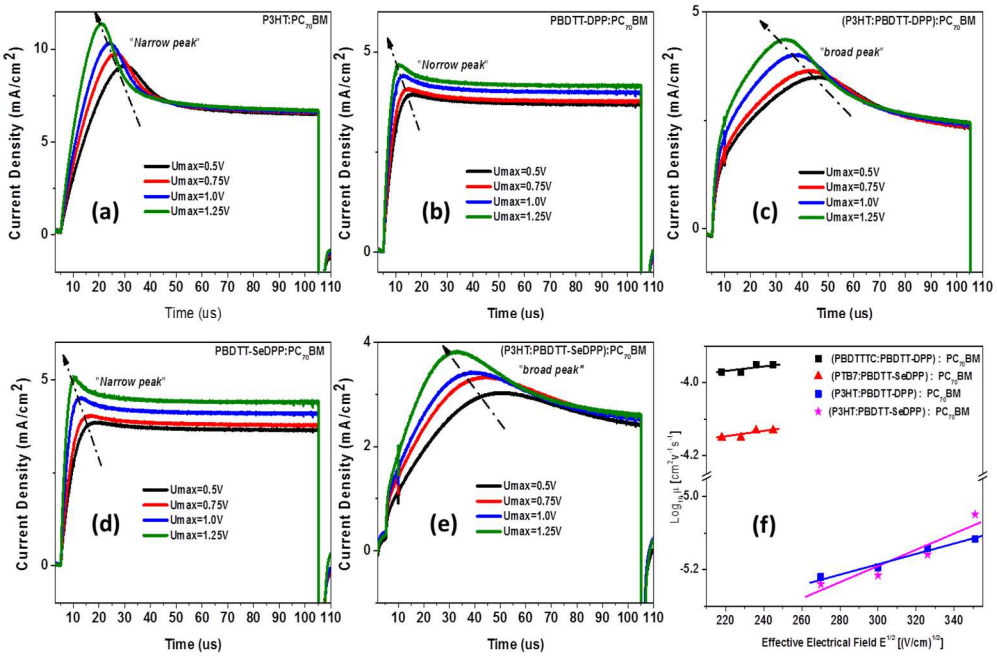

Figure 2-9 Photo-CELIV (Charge Extraction by Linearly Increasing Voltage) measurements of the (P3HT:PBDTT-DPP):$PC_{70}BM$ and (P3HT:PBDTT-SeDPP):$PC_{70}BM$ ternary BHJ solar cell systems. Photo-CELIV transient of (a) P3HT:$PC_{70}BM$; (b) PBDTT-DPP:$PC_{70}BM$; (c) (P3HT:PBDTT-DPP):$PC_{70}BM$; (d) PBDTT-SeDPP:$PC_{70}BM$; (e) (P3HT:PBDTT-SeDPP):$PC_{70}BM$ with different applied electrical field. All the tannery BHJ devices have the same blending ratio of 1:1;(f) Electrical field dependent charge carrier mobility of the compatible and incompatible ternary BHJ solar cell systems.

The charge transport study implies that more electronic traps arise if incompatible polymers are blended, and generally those uncomplimentary traps might provide as recombination centers as well, and the open circuit voltage will be limited if the recombination loss is severe enough. The open circuit voltage describes the energetic transfer process from exciton generation to free carrier collection, and it is of particular interest for the ternary BHJ solar cells.[32,33] It is known that the V_{OC} is determined by the effective band gap of the donor/acceptor blends subtracted by recombination loss.[34,35] For the conventional binary BHJ, the effective band gap might be simply defined as the

difference between highest occupied molecular orbital (HOMO) of the donor and lowest unoccupied molecular orbital (LUMO) of the acceptor,[34] however that is no longer practical for the ternary or multiple compounds systems. A better way to define it is through its equivalent charge transfer state, which sets the upper limit of the Voc. The tunable charge transfer state is observed in some of the ternary BHJ solar cell systems.[36] In our case, we also find the charge transfer state of the (PBTDDD-C:PBDTT-DPP):$PC_{70}BM$ and (PTB7:PBDTT-SeDPP):$PC_{70}BM$ ternary systems is roughly in between of the relative binary systems, but is slightly closer to the one with lower charge transfer state, measured by the highly sensitive photo spectral response (PSR) (Figure 2.10) The Voc difference correlates well with the measured charge transfer state, which is a hint that the recombination loss within such systems are around the same level.

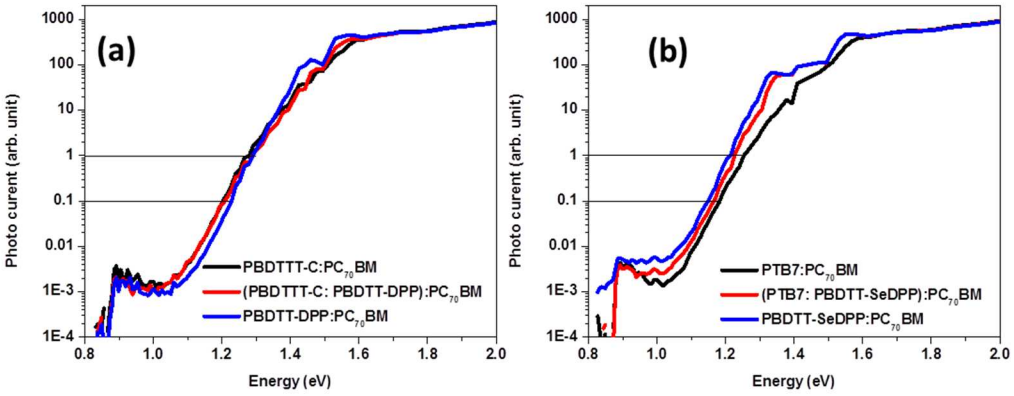

Figure 2-10 Photo spectral response (PSR) of the ternary BHJ solar cell systems of (a) (PDBTTT-C:PBDTT-DPP):$PC_{70}BM$ system; (b) (PTB7:PBDTT-SeDPP):$PC_{70}BM$ system.

The recombination dynamics were directly investigated by the transient photo-voltage (TPV) technique as shown in Figure 2.11, the measurement was conducted under one-sun light bias. The solar cell is considered as working on the open circuit condition, (connected with 1M Ω resistor) so the transient photo-voltage decay describes the recombination of

the photo-induced carriers.[37] Figure 2.11 (a),(b) indicate that the carrier lifetime of the compatible ternary BHJ solar cells is not reduced compared with their corresponding binary systems, if not increased. On the other hand, the carrier lifetime of poorly-performed ternary systems containing P3HT and PBDTT-DPP or PBDTT-SeDPP, is much lower than that in the P3HT:$PC_{70}BM$ device, and close to or lower than the low band gap polymer:$PC_{70}BM$ devices. It is worth mentioning that only the carrier lifetime value itself doesn't necessarily predicate the recombination rate, the open circuit charge carrier density also matters, which can be determined by charge extraction experiments.[38] To summarize, the Voc can be well maintained if compatible polymers are mixed, since negligible additional recombination is introduced.

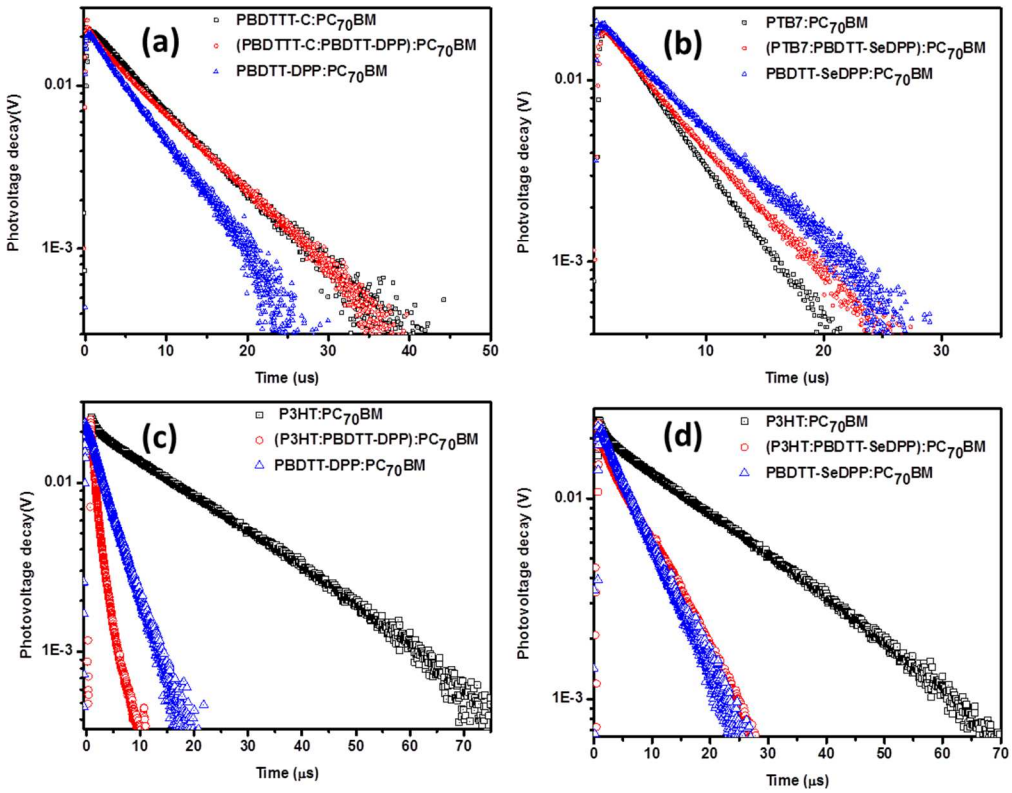

Figure 2-11 Transient photo-voltage (TPV) decay of the ternary BHJ solar cell systems of (a) (PDBTTT-C:PBDTT-DPP):$PC_{70}BM$; (b) (PTB7:PBDTT-SeDPP):$PC_{70}BM$; (c)

(P3HT:PBDTT-DPP):PC70BM; (d) (P3HT:PBDTT-SeDPP):$PC_{70}BM$. The measurment is under one-sun light bias.

2.4 Morphology characterization

To correlate the electronic properties of the ternary blending and photovoltaic device performance with the structural information, and understand the physical origin on the molecular level, Grazing Incidence Wide Angle X-ray Scattering (GIWAXS) was performed. The 2D GIWAXS patterns for each individual polymer and their blends are shown in Figure. 2.12. All thin film samples were measured on an Si substrate (with naturally formed SiO_2 surface) pre-coated with 30 nanometers of PEDOT:PSS. Distinct out-of-plane peaks appear in the PBDTTT-C, PBDTT-DPP, PTB7, and PBDTT-SeDPP films, with q_z = 1.57 ± 0.06 Å, 1.60 ± 0.06 $Å^{-1}$, 1.61 ± 0.06 $Å^{-1}$ and 1.60 ± 0.06 $Å^{-1}$ respectively, which are associated with the π-π stacking distance of 4.0 ± 0.2 Å. This indicates that the π-π stacking direction is perpendicular to the substrate in such films, and thus they prefer a "face-on" orientation. After PBDTTT-C and PBDTT-DPP were blended together, this π-π stacking peak still appears in the 2D GIWAXS pattern with qz = 1.58 ± 0.06 Å, which suggests that the preferred molecular orientation with the substrate remains unchanged in the blended film.

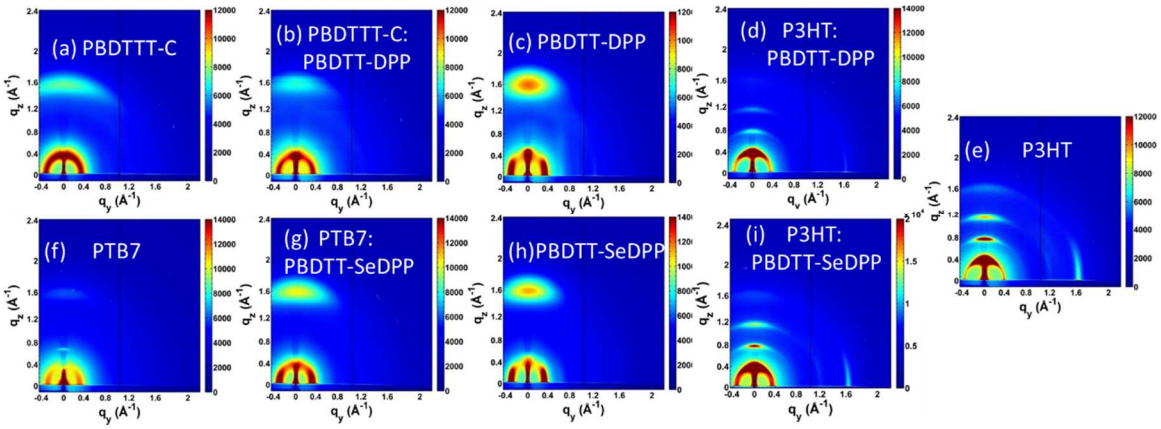

Figure 2-12 GIWAXS (Grazing Incidence Wide Angle X-ray Scattering) patterns of (a) PBDTTT-C; (b) PBDTTT-C:PBDTT-DPP blending; (c) PBDTT-DPP; (d) P3HT:PBDTT-DPP blending; (e) P3HT; (f) PTB7; (g) PTB7:PBDTT-SeDPP blending; (h) PBDTT-SeDPP; (i) P3HT:PBDTT-SeDPP blending;

The π-π stacking coherence length can also be estimated through using the full width at half-maximum (fwhm) of the scattering peaks based on the Scherrer equation.[40,41] We found that the coherence length along the π-π stacking direction for PBDTTT-C, PBDTTT-C:PBDTT-DPP blend, and PBDTT-DPP are 15 Å, 19 Å, and 15 Å, respectively, which corresponds to roughly 3~4 stacked molecules in the pristine polymer films, and slightly increases to 4~5 stacked molecules in the blending film. These results indicate a general retention of π-π coherence length ($L_{\pi-\pi}$) are retained after the two "face-on" polymers are mixed, which is a promising sign of their ability to form compact films without disrupting the morphology and stacking structure of the other polymer. Similarly, the distinctive π-π stacking peak is also retained in the PBT7:PBDTT-SeDPP blending film, and the π-π coherence length ($L_{\pi-\pi}$) is 17 Å, comparable to pristine PTB7 (18 Å) and pristine PBDTT-SeDPP (17 Å).

While in the P3HT case, the π-π stacking peak in pure P3HT films are shown up both in plane and out of plane, but more manifestly in the in-plane axis, with $q_y = 1.61 \pm 0.01$ Å-1 indicating a stronger preference for the "edge-on" orientation. Three distinct peaks arising from the (100), (200), and (300) Bragg diffraction peaks corresponding to periodic P3HT lamellae in the out-of-plane direction were also observed, which have been reported in previous structural studies of P3HT films[17]. Unfortunately by blending the PBDTT-DPP with the P3HT, no scattering peaks corresponding to π-π stacking of both polymers (particularly PBDTT-DPP) could be observed in the out-of-plane direction, suggesting that

the ordered molecular packing along the vertical direction was significantly suppressed in the mixtures of P3HT and PBDTT-DPP. It is generally believed face-on orientation is more favorable for photovoltaic device due to its vertical charge transportation channel. The undermined molecular ordering along vertical direction inevitably impedes the charge transportation property of the photovoltaic device. Due to the strong crystallinity of P3HT, the in-plane π-π stacking peak is still present in the blending film, however, the π – π stacking coherence length (Lπ–π) reduced from 61 Å to 50 Å, corresponding to a reduced number of π-π stacked molecules from ~15 to ~12, which implies that the molecular ordering in the in-plane direction is interrupted as well. The GIWAXS pattern of the P3HT and PBDTT-SeDPP demonstrates the similar trend. The GIWAXS scanning curves along each direction are provided in Figure 2.13 and Figure 2.14.

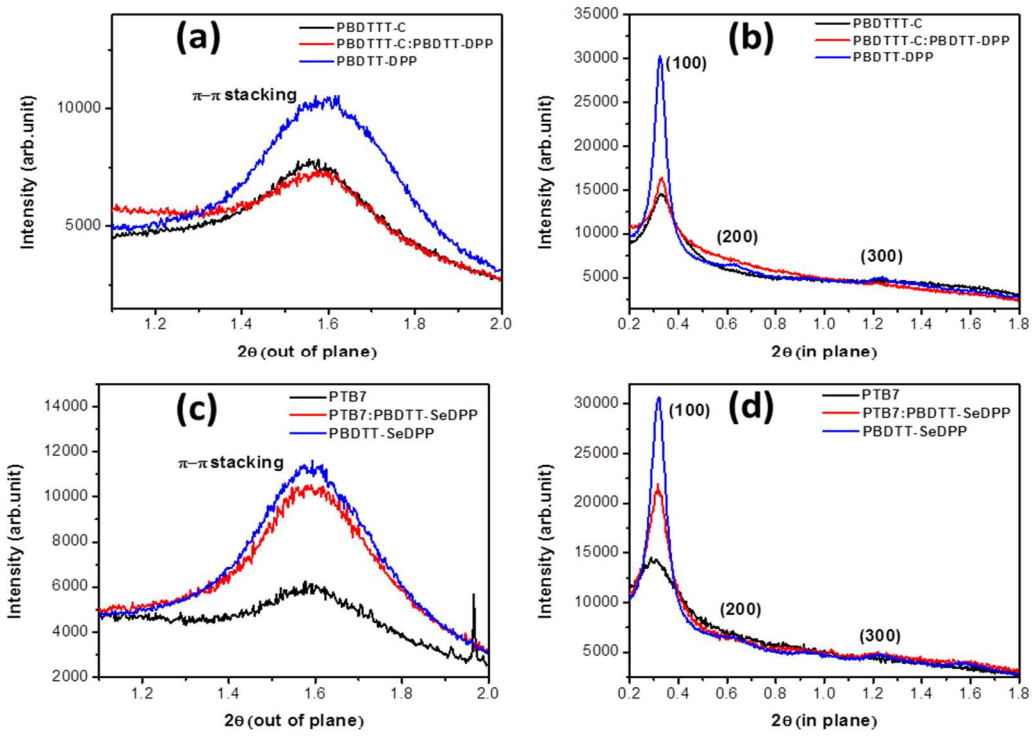

Figure 2-13 GIWAXS (Grazing Incidence Wide Angle X-ray Scattering) scanning curve of (a) PBDTTT-C:PBDTT-DPP blending system (out of plane); (b) PBDTTT-C:PBDTT-DPP blending

system (in plane); (c) PTB7:PBDTT-SeDPP blending system (out of plane); (d) PTB7:PBDTT-SeDPP blending system (in plane).

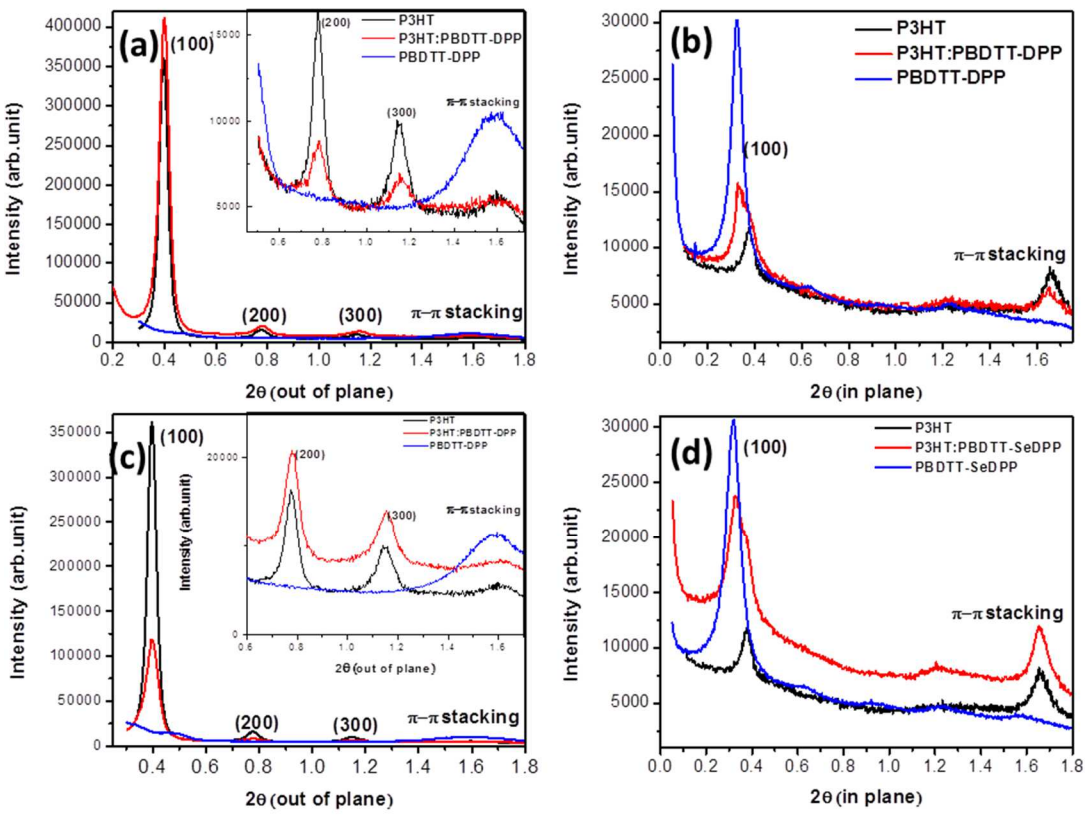

Figure 2-14 GIWAXS (Grazing Incidence Wide Angle X-ray Scattering) scanning curve of (a) P3HT:PBDTT-DPP blending system (out of plane); (b) P3HT:PBDTT-DPP blending system (in plane); (c) P3HT:PBDTT-SeDPP blending system (out of plane); (d) P3HT:PBDTT-SeDPP blending system (in plane).

This measurement evidently tells that the molecular ordering is well maintained in the compatible polymer mixture, but is greatly disturbed in the incompatible polymer blending. The molecular disorder arisen from the mixing of incompatible polymers is very likely one of the key physical origins of the electronic traps and recombination sites, and hence limits the photovoltaic performance of the multiple donor solar cells. The non-conjugated polymer side chain is largely insulating, while the conjugated backbone is conductive. When two polymers with different molecular orientation are mixed, as in the

P3HT:PBDTT-DPP blended system, we propose that the non-conductive side chain of one polymer is likely to be close to the conductive conjugated backbone of the other polymer. This type of unfavorable molecular pattern becomes “morphological traps”, reduces the crystalline length, disrupts long range charge transport and lowers the charge carrier mobility of the blended film. The proposed scenario of the local molecular disordering is illustrated in Figure 2.15.

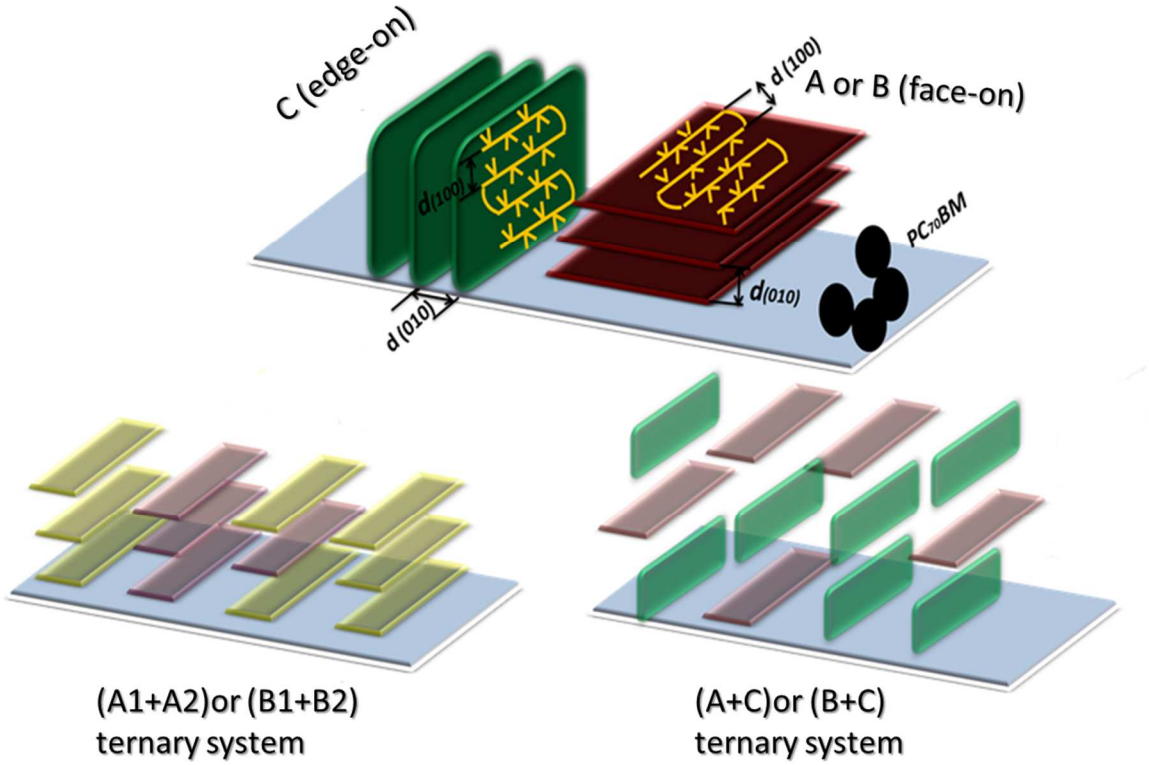

Figure 2-15 Schematic of lacal morphological trap in the incompatible polymer blendings

Besides the molecular crystallinity, another important morphological factor that will determine the photovoltaic performance is how these localized molecular crystals and aggregates form phase-separated domains in the BHJ. Figure 2.16 show the resonant soft X-ray scattering (RSoXS) profiles (open symbols), the calculated scattering intensities, I(q),

(solid lines), and their corresponding pair distance distribution functions (PDDFs), P(r), of the compatible and incompatible ternary BHJ films.

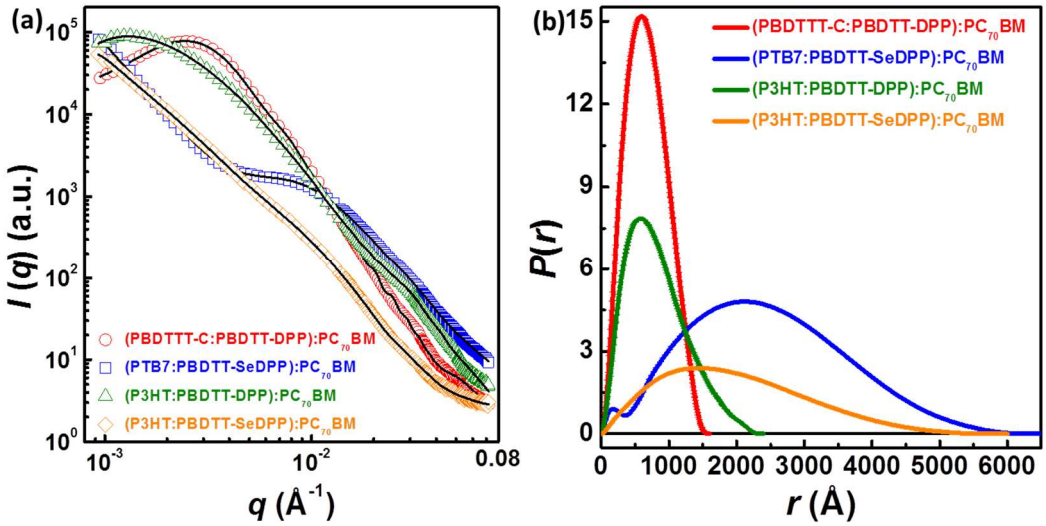

Figure 2-16 RSoXS profiles (open symbols), calculated $I(q)$ (solid lines); (k) corresponding $P(r)$ of (PBDTTT-C:PBDTT-DPP):$PC_{70}BM$ (red), (PTB7:PBDTT-SeDPP):$PC_{70}BM$ (blue), (P3HT:PBDTT-DPP):$PC_{70}BM$ (green) and (P3HT:PBDTT-SeDPP):$PC_{70}BM$ (orange).

(PBDTTT-C:PBDTT-DPP):$PC_{70}BM$, (P3HT:PBDTT-DPP):$PC_{70}BM$ and (P3HT:PBDTT-SeDPP):$PC_{70}BM$ form similar domain structures at the length scales of hundreds of nanometers. As indicated by the zero crossing of P(r), (P3HT:PBDTT-DPP):$PC_{70}BM$ and (P3HT:PBDTT-SeDPP):$PC_{70}BM$ exhibit much larger domain size than the (PBDTTT-C:PBDTT-DPP):$PC_{70}BM$, which correlates with their unsatisfied device performance, especially the low Jsc. Interestingly, the best performed (PTB7:PBDTT-SeDPP):$PC_{70}BM$ ternary BHJ device shows hierarchical nanomorphologies at multiple length scales, in consistence with the previous observations in PTB7:$PC_{70}BM$.[40,42] A kink of P(r) at the length scales of tens of nanometers indicates that the fine domains are even smaller than the that of the other three blended systems. These compositionally heterogeneous small domain regions exist inside phase-separated domains with hundreds

of nanometers scale. It has been proposed that these hierarchical nanomorphologies are related to significantly enhanced exciton dissociation, which consequently contributes to the photocurrent.[40] The retain of such nanostructural characteristics at multiple length scales not only explains the high efficiency of (PTB7:PBDTT-SeDPP):$PC_{70}BM$ device but also demonstrates that the sophisticated nanomorphology determining the superior device performance can be well maintained in compatible ternary BHJ systems.

2.5 Discussions on working mechanism

The underlying working mechanism of the ternary BHJ solar cell is complicated, and it varies by the particular blending system. There are several possibilities of how the blending donor materials interact with each other: I. the low band gap donor could be IR-sensitizer (back hole transfer from low band gap sensitizer); II. Exciton energy transfers from wide band gap donor to the low band gap donor; III. Different donors work separately.[23] Those possible working principle could dominate or coexist in one specific ternary system.

In the successful ternary systems studied here, the HOMO of the blending materials is close to each other, hence mechanism I is not likely dominating. Given the fact that the photoluminescence (PL) spectra is approximately the averaging of the two materials (Figure 2.17), the possibility of the exciton energy transfer process is excluded.

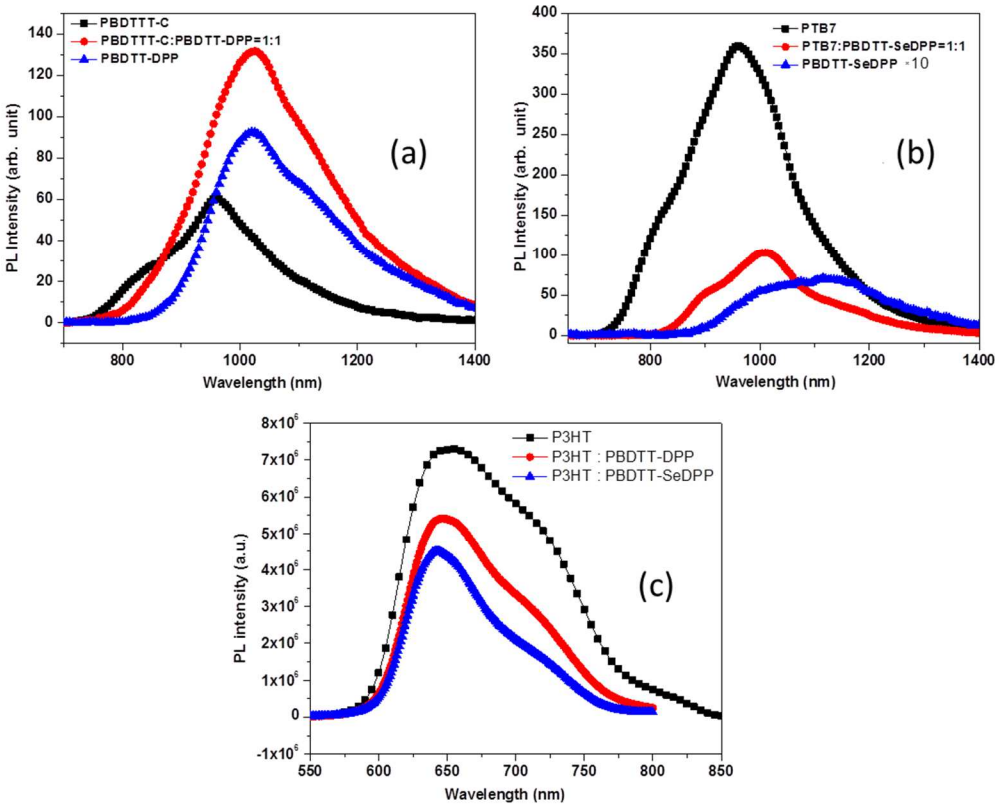

Figure 2-17 Photoluminenscence spectra of (a) PBDTTT-C:PBDTT-DPP blending system; (b) PTB7:PBDTT-SeDPP blending system; (c) P3HT:PBDTT-DPP and P3HT:PBDTT-SeDPP blending systems.

It is believed to work like paralleled devices. In such scenario the Nano morphology of each polymer matters since they both contribute to the hole transportation pathway. While in the incompatible polymer blending, the exciton energy transfer from P3HT to the low band gap polymer is believed not dominating evidenced by the fact the PL of P3HT is not effectively quenched by adding low band gap donors. (Figure 2.17) Due to relatively bigger HOMO level difference in such system, it is possible that the low band gap polymer works as IR-sensitizer and transfers the hole to the P3HT just as the working mechanism in P3HT and Si-PCPDTBT ternary system[43]. In such case, the hole transportation is mainly determined by the P3HT morphology, which is interrupted by

blending with the incompatible low band gap polymers. It is also likely that mechanism I and III coexist, so both P3HT and the low band gap polymers contribute to hole conduction. The nano morphology of both P3HT and the low band gap polymer are disrupted in the blending system, and it provides an explanation for the hindered charge transportation and lowered device efficiency.

However, an alternative explanation might be that the relatively bigger HOMO level difference of P3HT and the low band gap polymers induces energetic disorder which impedes the charge transportation. Although it is not confirmed whether similar HOMO is a presupposition for the successful ternary BHJ solar cell, only ensuring small HOMO offset is not necessarily leading to a success. The preliminary result shows that the ternary BHJ consisting of PBDTTT-C (HOMO: 5.08eV) and Si-PCPDTBT (5.16eV), which has similar HOMO offset as the successful ternary BHJ in our study, doesn't deliver a promising device performance. The effect of HOMO level offset in ternary or multi-donor BHJ device is definitely worth further investigation, since it plays a significant role in determining the Voc by modulating the charge transfer state and energetic disorder that affects the hole transportation.

2.6 Summary

Taken together, the GIWAXS and RSoXS results explain on a molecular and domain scale the dramatically different electronic and photovoltaic device performance of the two ternary BHJ systems. The blending of structurally compatible polymers with the identical BDT unit doesn't introduce significant interference to their molecular stacking preferences, and even crystallite size and domain structure is also retained. Therefore, the electronic

properties are preserved in the ternary blends; two different molecules can coexist in harmony, and contribute to the improved photovoltaic performance by broadening the absorption range. With this in mind, we can infer that molecules with complementary absorption ranges and good structural compatibility, such as similar crystallinity and molecular orientation, are potential candidates to achieve high performance ternary BHJ solar cells. Structural compatibility may also be linked to polymers with similar molecular groups, such as the shared BDT unit in the backbones of PBDTTT-C and PBDTT-DPP.

In summary, we report the structural, electronic, and photovoltaic characteristics of several ternary BHJ solar cell systems. Two successful ternary BHJ solar cells have been demonstrated, and the best devices achieved 8.7% PCE. By comparing the successful and unsuccessful multiple donor systems, a relationship between device performance and the molecular structure of the donor materials has been established. We conclude that structural compatibility is the key factor for achieving high performance in multiple donor BHJ polymer solar cells. Indications of compatibility between polymers include preferred molecular orientation, crystallite size, domain structure and so on. This work not only proves the feasibility of producing highly efficiency BHJ polymer solar cells that incorporate more than one donor material, but also provides guidelines for matching existing materials and designing new ones explicitly for achieving high performance OPVs.

2.7 Experimental details

Materials: P3HT was purchased from Rieke Metals. $PC_{70}BM$ were purchased from Nano-C. PTB7 and PBDTTT-C was purchased from 1-Material Inc and Solarmer Materials Inc., respectively. These materials were used as received without further purification. PBDTT-

DPP and PBDTT-SeDPP were synthesized in-house, according to recipes reported in previous papers[18,22]. The polymers used in this project were all from the same batch in order to ensure a fair comparison between experimental and control devices.

Device fabrication and measurement: Photovoltaic devices were fabricated on indium tin oxide (ITO) coated glass substrates that served as the anode. The ITO substrates were ultrasonically cleaned in detergent, deionized water, acetone, and isopropanol. A layer of 30 nm PEDOT:PSS (poly(3,4-ethylenedioxythiophene): poly(styrene sulfonate)) (Baytron P VPAI 4083, Germany) was spin-coated onto the ITO substrate and was dried in air at 120 ℃ for 10 minutes. Polymer/$PC_{70}BM$ or Polymer blend/$PC_{70}BM$ were dissolved in 1,2-dichlorobenzene (O-DCB) and were spin-coated on top of the PEDOT layer. Finally, the Ca/Al cathode (100 nm) was vacuum evaporated onto the annealed photoactive layer. The reference P3HT:PC70BM solar cells were spin coated at 800 rpm with a 1:1 D/A ratio followed by a "slow growth" method, as reported in the literature[9], the thickness was around 210nm. For both the (PBDTTT-C:PBDTT-DPP):$PC_{70}BM$ and (PTB7:PBDTT-SeDPP):$PC_{70}BM$ ternary BHJ solar cell systems, the D/A ratio was kept at 1:2, and each was spinning casted from (DCB + 3% DIO) solutions. The optimized thicknesses for PBDTTT-C:$PC_{70}BM$, (PBDTTT-C:PBDTT-DPP=1:1):$PC_{70}BM$ and PBDTT-DPP:$PC_{70}BM$ solar cells were 100nm, 120 nm, and 105 nm, respectively. In the (PTB7:PBDTT-SeDPP):$PC_{70}BM$ ternary BHJ solar cell system, the optimized thickness for PTB7:$PC_{70}BM$, (PTB7:PBDTT-SeDPP=1:1):$PC_{70}BM$ and PBDTT-DPP:$PC_{70}BM$ solar cells were 95nm, 115 nm, and 100 nm, respectively. For the four-donor BHJ solar cell, the active layer was spin-cast from the combined solution of (PBDTTT-C:PBDTT-DPP=1:1):$PC_{70}BM$ and (PTB7:PBDTT-SeDPP=1:1):$PC_{70}BM$ with a 1:1 vol. ratio, so that

the D/A ratio is 1:2, and the device thickness is roughly 120nm. The effective area of the devices was 0.1 cm^2. The current-voltage (J-V) measurements of the photovoltaic devices were conducted using a Keithley 236 Source-Measure unit. A xenon lamp with an AM1.5G filter (NEWPORT) simulated 1 sun conditions, and the light intensity at the sample was 100 mW/cm2 , calibrated with a Mono-Si photodiode with KG-5 color filter. The reference diode is traceable to NREL certification. EQE measurements were conducted with an integrated system (system name) from EnliTech, Taiwan.

Photo-CELIV measurements: Photo-CELIV measurements were used to study the charge transportation property in the single and multiple donor BHJ solar cells. A 590 nm dye (Rhodamine Chloride 590) laser pumped by a nitrogen laser (LSI VSL-337ND-S) was used as the excitation source, with pulse energy and pulse width values of 0.03μJ/cm^2 and 4 ns, respectively. The triangle voltage pulse was applied by the function generator (Tektronix AFG 3532). The current transient was recorded by a digital oscilloscope (Tektronix DPO 4104). The offset voltage was applied to all the measurement to compensate the internal electrical filed. The field dependent mobility is measured by modulating the highest extraction voltage. The effective electrical field is determined by E=At/d, where t is the time when current transient approaches displacement current j_0, it means the charge extraction is completed. CELIV is not the best method to give accurate field dependent mobility since the electrical field is varied during measurement. Here, we only focused on the relative comparison of the field dependence.

Transient photovoltage (TPV) measurement: The device structure was ITO/PEDOT:PSS/Polymer or Polymer Blend:$PC_{71}BM$/Ca/Al. A 590 nm dye (Rhodamine Chloride 590) laser pumped by a nitrogen laser (LSI VSL-337ND-S) was used as the

excitation source, with pulse energy and pulse width values of 0.03μJ/cm^2 and 4 ns, respectively. The measurement was conducted under one sun condition by illuminating the device with a while light LED. The input impedance of the oscilloscope (Tektronix DPO 4104) is 1 MΩ, and the solar cell device is considered as working at the open circuit condition. The charge carrier can't be extracted but recombined. Therefore, the transient decay can represent the charge carrier lifetime.

High-Sensitivity Photo spectral response (PSR) measurement: The experimental set up is basically similar as the EQE measurement, but with much higher sensitivity. The incident light is modulated with optical chopper with 171 HZ, and the photocurrent is firstly amplified by using a 100K resistor and captured by the lock-in amplifier (Stanford Research SR830). The photocurrent can drop ~6 orders before reaching the noise level.

Grazing Incidence Wide Angle X-ray Scattering (GIWAXS): GIWAXS was performed at the 8ID-E beamline at the Advanced Photon Source (APS), Argonne National Laboratory using x-rays with a wavelength of λ = 1.6868 Å and a beam size of ~200 μm (h) × 20 μm (v). A 2-D PILATUS 1M-F detector was used to capture the scattering patterns and was situated at 208.7 mm from samples. All the samples were prepared on PEDOT:PSS modified Si substrates to emulate the fabrication condition of OPV devices. Typical GISAXS patterns were taken at an incidence angle of 0.20°, above the critical angles of polymers:$PC_{70}BM$ blends and below the critical angle of the silicon substrate.

Resonant soft X-ray scattering (RSoXS): RSoXS transmission measurements were achieved at beamline 11.0.1.2 at the Advanced Light Source (ALS), Lawrence Berkeley National Laboratory. RSoXS was taken with x-ray photon energy of 284.2 eV for the best contrast and sensitivity. Samples for RSoXS measurements were first prepared on a

PEDOT:PSS modified Si substrate under the same conditions as those used for fabrication of OPV devices, and then transferred to a 1.5 mm × 1.5 mm, 100 nm thick Si_3N_4 membrane supported by a 5 mm × 5 mm, 200 μ m thick Si frame (Norcada Inc.). The calculation of RSoXS intensities, $I(q)$, and PDDFs, $P(r)$, was performed using the generalized indirect Fourier transformation approach[44,45] through the GIFT software program in the PCG software package.

2.8 References

1. Li, G., Zhu, R., & Yang, Y. Polymer solar cells. Nature Photon.**6**, 153-161 (2012).
2. Gunes, S., Neugebauer, H., & Sariciftci, N. S. Conjugated polymer-based organic solar cells.Chem. Rev. **107**, 1324-1338 (2007).
3. Peumans, P., Yakimov, A., & Forrest, S. R. Small molecular weight organic thin-film photodetectors and solar cells. J. Appl. Phys. **93**, 3693-3723 (2003).
4. Halls, J. J. M.et al. Efficient photodiodes from interpenetrating polymer networks. Nature **376**, 498-500 (1995).
5. Shaheen, S. E. et al. 2.5% efficient organic plastic solar cells. Appl. Phys. Lett. **78**, 841 (2001).
6. Brabec, J., Sariciftci, N. S. & Hummelen, J. C. Plastic solar cells. Adv. Funct.Mater. **11**, 15–26 (2001).
7. Clarke, T. M., & Durrant, J. R. Charge photogeneration in organic solar cells. Chem. Rev. **110**, 6736-6767 (2010)
8. Kniepert, J., Schubert, M., Blakesley, J. C., & Neher, D. Photogeneration and Recombination in P3HT/PCBM Solar Cells Probed by Time-Delayed Collection Field Experiments. J. Phys. Chem. C **2**, 700-705 (2011).
9. Li, G. et al. High-efficiency solution processable polymer photovoltaic cells by self-organization of polymer blends. Nature Mater. **4,** 864-868 (2005).

10. Liang, Y. et al. For the bright future—bulk heterojunction polymer solar cells with power conversion efficiency of 7.4%. Adv. Mater. **22**, 135-138 (2010).
11. Dou, L. et al. Tandem polymer solar cells featuring a spectrally matched low-bandgap polymer. Nature Photon. **6**, 180-185 (2012).
12. Chen, H. et al. Polymer solar cells with enhanced open-circuit voltage and efficiency. Nature Photon. **3**, 649-653 (2009).
13. Small, C. E. et al. High-efficiency inverted dithienogermole-thienopyrrolodione-based polymer solar cells. Nature Photon. **6,** 115-120 (2011).
14. He, Z. et al. Enhanced power-conversion efficiency in polymer solar cells using an inverted device structure. Nature Photon. **6**, 593-597 (2012).
15. You, J. et al. A polymer tandem solar cell with 10.6% power conversion efficiency. Nature Commun. **4**, 1446 (2013).
16. Green, M. A. et al. Solar cell efficiency tables (version 39). Prog. Photovolt. Res. Appl. **20**, 12-20 (2012).
17. Li, G. et al. Solvent Annealing Effect in Polymer Solar Cells Based on Poly (3□ hexylthiophene) and Methanofullerenes. Adv. Funct. Mater. **17**, 1636-1644 (2007).
18. Dou, L. et al. Systematic investigation of benzodithiophene-and diketopyrrolopyrrole-based low-bandgap polymers designed for single junction and tandem polymer solar cells. J. Am. Chem. Soc.**134**, 10071-1007 (2012).
19. Liang, Y., & Yu, L. A new class of semiconducting polymers for bulk heterojunction solar cells with exceptionally high performance. Acc. Chem. Res. **43**, 1227-1236 (2010).
20. Hou, J. et al. Synthesis of a low band gap polymer and its application in highly efficient polymer solar cells. J. Am. Chem. Soc.**131**, 15586-15587 (2009).
21. Jankovic, V. et al. Active Layer-Incorporated, Spectrally-Tuned Au/SiO2 Core/Shell Nanorod-Based Light Trapping for Organic Photovoltaics. ACS nano **7**, 3815-3822 (2013).

22. Dou, L. et al. A Selenium-Substituted Low-Bandgap Polymer with Versatile Photovoltaic Applications. Adv. Mater. **25**, 825–831 (2013).

23. Ameri, T., Khoram, P., Min, J., & Brabec, C. J. Organic ternary solar cells: a review. Adv. Mater. **25**, 4245-4266 (2013).

24. Huang, Y. et al. Small-and Wide-Angle X-ray Scattering Characterization of Bulk Heterojunction Polymer Solar Cells with Different Fullerene Derivatives. J. Phys. Chem. C **116**, 10238-10244 (2012).

25. Liang, Y. Y. et al. Development of new semiconducting polymers for high performance solar cells. J. Am. Chem. Soc. **131**, 56–57 (2009).

26. Liang, Y. Y. et al. Highly efficient solar cell polymers developed via fine tuning of structural and electronic properties. J. Am. Chem. Soc. **131**, 7792–7799 (2009).

27. Piliego, C. et al. Synthetic control of structural order in N-alkylthieno [3, 4-c] pyrrole-4, 6-dione-based polymers for efficient solar cells. J. Am. Chem. Soc. **132**, 7595-7597 (2010).

28. Bartelt, J. A. et al.The Importance of Fullerene Percolation in the Mixed Regions of Polymer–Fullerene Bulk Heterojunction Solar Cells. Adv. Energy Mater. **3**, 364–374 (2013).

29. Rivnay, J. et al. Drastic control of texture in a high performance n-type polymeric semiconductor and implications for charge transport. Macromolecules **44**, 5246-5255 (2011).

30. Mozer, A. J. et al. Time-dependent mobility and recombination of the photoinduced charge carriers in conjugated polymer/fullerene bulk heterojunction solar cells. Phys Rev.B **72**, 035217 (2005).

31. Mozer, A. J. et al. Charge transport and recombination in bulk heterojunction solar cells studied by the photoinduced charge extraction in linearly increasing voltage technique. Appl. Phys. Lett. **86**, 112104-112104 (2005).

32. Khlyabich, P. P., Burkhart, B., & Thompson, B. C. Efficient Ternary Blend Bulk Heterojunction Solar Cells with Tunable Open-Circuit Voltage. J. Am. Chem. Soc. **133**, 14534-14537 (2011).

33. Khlyabich, P. P., Burkhart, B., & Thompson, B. C. Compositional Dependence of the Open-Circuit Voltage in Ternary Blend Bulk Heterojunction Solar Cells Based on Two Donor Polymers. J. Am. Chem. Soc. **134**, 9074-9077 (2012).
34. Maurano, A. et al. Recombination dynamics as a key determinant of open circuit voltage in organic bulk heterojunction solar cells: a comparison of four different donor polymers. Adv. Mater. **22**, 4987-4992 (2010).
35. Vandewal, K., Tvingstedt, K., Gadisa, A., Inganäs, O., & Manca, J. V. On the origin of the open-circuit voltage of polymer–fullerene solar cells. Nature Mater.**8**, 904-909 (2009).
36. Street, R. A., Davies, D., Khlyabich, P. P., Burkhart, B., and Thompson, B. C. Origin of the Tunable Open-Circuit Voltage in Ternary Blend Bulk Heterojunction Organic Solar Cells. J. Am. Chem. Soc.**135**, 986-989 (2013).
37. Shuttle, C. G. et al. Experimental determination of the rate law for charge carrier decay in a polythiophene: Fullerene solar cell. Appl. Phys. Lett. **92**, 093311-093311 (2008).
38. Shuttle, C. G. et al. Charge extraction analysis of charge carrier densities in a polythiophene/fullerene solar cell: Analysis of the origin of the device dark current. Appl. Phys. Lett. **93**, 183501-183501 (2008).
39. Shuttle, C. G., Hamilton, R., O'Regan, B. C., Nelson, J. A., & Durrant, J. R. Charge-density-based analysis of the current–voltage response of polythiophene/fullerene photovoltaic devices. Proc. Natl. Acad. Sci. **107**, 16448-16452 (2010).
40. Chen, W. et al. Hierarchical nanomorphologies promote exciton dissociation in polymer/fullerene bulk heterojunction solar cells. Nano Lett. **11**, 3707-3713 (2011).
41. Rivnay, J., Noriega, R., Kline, R. J., Salleo, A., & Toney, M. F. Quantitative analysis of lattice disorder and crystallite size in organic semiconductor thin films. Phys Rev.B **84**, 045203 (2011).
42. Chen, W., Nikiforov, M. P., Darling, S. B. Morphology characterization in organic and hybrid solar cells. Energy Environ. Sci. **5**, 8045-8074 (2012).

43. Löslein, H. et al. Transient Absorption Spectroscopy Studies on Polythiophene–Fullerene Bulk Heterojunction Organic Blend Films Sensitized with a Low-Bandgap Polymer. Macromol. Rapid. **34**, 1090-1097 (2013).

44. Brunner-Popela, J., Glatter, O. Small-Angle Scattering of Interacting Particles. I. Basic Principles of a Global Evaluation Technique. J. Appl. Crystallogr. **30**, 431-442 (1997).

45. Weyerich, B., Brunner-Popela, J. Glatter, O. Small-angle scattering of interacting particles. II. Generalized indirect Fourier transformation under consideration of the effective structure factor for polydisperse systems. J. Appl. Crystallogr. **32**, 197-209 (1999).

Chapter 3 Au/SiO2 Core/Shell Nanorod-Based Light Trapping for Organic Photovoltaics

In this work, we demonstrated that incorporation of octadecyltrimethoxysilane (OTMS) functionalized, spectrally tuned, gold/silica (Au/SiO_2) core/shell nanospheres and nanorods into the active layer of an organic photovoltaic (OPV) device led to an increase photo conversion efficiency (PCE). The silica shell layer was added onto the Au core nanospheres and nanorods in order to provide an electrically insulating surface that wouldn't interfere with carrier generation and transport inside the active layer. Functionalization of the Au/SiO_2 core/shell nanoparticles with the OTMS organic ligand was necessary in order to transfer the Au/SiO_2 core/shell nanoparticles from an ethanol solution into an OPV polymer-compatible solvent such as dichlorobenzene (DCB). The OTMS-functionalized Au/SiO_2 core/shell nanorods and nanospheres were incorporated into the active layers of two OPV polymer systems: a poly(3-hexylthiophene):[6,6]-phenyl-C61-butyric acid methyl ester (P3HT:$PCB_{60}M$)-based OPV device and a poly[2,6-4,8-di(5-ethylhexylthienyl)benzo[1,2-b;3,4-b]dithiophene-alt-5-dibutyloctyl-3,6-bis(5-bromothiophen-2-yl) pyrrolo[3,4-c]pyrrole-1,4-dione] (PBDTT-DPP:$PC_{60}BM$)-based OPV device. For the P3HT:$PC_{60}BM$ polymer with a band edge ~700 nm, the addition of the core/shell nanorods with an aspect ratio (AR)~2.5 (extinction peak, λ_{peak}=670 nm) resulted in an 7.1% improvement in photon conversion efficiency (PCE), while for the PBDTT-DPP:$PC_{60}BM$ polymer with a band edge ~860 nm, the addition of core/shell nanorods of AR~4 (extinction peak, λ_{peak}=830 nm) resulted in a 14.4% improvement in PCE. The addition of Au/SiO_2 core/shell nanospheres to the P3HT:$PC_{60}BM$-polymer resulted in a 2.7% improvement in PCE, while their addition to a PBDTT-DPP:$PC_{60}BM$

polymer resulted in a 9.1% improvement. The PCE and J_{sc} enhancements were consistent with external quantum efficiency (EQE) measurements and the EQE enhancements spectrally matched the extinction spectra of Au/SiO_2 nanospheres and nanorods in both OPV polymer systems.

3.1 Objective and experimental design

Given that its active layer is amenable to simple solution processing, organic photovoltaic (OPV) technology is an inexpensive, flexible and lightweight option for solar energy conversion. Research in organic solar cells started in the early 1980s and focused on Schottky junctions with low work-function metals and p-n junctions with p-type organic semiconducting polymers and inorganic n-type semiconductors.[1-5] Interest in the field intensified after Tang et al. demonstrated an OPV device in 1986 with a 0.95% efficiency using organic polymers as both donors and acceptors.[6] Other breakthroughs in OPV technology came with the introduction of buckminsterfullerene (C60) and its derivatives such as [6,6]-phenyl-C60-butyric acid methyl ester (PC60BM) as n-type organic materials by Sariciftci et al.[7,8] and with the development of the bulk heterojunction (BHJ) by Hiramoto et al.[9] Seminal BHJ OPV papers using poly(2-methoxy-5(20-ethylhexyloxy)-1,4-phenylenevinylene (MEH-PPV) as the donor molecule and PC60BM as the acceptor molecule were published by the Heeger[10] and Friend[11] groups independently in 1995. As research in the field continued, studies revealed that the nanoscale morphology of the active layer of OPV devices was critical for optimizing their efficiency.[12,13] Numerous strategies, including solvent selection,[14-16] thermal annealing,[17] and the incorporation of various additives[13] have led to improved active layer morphologies and consequently further

improvements in photon conversion efficiencies (PCEs).[18] High carrier mobility donor polymers such as poly(3-hexylthiphene) (P3HT)[19] and low-bandgap polymers such as poly[2,6-4,8-di(5-ethylhexylthienyl)benzo[1,2-b;3,4-b]dithiophene-alt-5-dibutyloctyl-3,6-bis(5-bromothiophen-2-yl) pyrrolo[3,4-c]pyrrole-1,4-dione] (PBDTT-DPP) which have absorption wavelengths that extend up to ~850 nm have also led to PCE improvements.[20] Currently, a PCE of over 9% for single-junction OPVs has been achieved by Mitsubishi Chemical[21] and a NREL-certified PCE of 10.6% has been achieved for tandem cells by Li et al.[20]

Photons absorbed by an OPV device can only generate current if they are absorbed near donor–acceptor interfaces such that dissociation occurs prior to dissipative recombination. Since the carrier mobility is small in photo-active polymers (on the order of 10-4 cm2/Vs, or less), it is common to use rather thin films (100nm or less) in order to achieve efficient carrier extraction.[22] The use of such thin layers means a significant portion of the incident photon flux remains unharvested; it also means that the light absorption efficiencies of OPV devices can be improved.

Light trapping refers to the various methods used to increase the distance over which incident photons interact with photovoltaic (PV) materials, thereby increasing the likelihood of photon absorption. From a ray-optics perspective, conventional light trapping employs total internal reflection by patterning the entrance or exit interfaces of the solar cell and redirecting the incident light into the PV active layer.[23] In thick crystalline silicon (Si) solar cells, light trapping is typically achieved with the use of patterned structures that have features on the scale of the wavelength of light.[24] Since the active layers in organic cells have thicknesses that are far smaller than the wavelength of light, the relatively large-

scale geometries used in traditional light trapping designs are not suitable for OPVs.[25] For OPV applications, light trapping techniques that rely on structures compatible with the scale of OPV films, in other words, at a scale less than 100 nm are needed.[26]

One light trapping method that shows promise for OPV applications involves the use of noble metal (mainly gold (Au) or silver (Ag)) nanoparticles.[25] Noble metal nanoparticles are capable of confining resonant photons in such a manner as to induce coherent surface plasmon oscillation of their conduction band electrons.[27] At the resonant frequency, termed the local surface plasmon resonance (LSPR), a large enhancement of the nanoparticle's light absorption and scattering properties occurs.[28] For example, an Ag nanoparticle in air has a scattering cross section that is around ten times the geometrical cross-sectional area of the particle; hence, a substrate covered with a 10% areal density of Ag particles could ideally absorb and scatter all the light incident on the substrate.[29] Indeed, noble metal nanoparticles deposited on the top of thin film solar cells have been shown to preferentially scatter light into the high-index substrate, leading to enhanced coupling with the underlying semiconductor and thus a reduced reflectance over a broad spectral range.[30]

Light trapping with Au and Ag nanoparticles for OPVs has been demonstrated by various groups.[31-33] By incorporating Au nanospheres (~45 nm diameter) into the poly(ethylenedioxythiophene):polystyrenesulphonate (PEDOT:PSS) buffer layer of a P3HT:PC60BM OPV device, Morfa et al. increased the PCE of the device from 1.3% to 2.2%.[31] Qiao et al. showed that Au nanoparticles (~15 nm diameter) introduced into the PEDOT:PSS layer of an OPV device using poly(2-methoxy-5(20-ethylhexyloxy)-1,4-phenylenevinylene (MEH-PPV) as the active layer enhanced the PCE from 1.99% to 2.36%.[32] Wu et al. demonstrated that incorporating Au nanoparticles (~45 nm diameter)

into the anodic buffer layer of a P3HT:PC60BM OPV device improved the PCE from 3.57% to 4.24%.[33] More recently, Au nanoparticles (~72 nm diameter) were deposited in the interconnecting layer of an inverted tandem polymer solar cell, resulting in a 20% increase in PCE (from 5.22% to 6.24%).[34] In all of these reports, because the plasmonic nanoparticles were inserted relatively far from the active organic layers of the OPV devices, the documented absorption enhancements arose from the light scattering properties of the Au nanoparticles and failed to exploit the near-field enhanced LSPR modes.[26] As theoretical studies have shown, embedding plasmonic nanoparticles into the active layer of an OPV device can capitalize on both the light scattering effect and the enhanced LSPR near field.[35,36]

Currently, there are only a few reports documenting incorporation of plasmonic materials into OPV active layers. Szeremeta et al. showed that Cu nanoparticles (20 nm) embedded inside P3HT layers enhanced the dissociation of excitons without increasing the P3HT optical absorption.[37] Wang et al. demonstrated improved PCEs in three different polymer systems resulting from incorporation of Au nanoparticles in the active layer but the observed EQE enhancements were broadband, indicating that the enhancements were due to light scattering and not due to the narrow band LSPR near field.[38] Mei et al. incorporated Ag nanoparticles into the active layer of a P3HT:PC60BM OPV device and found that while their addition into the active layer significantly enhanced carrier mobility, it decreased the total extracted carrier density.[39] A potential way to address some of these issues is to coat the noble metal nanoparticles with a thin layer of SiO2 rendering their surfaces insulating yet still retain their attractive optical properties.

The frequency of light that is resonantly absorbed and scattered from a nanoparticle is another important consideration in optimizing OPV device performance. Since different OPV polymers have different light absorption frequency bands, it is of interest to develop a light trapping technique that can be tailored to specific OPV polymers. The peak extinction frequency of noble metal nanospheres is around 520 nm and varies ~20 nm depending on the nanosphere size.[29] In Au nanorods on the other hand, free electrons oscillate along both the long and short axes of the rod, resulting in two resonance bands: a band of wavelengths resulting from electron oscillations along the long axis, which, depending on the nanorod aspect ratio (AR) ranges between ~600 nm to ~900 nm, and, a second, weaker band at ~520 nm resulting from electron oscillations along the short axis (similar to nanospheres).[40] Incorporating Au nanorods of different ARs (and hence different peak extinction wavelengths) into OPV active layers can be utilized to achieve LSPR near field absorption enhancements over a large range of wavelengths.

3.2 Results and discussions

In order to study the viability of this approach, Au/SiO2 core/shell nanospheres and nanorods were incorporated into the active layers of two polymer OPV systems: P3HT:PC60BM and PBDTT-DPP:PC60BM. We hypothesized that the greatest enhancement due to the LSPR near field would be observed in spectral regions where the OPV polymer absorbs poorly and the lowest enhancement would be observed in spectral regions where the OPV polymer absorbs efficiently. To investigate this hypothesis, EQE measurements on OPV devices with spectrally-tuned Au/SiO2 nanoparticles were performed. For the P3HT:PC60BM system, Au/SiO2 nanospheres with a peak extinction

of ~540 nm (matching a spectral region of high polymer absorption) and AR~2.5 Au/SiO2 nanorods with a peak extinction of ~670 nm (matching a spectral region of poor polymer absorption at the band edge of the P3HT:PC60BM) were synthesized. For the PBDTT-DPP:PC60BM system, Au/SiO2 nanospheres with a peak extinction of ~540 nm (matching a spectral region of moderate polymer absorption) and AR~4 Au/SiO2 nanorods with a peak extinction of ~830 nm (matching a spectral region of poor polymer absorption at the OPV polymer band edge) were synthesized. The SiO2 shell thickness in all samples was ~10 nm. Short circuit current (Jsc), open circuit voltage (Voc), and external quantum efficiency (EQE) measurements were performed on the devices. Blending the Au/SiO2 nanospheres and nanorods in the BHJ resulted in enhanced Jsc and PCE in both the P3HT:PC60BM and PBDTT-DPP:PC60BM devices compared to the reference devices (Supplemental Information, Tables S.1.-S.4.). Figure 1(i) shows the transmission electron microscopy (TEM) images of Au nanospheres (A), AR~2.5 Au nanorods (B), AR~4 Au nanorods (C), Au/SiO2 nanospheres (D), AR~2.5 Au/SiO2 nanorods (E), AR~4 Au/SiO2 nanorods (F). Figure 1(ii) shows the extinction spectra of bare Au nanospheres, AR~2.5 nanorods and AR~4 nanorods in water (corresponding TEM images are A-C) plotted with the extinction spectra of Au/SiO2 core/shell nanorods in di-chlorobenzene (corresponding TEM image are D-F). Figure 3.1(iii) shows normalized extinction spectra of solutions D and E plotted with a normalized EQE spectrum of P3HT:PC60BM while Figure 3.1(iv) shows a normalized EQE spectrum of PBDTT-DPP:PC60BM plotted with normalized extinction spectra of solutions D and F. Figure 1(v) show the reference and plasmonic OPV device EQE spectra for the P3HT:PC60BM while the EQE spectra of plasmonic and

reference devices using the PBDTT-DPP:PC60BM polymer system is shown in Figure 3.1(vi)

(i)

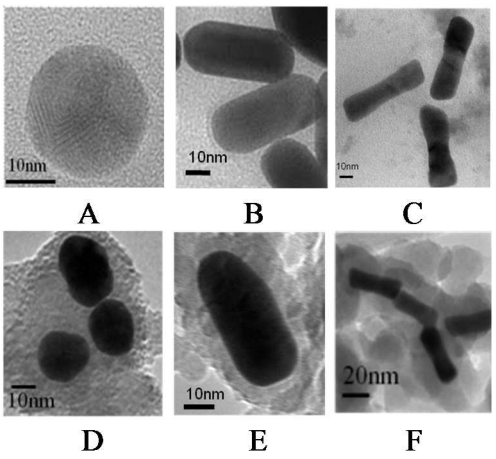

(ii)

(iii)

(iv)

(v)

(vi)

Figure 3-1(i) TEM images of: (A) Au nanospheres in water (B) Au/SiO2 core/shell nanospheres in DCB (C) Au nanorods of AR~2.5 in water (D) Au/SiO2 core/shell nanorods of AR ~2.5 in DCB (E) Au nanorods of AR~4 in water (F) Au/SiO2 core/shell nanorods of AR ~4 in DCB (ii) Extinction spectra of corresponding colloidal solutions A-F (iii) Normalized EQE of

P3HT:PC60BM plotted with normalized extinction spectra of B and F (iv) Normalized EQE spectrum of PBDTT-DPP:PC60BM devices with D and F and reference devices

The reference EQE spectra were subtracted from the plasmonic OPV device in order to obtain EQE enhancement values (ΔEQE). Figure 2 shows EQE enhancements of OPV devices plotted with the extinction spectra of Au/SiO2 nanospheres and nanorods embedded in their active layers.

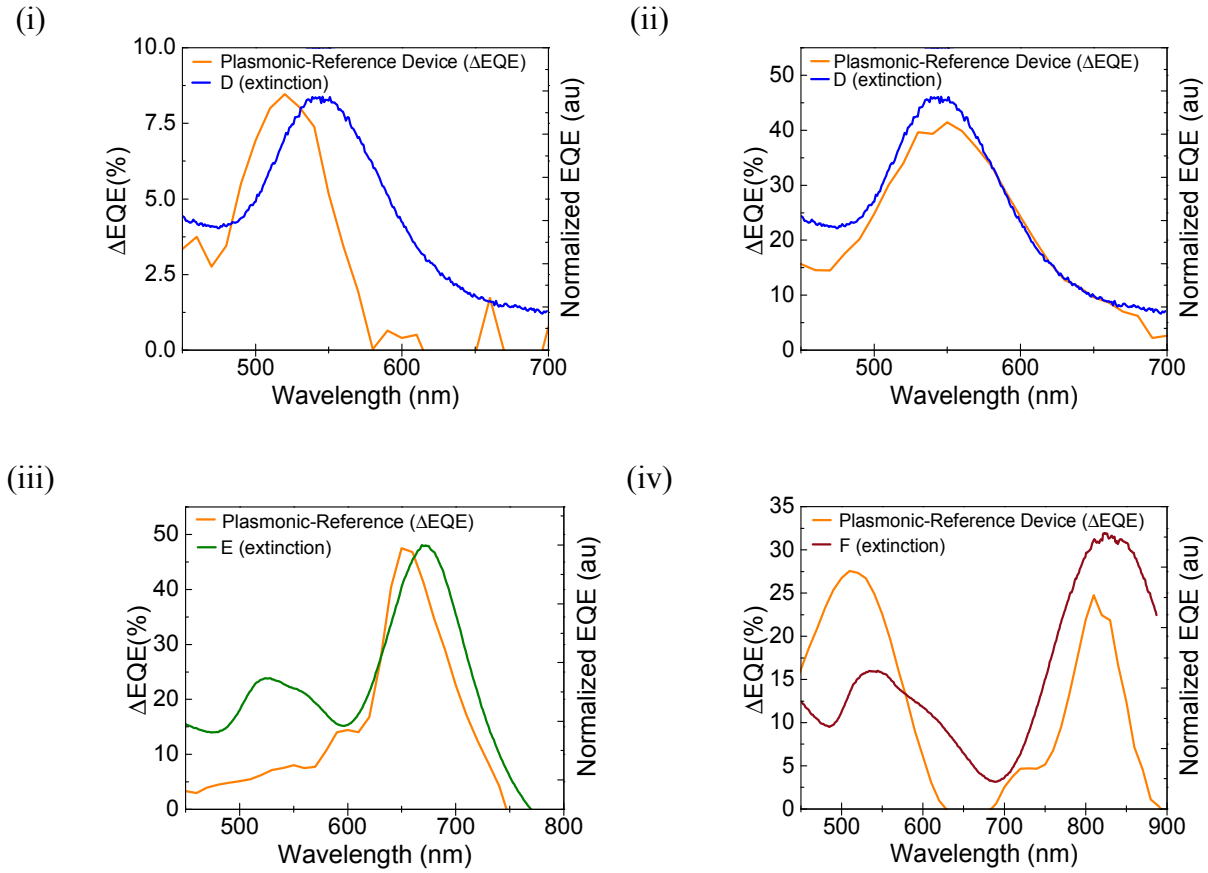

Figure 3-2 Spectral EQE enhancements of (i) P3HT-based device with Au/SiO2 nanospheres (solution D) (ii) PBDTT-DPP-based device with solution Au/SiO2 nanospheres (solution D) (iii) P3HT-based device with AR~2.5 Au/SiO2 core/shell nanorods (solution E) (iv) PBDTT-DPP-based device with AR~4 Au/SiO2 core/shell nanorods (solution F)

EQE enhancements in both polymer systems spectrally matched the extinction spectra of the active layer-incorporated Au/SiO2 core/shell nanospheres and nanorods. AR~4 Au/SiO2 core/shell nanorods with extinction peaks matched to the band edges of the PBDTT-DPP:PC60BM OPV systems showed the highest EQE enhancement factors while Au/SiO2 nanospheres incorporated in a P3HT:PC60BM system showed the lowest performance enhancement. In the low band gap polymer system, PBDTT-DPP:PC60BM, we found that the improvement was in two spectral regions: one that matched the longitudinal oscillation mode of the Au/SiO2 nanorods, and another one that matched the transverse oscillation mode of the Au/SiO2 nanorods. The mismatch between the EQE of the P3HT:PC60BM polymer system and the extinction spectrum of the Au/SiO2 nanospheres requires further investigation.

A concentration study was also conducted and revealed that OPV device performance depended sensitively on the amount of Au/SiO2 core/shell nanospheres or nanorods incorporated into the active layer. Increasing the amount of Au/SiO2 nanoparticles led to an initial increase in solar cell PCE. As the Au/SiO2 concentration increased, however, a drop in device performance was observed. For the P3HT:PC60BM system, the optimal Au/SiO2 nanosphere concentration was 0.4 mg/ml and 0.6 mg/ml for the Au/SiO2 nanorods; concentrations of nanospheres or nanorods greater than 2 mg/ml resulted in OPV device performance degradation. The optimum Au/SiO2 core/shell nanosphere concentration for the PBDTT-DPP:PC60BM system was 0.1 mg/ml and 0.2 mg/ml for the Au/SiO2 nanorods (AR~4); concentrations of either nanospheres or nanorods greater than 1 mg/ml resulted in OPV device performance degradation. The results of the concentration study are summarized in Figure 3.3.

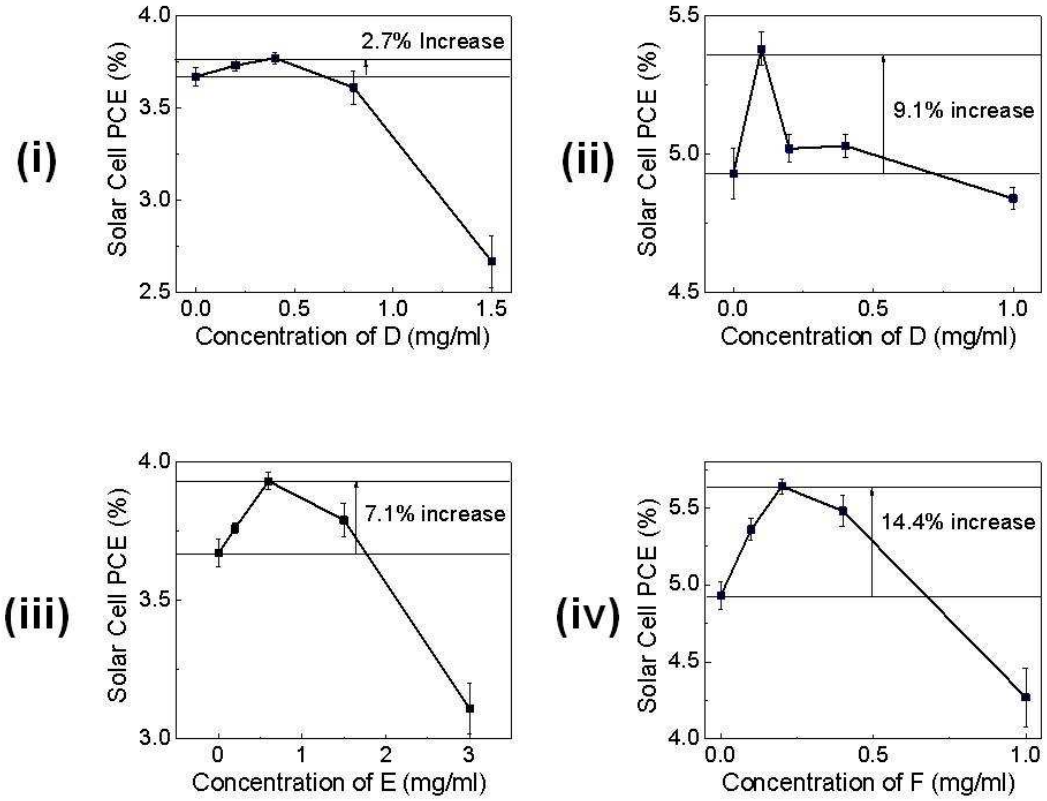

Figure 3-3Solar cell PCE as a function of Au/SiO2 nanosphere and nanorod concentrations for (i) D in P3HT:PC60BM (ii) D in PBDTT-DPP:PC60BM (iii) E in P3HT:PC60BM and (iv) F in PBDTT-DPP:PC60BM

In conclusion, we achieved improvements in the PCE and Jsc of two OPV polymer systems by incorporating resonant light absorption and scattering Au/SiO2 core/shell nanorods in their active regions. For the P3HT:PC60BM, the incorporation of Au/SiO2 core/shell nanospheres (~540nm peak extinction) in the active layer led to a 2.7% increase in PCE. Active layer incorporation of Au/SiO2 nanorods with a peak extinction wavelength ~670 nm matched to the P3HT:PC60BM polymer band edge led to a 7.1% increase in OPV device PCE. For the PBDTT:PC60BM system, active layer incorporation of Au/SiO2 nanospheres with peak extinction wavelengths ~540 nm led to a 9.1% increase in PCE while Au/SiO2 core/shell nanorods with extinction peaks ~830 nm, matched to the band

edge of PBDTT-DPP:PC60BM showed the highest PCE increases (14.4% increase in PCE). The results indicate that spectral tuning of the active layer plasmonic light trapping particles is a key consideration for active layer incorporated plasmonic light trapping in OPVs. In order to maximize light trapping in practical applications, the extinction peaks of active layer-incorporated Au/SiO2 nanoparticles should spectrally match wavelength regions of poor OPV light absorption. In spectral regions where the OPV polymer absorbs light efficiently, the effect of incorporating spectrally-matched plasmonic light trapping nanoparticles was found to be small.

Our data also indicates that plasmonic OPV device performance sensitively depends on the Au/SiO2 core/shell nanoparticle concentration incorporated in the active layer. Device performance was found to increase with the addition of core/shell nanoparticles up to a certain concentration (varies depending on the polymer and the nanoparticle geometry and size). Using higher concentrations of core/shell nanoparticles was found to degrade device performance. AFM analysis indicated that addition of high concentrations of Au/SiO2 core/shell particles in the active layer led to the higher surface roughness and potential disruption of the OPV polymer morphology.

The results of this study support the viability of our approach of increasing OPV solar cell device efficiencies by incorporating spectrally-tuned Au/SiO2 core/shell nanorods in OPV active layers. Our data indicates that plasmonic enhancement should target spectral regions where the OPV cell absorbs poorly and that the concentration of the plasmonic light trapping agents should be carefully controlled.

3.3 Experimental details

Au/SiO2 core/shell Nanoparticle Synthesis:

The synthesis of Au nanospheres was achieved by reducing gold chloride ($HAuCl_4$) with sodium borohydride ($NaBH_4$) in the presence of a surfactant (cetyltrimethylammoniumbromide (CTAB)). To prepare 10.6 ml of Au nanospheres, 5 ml of a 0.5 mM $HAuCl_4$ solution were mixed with 5 ml of a 0.2 M CTAB solution and then 0.6 ml of ice cold $NaBH_4$ was added to initiate the reaction. The protocol produces 2-5 nm diameter nanospheres which increased in size to ~20 nm diameter nanospheres over a few days. Synthesis of Au nanorods required preparation of two solutions: a seed solution and a growth solution. The seed solution was prepared by mixing 5 ml of 0.5 mM $HAuCl_4$, 5 ml of 0.2M CTAB and 0.6 ml of 0.1 M ice cold $NaBH_4$. A solution of nanorods with a plasmon resonance of ~650 nm was prepared using a growth solution that contained 0.6 ml of 0.01M $AgNO_3$, 20 ml of 0.5 mM $HAuCl_4$, 20 ml of 0.2 M CTAB and 0.7 ml of 0.77 M ascorbic acid. To prepare nanorods with an extinction peak of ~800 nm, 0.9 ml of 0.01 M $AgNO_3$ was used instead of 0.6 ml of 0.01 M $AgNO_3$ in the growth solution. The growth process was initiated by injecting 26 μl of seed solution into the growth solution at a temperature of 27oC. The reaction took approximately two hours to come to completion. To coat the Au nanorods with SiO_2, a literature protocol developed by Pastoriza-Santos was followed.41 The nanorods were first rendered vitreophyllic by treating them with consecutive polyelectrolyte layers. Au metal has little affinity for SiO_2 because unlike most other metals, it does not form a passivating oxide film in solution. Furthermore, the CTAB stabilizing surfactant interferes with the SiO_2 coating process. In order to replace the CTAB stabilizer and modify the Au nanorod surface chemistry, consecutive polyelectrolyte layers were adsorbed onto the metal surface. This process proceeded in the following manner. First, the as-synthesized, CTAB-stabilized Au rods were centrifuged,

the precipitate was redissolved in 3 ml of distilled water and then added to 3 ml of an aqueous solution containing poly-styrene sulfonate (PSS) (2 mg/mL and 6 mM NaCl) and stirred for approximately three hours. The PSS-modified particles were centrifuged twice to remove any excess PSS and redispersed in 3 ml of deionized water. The dispersion was then added drop-wise under vigorous stirring to 3 ml of an aqueous solution of poly(anilline hydrochloride) (PAH) of (2 mg/ml and 6 mM NaCl). PAH adsorption was allowed to proceed for three hours. The sample was then centrifuged to remove excess polyelectrolyte and redispersed in 3 mL of deionized water. Finally, 3 ml of the PSS/PAH functionalized Au spheres were added to a polyvinylpyrrolidone (PVP) solution (4 mg/ml). The mixture was stirred for approximately twelve hours, centrifuged to remove any excess polymer, and redispersed in 0.2 mL of deionized water. This aqueous dispersion of PVP-coated nanoparticles was then added drop-wise and under vigorous stirring to 2 ml of isopropyl-alcohol (IPA). Once the Au nanoparticles were transferred into IPA, SiO2 coating was completed through the adjustment of the pH and addition of tetra-ethyl-orthosilicate (TEOS). The pH was adjusted to 10 by adding 1.5 ml, 4 vol% NH3 in IPA (27% in water). Finally, 0.4 ml of TEOS (1 vol% in ethanol) was added under gentle stirring and the reaction was allowed to proceed for approximately twelve hours.

In order to dissolve the Au/SiO2 core/shell nanorods in an OPV-compatible solvent, like dichlorobenzene, functionalization with octadecyltrimethoxysilane (OTMS) was performed. The Au/SiO2 core/shell nanorods were centrifuged and redissolved in 3 ml of ethanol containing 30 µl of NH4OH (32%). 300 µl of OTMS chloroform solution (3%) was added drop-wise with vigorous stirring and functionalization of the SiO2 surface was achieved by hydrolysis of the methoxy groups and condensation of the resulting silane

groups with SiOH groups on the SiO2 surface. Transmission electron microscopy (TEM) using and FEI TF20 was used to confirm the morphology of the synthesized Au/SiO2 core/shell nanorods, while UV Vis spectroscopy was used to determine the extinction spectra of the nanorod solutions.

Plasmonic OPV Device Fabrication

Polymer reference solutions consisted of 20 mg/mL of P3HT:PC60BM (1:1 weight ratio) and 6 mg/mL PBDTT-DPP:PC60BM (1:2.5 weight ratio). The plasmonic P3HT:PC60BM solar cell device solution was prepared by adding a solution of the OTMS-functionalized Au/SiO2 core/shell nanorods (AR~2.5) to the P3HT:PC60BM solution so that the final concentration of the nanorods was 0.6 mg/mL. The plasmonic PBDTT-DPP:PC60BM solar cell device solution was prepared by mixing the OTMS-functionalized Au/SiO2 core/shell nanorod solution (AR~4) with the PBDTT-DPP:PC60BM solution so that the final concentration of Au/SiO2 core/shell nanorods was 0.2 mg/mL.

All the devices in this manuscript had the same structure: indium tin oxide (ITO)/ poly(ethylenedioxythiophene):polystyrenesulphonate (PEDOT:PSS) (4083) /active layer / Calcium (Ca) / Aluminum (Al). The PEDOT:PSS was pre-coated onto the ITO substrate and baked at 120oC for fifteen minutes before spin-casting the solutions. The P3HT:PC60BM-based devices were spin-coated at 800 rpm for 40 seconds after which the wet films remained in the petri dishes until they dried (the color of the films changed from orange to dark-red). This solvent annealing process has been demonstrated to attain an optimized morphology for P3HT:PC60BM-based organic solar cell devices. The PBDTT-DPP:PC60BM-based devices were fabricated by spin-casting at 1800 rpm for 80 seconds with no other treatment. A bilayer cathode containing a Ca layer (20 nm) and a subsequent

Al layer (100 nm) were deposited by thermal evaporation under high vacuum (<3·10-6 Torr). The active layer thickness of the P3HT:PC60BM-based devices was ~210 nm while the thickness of the PBDTT-DPP:PC60BM-based devices was ~90nm.The thickness was measured by Vecoo Dektak 150 profiler.

3.4 References

1. Loutfy, R. O.; Sharp, J. H. Photovoltaic Properties of Metal-Free Phthalocyanines. I. Al/H2Pc Schottky barrier solar cells. The Journal of Chemical Physics 1979, 71, 1211-1217.

2. Morel, D. L.; Ghosh, A. K.; Feng, T.; Stogryn, E. L.; Purwin, P. E.; Shaw, R. F.; Fishman, C. High-Efficiency Organic Solar Cells. Applied Physics Letters 1978, 32, 495-497.

3. Wagner, H. J.; Loutfy, R. O., Photoelectric properties of CdS--MgPc heterojunction solar cells. Journal of Vacuum Science and Technology 1982, 20, 300-304.

4. Yokoyama, M.; Endo, Y.; Matsubara, A.; Mikawa, F. H., Mechanism of extrinsic carrier photogeneration in poly-N-vinylcarbazole. II. Quenching of exciplex fluorescence by electric field. The Journal of Chemical Physics 1981, 75, 3006-3011.

5. Yokoyama, M.; Shimokihara, S.; Matsubara, A.; Mikawa, H. Extrinsic carrier photogeneration in poly-N-vinylcarbazole. III. CT Fluorescence Quenching by an Electric Field. The Journal of Chemical Physics 1982, 76, 724-728.

6. Tang, C. W. 2-Layer Organic Photovoltaic Cell. Applied Physics Letters 1986, 48, 183-185.

7.Sariciftci, N. S.; Braun, D.; Zhang, C.; Srdanov, V. I.; Heeger, A. J.; Stucky, G.; Wudl, F. Semiconducting Polymer-Buckminsterfullerene Heterojunctions: Diodes, Photodiodes, and Photovoltaic cells. Applied Physics Letters 1993, 62, 585-587.

8. Sariciftci, N. S.; Smilowitz, L.; Heeger, A. J.; Wudl, F. Photoinduced Electron-Transfer from a Conducting Polymer to Buckminsterfullerene. Science 1992, 258, 1474-1476.

9. Hiramoto, M.; Fujiwara, H.; Yokoyama, M. P-I-N like Behavior in Three-Layered Organic Solar Cells having a Co-Deposited Interlayer of Pigments. Journal of Applied Physics 1992, 72, 3781-3787.

10. Yu, G.; Gao, J.; Hummelen, J. C.; Wudl, F.; Heeger, A. J. Polymer Photovoltaic Cells: Enhanced Efficiencies via a Network of Internal Donor-Acceptor Heterojunctions. Science 1995, 270, 1789-1791.

11. Marks, R. N.; Halls, J. J. M.; Bradley, D. D. C.; Friend, R. H.; Holmes, A. B. The Photovoltaic Response in Poly(p-phenylene Vinylene) Thin-Film Devices. Journal of Physics: Condensed Matter 1994, 6, 1379-1383.

12. Goetzberger, A.; Hebling, C.; Schock, H.W. Photovoltaic Materials, History, Status and Outlook. Materials Science and Engineering: Reports 2003, 40, 1-46.

13. Li, W. W.; Zhou, Y.; Andersson, B. V.; Andersson, L. M.; Thomann, Y.; Veit, C.; Tvingstedt, K.; Qin, R. P.; Bo, Z. S.; Inganas, O.; Wurfel, U.; Zhang, F. L. The Effect of Additive on Performance and Shelf-Stability of HSX-1/PCBM Photovoltaic Devices. Organic Electronics 2011, 12, 1544-1551.

14. Duong, D. T.; Walker, B.; Lin, J.; Kim, C.; Love, J.; Purushothaman, B.; Anthony, J. E.; Nguyen, T. Q. Molecular solubility and Hansen Solubility Parameters for the Analysis of Phase Separation in Bulk Heterojunctions. Journal of Polymer Science Part B-Polymer Physics 2012, 50, 1405-1413.

15. Fang, G.; Liu, J.; Fu, Y. Y.; Meng, B.; Zhang, B. H.; Xie, Z. Y.; Wang, L. X. Improving the Nanoscale Morphology and Processibility for PCDTBT-based Polymer Solar Cells via Solvent Mixtures. Organic Electronics 2012, 13, 2733-2740.

16. Song, Y.; Ryu, S. O. The Effect of Solvent Systems on the Electrical Performance of P3HT:PCBM-C61 Photoactive Layers. Journal of Nanoelectronics and Optoelectronics 2012, 7, 549-553.

17. Ma, W.; Yang, C.; Gong, X.; Lee, K.; Heeger, A. J. Thermally Stable, Efficient Polymer Solar Cells with Nanoscale Control of the Interpenetrating Network Morphology. Advanced Functional Materials 2005, 15, 1617-1622.

18. Brady, M. A.; Su, G. M.; Chabinyc, M. L. Recent Progress in the Morphology of Bulk Heterojunction Photovoltaics. Soft Matter 2011, 7, 11065-11077.

18. Padinger, F.; Rittberger, R. S.; Sariciftci, N. S. Effects of Postproduction Treatment on Plastic Solar Cells. Advanced Functional Materials 2003, 13, 85-88.

20. Li, G.; Zhu, R.; Yang, Y. Polymer solar cells. Nature Photonics 2012, 6, 153-161.

21. Service, R. F. Outlook Brightens for Plastic Solar Cells. Science 2011, 332, 293-295.

22.Park, S. H.; Roy, A.; Beaupre, S.; Cho, S.; Coates, N.; Moon, J. S.; Moses, D.; Leclerc, M.; Lee, K.; Heeger, A. J. Bulk Heterojunction Solar Cells with Internal Quantum Efficiency Approaching 100% Nature 2009, 3, 297-302.

23. Deckman, H. W.; Roxlo, C. B.; Yablonovitch, E. Maximum statistical increase of optical absorption in textured semiconductor films. Optics Letters 1983, 8, 491-493.

24. Battaglia, C.; Hsu, C.-M.; Söderström, K.; Escarré, J.; Haug, F.-J.; Charrière, M.; Boccard, M.; Despeisse, M.; Alexander, D. T. L.; Cantoni, M.; Cui, Y.; Ballif, C. Light Trapping in Solar Cells: Can Periodic Beat Random? ACS Nano 2012, 6, 2790-2797.

25. Atwater, H. A.; Polman, A. Plasmonics for Improved Photovoltaic Devices. Nature 2010, 9, 205-213.

26. Qiaoqiang, G.; Bartoli, F. J.; Kafafi, Z. H. Research Highlights on Organic Photovoltaics and Plasmonics. Photonics Journal, IEEE 2012, 4, 620-624.

27. Huang, X.; Neretina, S.; El-Sayed, M. A. Gold Nanorods: From Synthesis and Properties to Biological and Biomedical Applications. Advanced Materials 2009, 21, 4880-4910.

28. Chen, H.; Shao, L.; Li, Q.; Wang, J., Gold Nanorods and their Plasmonic Properties. Chemical Society Reviews 2013. 42, 2679-2724.

29. Catchpole, K. R.; Polman, A., Plasmonic Solar Cells. Optics Express 2008, 16, 21793-21800.

30. Spinelli, P.; Ferry, V. E.; Groep, J. v. d.; Lare, M. v.; Verschuuren, M. A.; Schropp, R. E. I.; Atwater, H. A.; Polman, A. Plasmonic Light Trapping in Thin-Film Si solar Cells. Journal of Optics 2012, 14, 024002-024013.

31. Morfa, A. J.; Rowlen, K. L.; Reilly, T. H.; Romero, M. J.; van de Lagemaat, J. Plasmon-Enhanced Solar Energy Conversion in Organic Bulk Heterojunction Photovoltaics. Applied Physics Letters 2008, 92, 13504-13505.

32. Qiao, L.; Wang, D.; Zuo, L.; Ye, Y.; Qian, J.; Chen, H.; He, S. Localized Surface Plasmon Resonance Enhanced Organic Solar Cell with Gold Nanospheres. Applied Energy 2011, 88, 848-852.

33. Wu, J.-L.; Chen, F.-C.; Hsiao, Y.-S.; Chien, F.-C.; Chen, P.; Kuo, C.-H.; Huang, M. H.; Hsu, C.-S. Surface Plasmonic Effects of Metallic Nanoparticles on the Performance of Polymer Bulk Heterojunction Solar Cells. ACS Nano 2011, 5, 959-967.

34. Yang, J.; You, J. B.; Chen, C. C.; Hsu, W. C.; Tan, H. R.; Zhang, X. W.; Hong, Z. R.; Yang, Y. Plasmonic Polymer Tandem Solar Cell. ACS Nano 2011, 5, 6210-6217.

35. Lee, J.-Y.; Peumans, P. The Origin of Enhanced Optical Absorption in Solar Cells with Metal Nanoparticles Embedded in the Active layer. Optics Express 2010, 18, 10078-10087.

36. Qu, D.; Liu, F.; Huang, Y.; Xie, W.; Xu, Q. Mechanism of Optical Absorption Enhancement in Thin Film Organic Solar Cells with Plasmonic Metal Nanoparticles. Opt. Express 2011, 19, 24795-24803.

37. Szeremeta, J.; Nyk, M.; Chyla, A.; Strek, W.; Samoc, M. Enhancement of photoconduction in a conjugated polymer through doping with copper nanoparticles. Optical Materials 2011, 33, 1372-1376.

38. Wang, D. H.; Kim, D. Y.; Choi, K. W.; Seo, J. H.; Im, S. H.; Park, J. H.; Park, O. O.; Heeger, A. J. Enhancement of Donor–Acceptor Polymer Bulk Heterojunction Solar Cell Power Conversion Efficiencies by Addition of Au Nanoparticles. Angewandte Chemie International Edition 2011, 50, 5519-5523.

39. Mei, X.; Lu, L.; Tremolet de Villers, B. J.; Huajun, S.; Jinfeng, Z.; Zhibin, Y.; Stieg, A. Z.; Qibing, P.; Schwartz, B. J.; Wang, K. L. Charge-Carrier Dynamics in Hybrid Plasmonic Organic Solar Cells with Ag Nanoparticles. Applied Physics Letters 2011, 98, 3302-3305.

40.Huang, X.; Jain, P. K.; El-Sayed, I. H.; El-Sayed, M. A., Gold Nanoparticles: Interesting Optical Properties and Recent Applications in Cancer Diagnostic and Therapy. Nanomedicine 2007, 2, 681-693.

41.Pastoriza-Santos, I.; Perez-Juste, J.; Liz-Marzan, L. M. Silica-Coating and Hydrophobation of CTAB-Stabilized Gold Nanorods. Chemistry of Materials 2006, 18, 2465-2467.

Chapter 4 Semi-transparent organic and hybrid perovskite photovoltaic

In this chapter, we devote to develop new transparent electrode that is compatible to the organic solar cell and hybrid perovskite solar cell systems. We utilized the conventional dielectric/metal/dielectric sandwiched structure to achieve a high quality transparent electrode, and applied it to both organic and hybrid perovskite solar cells. We also demonstrate distributed bragg reflection structure to further improve the efficiency of the semitransparent solar cell without losing visible transparency.

4.1 Design of dielectric/metal/dielectric transparent electrode

Recent development of the transparent conductor technologies has enabled several model systems e.g. solution processed metal Nanowires (Ag or Cu); Conducting polymer and Graphene; Dielectric/Metal/Dielectric photonic structures and etc. Among all of these possibilities, most of them are through solution process or wet-transfer technique,[1-2] though they are proved to be successful on the organic solar cells, they are difficult to be implemented to the hybrid perovskite (PVSK) system, since the polar solvent used to disperse the transparent conductors usually dissolve the PVSK materials as perovskite is a polar semiconductor. Herein, we focus on the Dielectric/Metal/Dielectric (MoOx/Ag/MoOx) structure via simple thermal evaporation technique. Compared with the sputtered ITO, this technology is also more cost effective. The schematic of the PVSK photovoltaic device as well as the top electrode are illustrated in Fig.4.1.

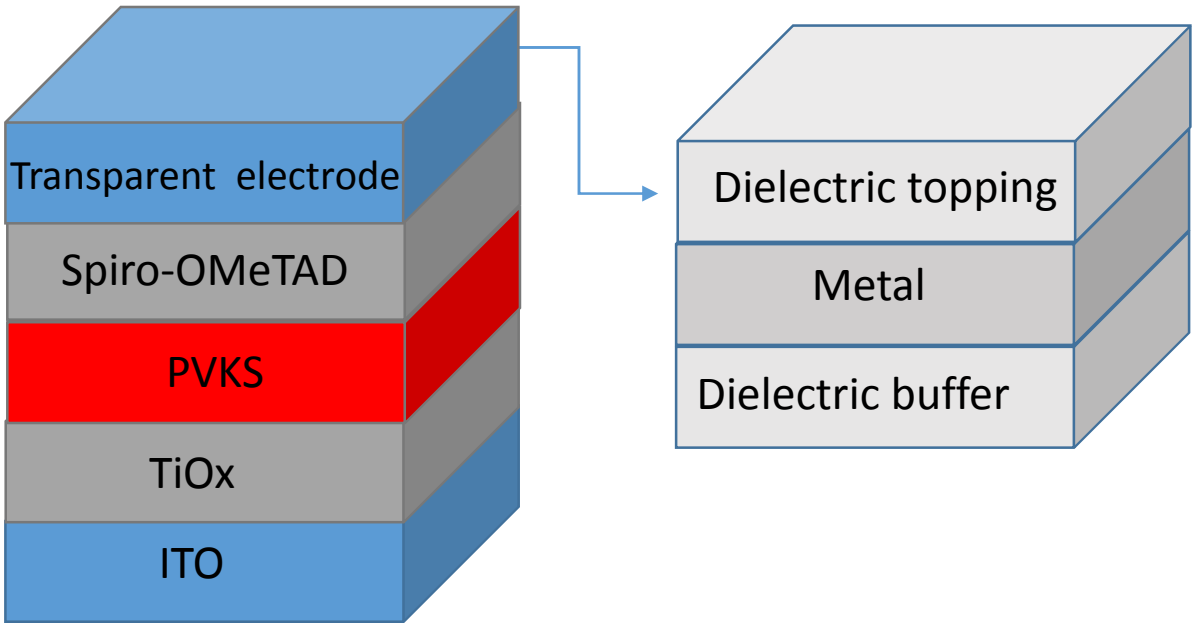

Figure 0-1 The schematic of the D/M/D transparent electrode.

The thermal evaporated MoOx is also a hole conducting material so as to be compatible with the Spiro-OMeTAD. This dielectric buffer layer provides a smooth surface for the metal deposition. The critical part of the transparent electrode is the metal layer, which determines the tradeoff between the transparency and the conductivity. Traditional Dielectric/Metal/Dielectric (DMD) structure use silver as the middle layer.[3-5] Silver thin film deposited on the dielectric material tends to form isolated nuclei for the first few nanometers. Therefore the thickness of silver must be over certain critical value, beyond which the isolated metal nuclei begin to connect together and form the continuous film, typically it is over 15 nm. During our research, we also noticed the quality of the transparent conductor is very much relying on some other deposit ion parameters than the mere thickness, i.e. fast evaporation rate (> 2nm/s) of the silver gives more continuous film morphology with higher conductivity, probably due to the inhabitation of the nucleation of the silver material, however such fast deposition rate can easily damage the

Spiro-OMeTAD and even the PVSK layer. Besides, the substrate temperature and roughness are also found to play an important role. All of these issues increase the complexity of this technology, and ultimately reduces the device performance, yield and reproducibility. The key is to control the wetting property of the silver layer sandwiched between two dielectrics and reduce the percolation threshold thickness. Here we find the wetting of the silver can be largely improved by inserting an ultral-thin Gold seed layer underneath the silver layer.

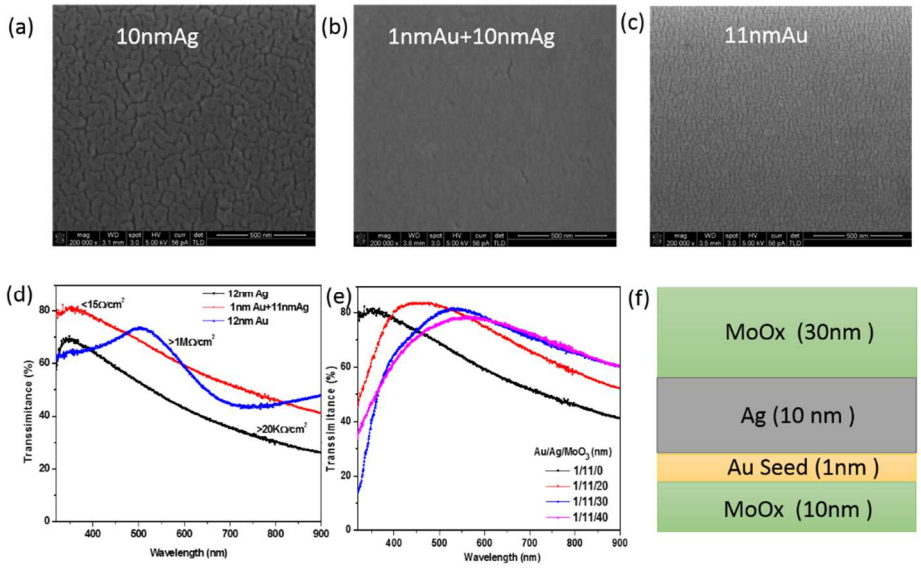

Figure 0-2 design of the Au seed layer incorporated D/MD transparent electrodes. The film morphology of (a) 10 nm pristine Ag, (b) 1nm Au seeded Ag film (11nm), and (c)pristine Au film (11nm). The transmittance of the pristine Ag, 1nm Au seeded Ag film, and pristine Au layer.(d) The transmittance of the 1nm Au seeded Ag film with different thickness of MoOx topping layer(e). The final parameters used in the study (f).

The film morphology of the silver layer dramatically changes by such strategy. As shown in the fig 4.2. a-c, the pristine silver layer is not continuous at 10nm with isolated metal inlands. However, it becomes much more uniform by inserting only 1 nm gold seed layer. The conductivity improves several orders of magnitude from 20KΩ/□ to around 16

Ω/□.The metal nuclei islands are very well connected to form charge conduction pathway. The transparency also increases as the plasmonic scattering effect are reduced with the smoother metal film. Interestingly, the pure gold thin film with same 10nm thickness also shows non-continuous morphology, the film is very resistive, it shows green color and has low transmittance at visible region due to the strong plasmonic scattering effect of the gold nano domains. The dielectric toping layer is used to further improve the transmittance of the electrode. All the dielectric materials in principle can deliver this function as long as they has large band gap toto avoid optical absorption, e.g.ZnS and ZnO.[7-8] Here, we still employ MoOx as the top layer just for easy process. The transmittance spectrum can be tuned by different MoOx thickness to match with the absorption spectra of active layer, as shown in fig 2.e. The final parameter of this top transparent electrode is illustrated in fig. 2. f. The transmittance is particularly high within the region from 550nm to 800nm, within which the PVSK materials actively absorb photons.

4.2 Top illuminated semitransparent hybrid perovskite solar cells

Up to the date the thesis is written, transparent top electrodes have been successfully applied in perovskite solar cells via limited approaches. A thin gold layer (~10 nm) is reported to be thermal evaporated, achieving a device with PCE of 7.5%. [9] In another report, a transparent conducting adhesive was utilized to laminate the Ni mesh embedded PET on the perovskite solar cell with a decent PCE over 13% from the ITO side and around 10% from the PET top electrode.[10] Recently, a transparent MoOx/ITO electrode on top of perovskite cells has been documented to obtain the efficiency of 6.2%.[11] The cell has been further used to build up the tandem device with the c-Si cell, achieving the final PCE of 13.4%. [11] The photovoltaic device employ the widely used planar structure with compact

TiO_2 as the electron transporting layer, and Spiro-OMeTAD as the hole conducting layer. The PVSK layer is deposited with two-step solution process.

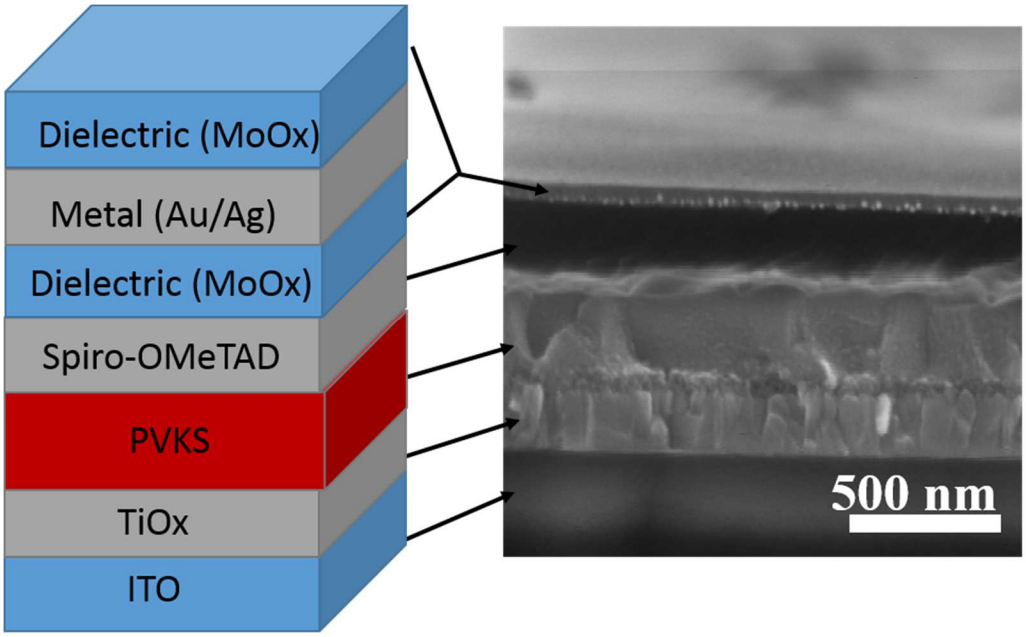

Figure 0-3 Device structure and cross-section of the top illuminated hybrid perovskite solar cell

The top illuminated semitransparent PVSK solar cell has an architecture as shown in Fig.4.3, and it delivers a very good device performance of 11% power conversion efficiency. The IV-Curve is shown in fig.4.4 . The fill factor (FF) achieves 75%, which is comparable with the best PVSK solar cell with regular metal electrode.[12-13] The open circuit voltage was as high as 1.005 V. This is also a reasonably high value, if considering that the photo-induced excess carrier concentration inside the semitransparent PVSK photovoltaic is lower than the regular device, so that the quasi Fermi level splitting is a little smaller. The high fill factor and open circuit voltage both indicate that the sheet resistance of this DMD transparent electrode is low enough to avoid the resistive loss. The short circuit current is lower than that in the regular opaque metal based device, due to the transmittance

loss of the top electrode. The short circuit current of the semitransparent PVSK solar cell is 14.65 A/cm^2, which is approximately 70% of the regular PVSK photovoltaic device. Such photocurrent loss correlates with the overall transmittance of the M/D/M transparent electrode.

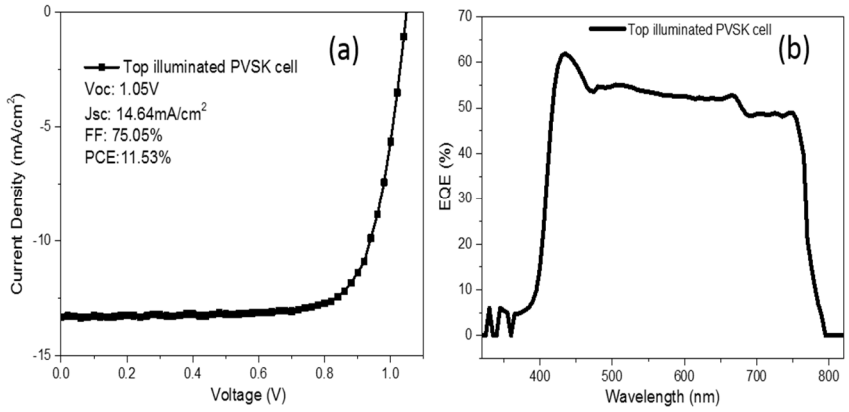

Figure 0-4 J-V characteristic (a) and external quantum efficiency of the top illuminated hybrid perovskite solar cells

4.3 Hybrid perovskite and CIGS four-tandem solar cells

Based on this M/D/M transparent top electrode, a four-terminal tandem solar cell with solution processed CIGS bottom cell is also demonstrated. The CIGS photovoltaic is via solution process following previous procedure,[14] and it shows Voc of 0.59V, Jsc of 29.75mA/cm2, FF of 70.7% and overall power conversion efficiency of 12.41%. . It is noted that the top cell and bottom cell should have approximately equal power conversion efficiency to maximize the benefit of the tandem device instead of the single junction device. Hence, solution processed CIGS bottom cell and PVSK top cell are believed to be a good combination for tandem structure. The CIGS bottom cell underneath the top cell show an efficiency of 3.97%, with Jsc of 10.2mA/cm2, Voc of 0.56V and FF of 69.6%.

The current-voltage curves and the external quantum efficiency (EQE) curves of the top PVSK cell, unfiltered CIGS solar cell, and CIGS bottom cell underneath the PVSK cell are shown in fig. 5.a and b. All the device parameters are included in table 4.1.

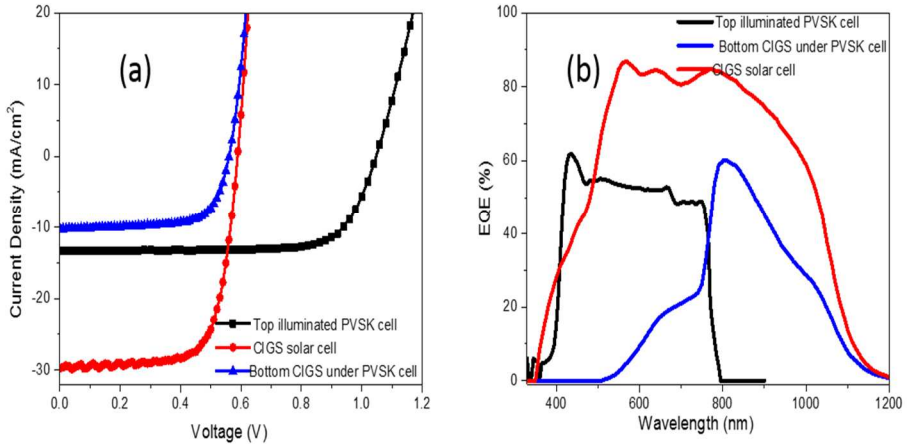

Figure 0-5 J-V characteristic (a) and external quantum efficiency(b) of the top illuminated hybrid perovskite solar cells, CIGS solar cells and Bottom CIGS cell under PVSK cell.

The four-terminal tandem device efficiency is realized by adding device efficiency of the top PVSK cell and the bottom CIGS cell when underneath the PVSK device. With the 11.53% efficient top illuminated PVSK cell, the efficiency of the solution processed CIGS solar cell was further upgraded to 15.5%, which was 25% enhancement. The easy solution process of both PVSK and CIGS active layer also ensure the low cost of this technology.

	Voc V	Jsc mA/cm²	FF %	PCE %
PVSK Top cell Illuminated from DMD electrode	1.05	14.64	75.05	11.53
CIGS solar cell	0.59	29.75	70.7	12.41
CIGS under PVSK cell	0.56	10.2	69.6	3.97
Four-terminal tandem				15.5%

Table 0-1 device parameters the top illuminated hybrid perovskite solar cells, CIGS solar cells and Bottom CIGS cell under PVSK cell.

It is worth mentioning that the underneath CIGS cell is without any antireflection coating, and the tandem device should be further improved when those photonic structure is introduced. The optical design parameter of such anti-reflection coating will be different with the single junction device, as only the photons with energy below the perovskite band gap need to be considered.

4.4 Visibly semitransparent organic photovoltaic

In addition to the pursuit of high efficiency solar cell, organic materials based photovoltaic have also been advocated for their potential in making unique applications e.g visibly transparent solar cells that could be used in building-integrated photovoltaics (BIPV) and integrated PV chargers for portable electronics. Herein, we also applied the D/M/D transparent electrode to the organic photovoltaic to fulfill the demands for the semitransparent organic solar cells.

From the point of view of the solar cell material, an ideal material for visibly transparent organic photovoltaic needs to be transmitted to the visible photons, but harvest as much as possible from ultraviolet (UV) and near infrared (NIR) wavelengths in the solar spectrum. There is often a compromise between absorbed photons and transparency which limits materials development for visibly transparent organic solar cells. For example, P3HT:PCBM and PTB7:PCBM bulk heterojunction blend are the most widely used photoactive layer material for this purpose.[15] However, such devices often have very low visible transparency due to their relatively high band gap. In this work, we use the newly developed high performance photovoltaic materials SPV1:$PC_{60}BM$ as the active layer.

The chemical structure and the absorption spectra are listed in Figure 4. 6.

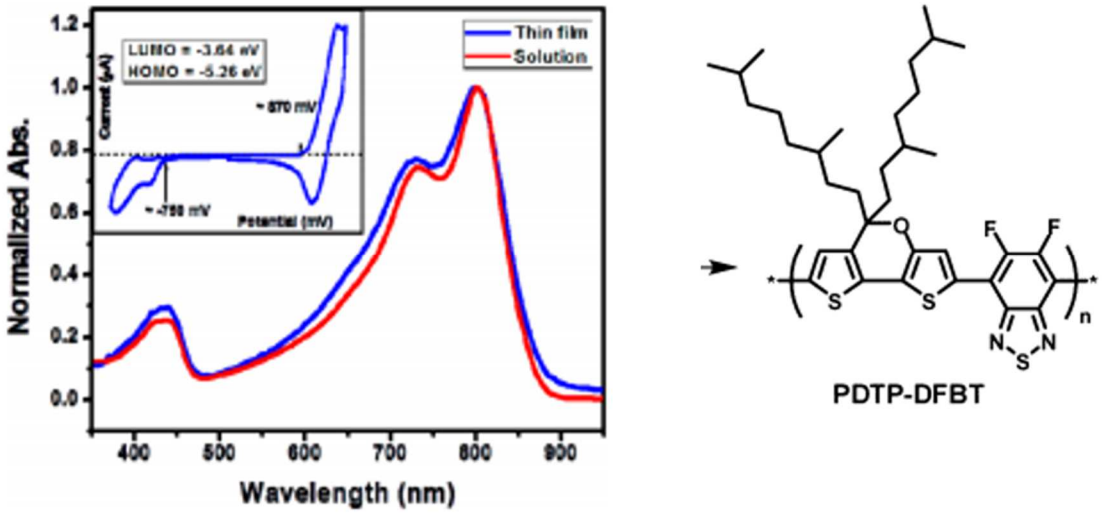

Figure 0-6 Chemical structure and absorption spectra of the low band gap polymer PDTP-DFBT

This bulk heterojunction blend exhibits extraordinary photovoltaic performance of ~ 6.5% efficiency. The SPV1: $PC_{70}BM$ shows even higher efficiency of ~8%.[16] Due to the intrinsic property of the polymeric semiconductor, the absorption of the polymer is always narrow, the absorption cross section is particularly high near the band edge, but is rather transparent to the higher energy photons. Such unique property enables this materials as an excellent candidate for the visibly transparent organic solar cell applications.

On the other hand, the transparent conductor is another key factor that ultimately determines the performance of visibly transparent organic solar cells. Based on the above discussion of the D/M/D transparent electrode, this might be a suitable candidate to achieve highly efficient and reproducible visibly semitransparent solar cell. Indeed, the following results show that the inverted solar cell with SPV1:$PC_{60}BM$ blend as the active layer, delivers an overall power conversion efficiency of 4.0% and the SPV1:$PC_{70}BM$ blend

system gives a higher efficiency of 5.5% but sacrificing little bit visible transparency since PC70BM has higher absorption cross section at the visible range. Smart photo management for visibly transparent organic solar cells

The best strategy to optimize the visibly transparent solar cell is try to increase the photo to electron conversion efficiency as much as possible at the UV and NIR region while keeping transparency at the visible region. Due to the limited carrier mobility, the organic active layer usually has relatively very thin thickness, i.e. ~ 100 nm, which is insufficient to absorb the NIR photons by single pass. To solve this problem, we developed the distributed bragg reflector on the back of the transparent electrode to selectively reflect the NIR photon and pass the visible photons. This concept is illustrated in the following figure 4.7.

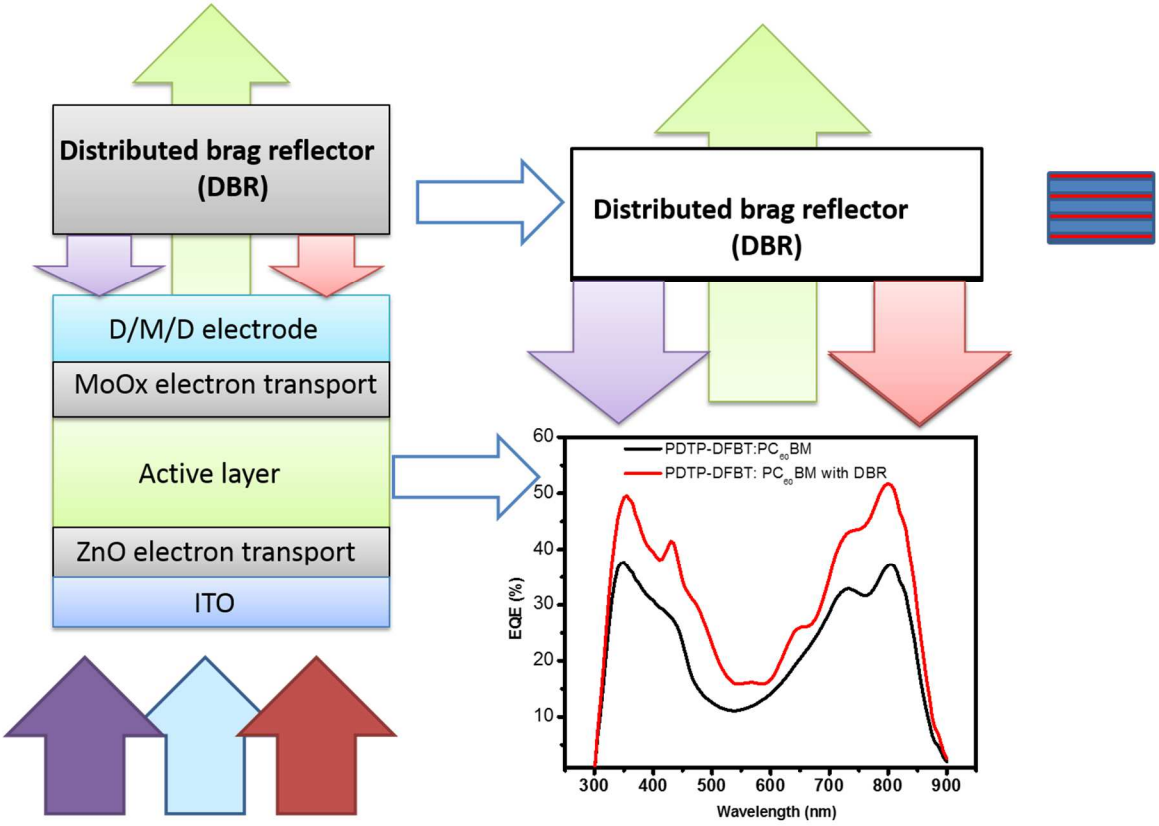

Figure 0-7 Schematic of the of the DBR incorporated visibly transparent solar cells

Such photonic structure can be realized simply by alternatively stacking different dielectric materials. In principle every pair of two dielectrics with sufficient refractive index difference can be employed to deliver this function. However, the band gap of this two materials have to be large enough to avoid absorption at the visible region. Herein, we alternatively evaporated LiF and TPD small molecule, with refractive index of 1.39 and 1.78 respectively, as the distributed bragg reflector (DBR). Figure 4. 7 illustrates the structure for this photonic DBR, and more alternating layers lead to better quality of the DBR. The reflection and transmittance region can be simply tuned by the thickness of each layer, to match with the absorption of different polymeric semiconductors. The thickness used in this study is 110 nm for TPD, and 150 nm for the LiF layer. It shows over 90 percent reflection at the NIR region (from 750 nm to 950 nm) as well as a secondary reflection mode at UV region (350-400), while the visible photons (from 400nm to 700nm) are almost completely transmitted as shown in the figure 4.8.

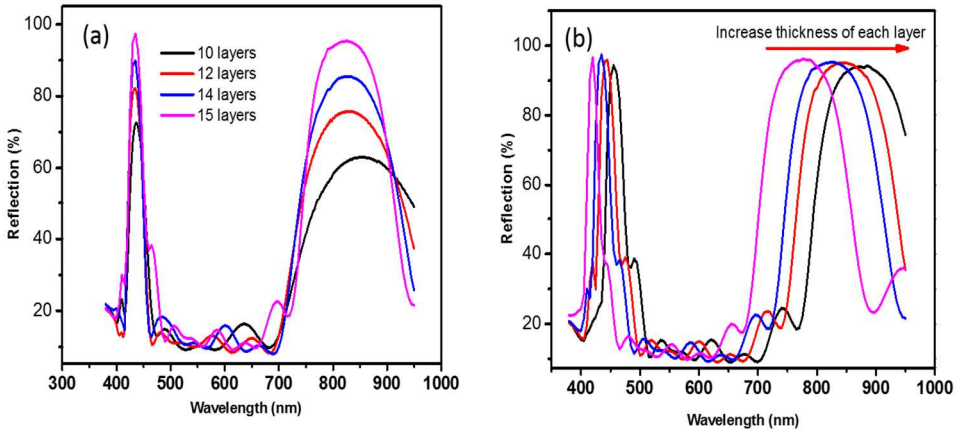

Figure 0-8 Design of the distributed bragg reflector (DBR) with different alternating layers and thickness of each layer.

By incorporating this DBR structure into the semitransparent organic solar cell, the active layer absorption in the NIR and UV region are both enhanced. The external quantum efficiency spectra clearly shows the quantum efficiency at these region are dramatically improved, which leads to an overall enhancement of the short circuit current and ultimately 25% improvement of the power conversion efficiency, as shown in figure 4.9.

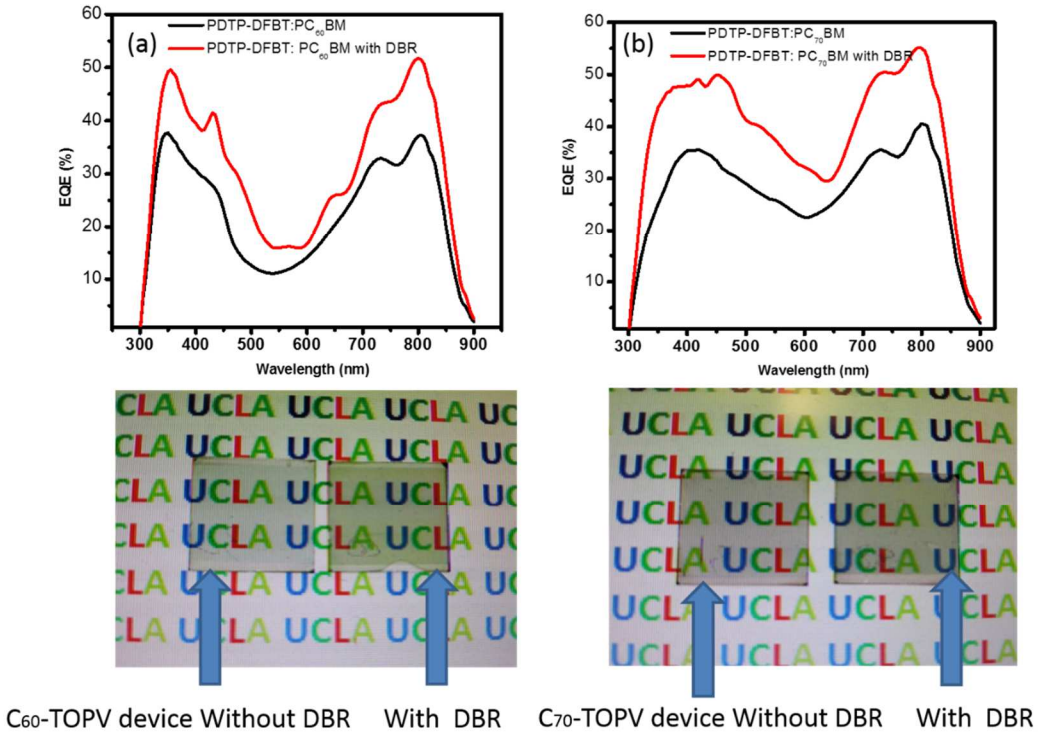

Figure 0-9 The EQE spectra of the DBR enhanced visibly transparent OPVs in the PDTP-DFBT:$PC_{61}BM$ and PDTP-DFBT:$PC_{71}BM$ systems.

While at the same time, whole solar cell device still looks rather transparent to the eyes, since the visible transmittance is not increased much, as shown in the transmittance spectra in below two figures in figure 4.9. In this work, we innovatively solve the

compromise between transparency and the efficiency, and pave a unique way to further improve the visibly transparent solar cell technology.

4.5 References

1. Chen, Chun-Chao, et al. "Visibly transparent polymer solar cells produced by solution processing." Acs Nano 6.8 (2012): 7185-7190.

2. Gaynor, W.; Lee, J. Y.; Peumans, P. Fully Solution-Processed Inverted Polymer Solar Cells with Laminated Nanowire Electrodes. ACS Nano 2010, 4, 30–34.

3. Lopéz, I. Pérez, et al. "Dielectric/metal/dielectric structures using copper as metal and MoO 3 as dielectric for use as transparent electrode." Thin Solid Films 520.20 (2012): 6419-6423.

4. Lewis, Jay, et al. "Highly flexible transparent electrodes for organic light-emitting diode-based displays." Applied physics letters 85.16 (2004): 3450-3452.

5. Sergeant, Nicholas P., et al. "Design of transparent anodes for resonant cavity enhanced light harvesting in organic solar cells." Advanced Materials 24.6 (2012): 728-732.

6. Jeong, Jin-A., and Han-Ki Kim. "Low resistance and highly transparent ITO–Ag–ITO multilayer electrode using surface plasmon resonance of Ag layer for bulk-heterojunction organic solar cells." Solar Energy Materials and Solar Cells93.10 (2009): 1801-1809.

7. Liu, Xuanjie, et al. "The design of ZnS/Ag/ZnS transparent conductive multilayer films." Thin Solid Films 441.1 (2003): 200-206.

8. Mohamed, S. H. "Effects of Ag layer and ZnO top layer thicknesses on the physical properties of ZnO/Ag/Zno multilayer system." Journal of Physics and Chemistry of Solids 69.10 (2008): 2378-2384.

9. Roldán-Carmona, Cristina, et al. "High efficiency single-junction semitransparent perovskite solar cells." Energy & Environmental Science 7.9 (2014): 2968-2973.

10. Bryant, Daniel, et al. "A Transparent Conductive Adhesive Laminate Electrode for High-Efficiency Organic-Inorganic Lead Halide Perovskite Solar Cells."Advanced Materials 26.44 (2014): 7499-7504.

11. Löper, Philipp, et al. "Organic–inorganic halide perovskite/crystalline silicon four-terminal tandem solar cells." Physical Chemistry Chemical Physics 17.3 (2015): 1619-1629.

12. Liu, Mingzhen, Michael B. Johnston, and Henry J. Snaith. "Efficient planar heterojunction perovskite solar cells by vapour deposition." Nature 501.7467 (2013): 395-398.

13. Liu, Dianyi, and Timothy L. Kelly. "Perovskite solar cells with a planar heterojunction structure prepared using room-temperature solution processing techniques." Nature Photonics 8.2 (2014): 133-138.

14. Zhou, Huanping, et al. "Interface engineering of highly efficient perovskite solar cells." Science 345.6196 (2014): 542-546.

15. Huang, Jinsong, Gang Li, and Yang Yang. "A Semi-transparent Plastic Solar Cell Fabricated by a Lamination Process." Advanced materials 20.3 (2008): 415-419.

16. Dou, Letian, et al. "Synthesis of 5 H-Dithieno [3, 2-b: 2′, 3′-d] pyran as an Electron-Rich Building Block for Donor–Acceptor Type Low-Bandgap Polymers." Macromolecules 46.9 (2013): 3384-3390.

Chapter 5 Photo-physical property of organic/inorganic hybrid perovskite materials and devices

Within the past two years, organic-inorganic perovskite (PVSK) solar cell has achieved unprecedentedly rapid progress of the solar cell efficiency. (1) (Martin Green review article) The efficiency has been improved to above 19% PCE, up from less than 10%. The perovskite materials (methylammonium plumbous trihalides) were employed as the absorber layer, representatives of a new class of semiconductor material that was first used in photovoltaic applications just four years ago. This rapid progress has promoted a research rush to investigate the fundamental physical and chemical properties of the PVSK materials.

5.1 Interplay between free carrier and exciton: crystal size matters

One of the central questions of the perovskite based semiconductor is what is the photoexcitation species, free carrier or exciton. These two different excited species will eventually leads to different optoelectronic applications. Excitonic material with tightly bound exciton give rise to fast recombination rate and high emission quantum yield and hence are potentially more suitable for light emitting diode or laser diode. While the free carrier based materials are more promising for photovoltaic cells, since electrons and holes need to be separately collected. Generally, the binding energy between electron and hole increases as the dimensionality is reduced due to the quantum confinement effect. When the radius of cation is larger than its limit for cubic packing, the perovskite transitions from 3D structure to 2D structure, which gives rise to the exciton binding. The most striking organic-inorganic hybrid perovskite material that recently achieve high photovoltaic

performance, adopts relatively small cation of $CH_3NH_3^+$ and has 3D structure. The exciton binding energy in this material is reported in the range of 19mV-50mV,[1] it is much smaller value than the normal organic semiconductors (a few hundreds meV). The photoexcitation specie in the commonly used tri-halide perovskite photovoltaic materials is believed to be free carrier or at least weakly bounded exciton. However, significant interplay between exciton and free carriers should exist given the 26meV of the characteristic thermal energy at room temperature. The experimental evidence is given by both steady state and transient absorption and photoluminescence measurement with temperature and excitation intensity dependence. The accurate estimation of the exciton binding energy is challenging. While this value is simply calculated in several literatures based on the temperature dependent PL measurement, assuming that the integrated PL intensity is decreased as temperature increases due to thermal dissociation of the exciton. Such assumption might not be valid without checking the PL dynamic, since non radiative recombination channel is more active at higher temperature, which ultimately reduces the PL intensity. So far, we believe the most reasonable estimation of the exciton binding energy is through the temperature dependent absorption measurement, through which ~50 meV exciton binding energy is estimated.[2]

However, we discovered that the photo-excitation species and exciton binding energy might be varied with different morphology or crystal size. The two typical samples with different crystal structures are in the figure 5.1.

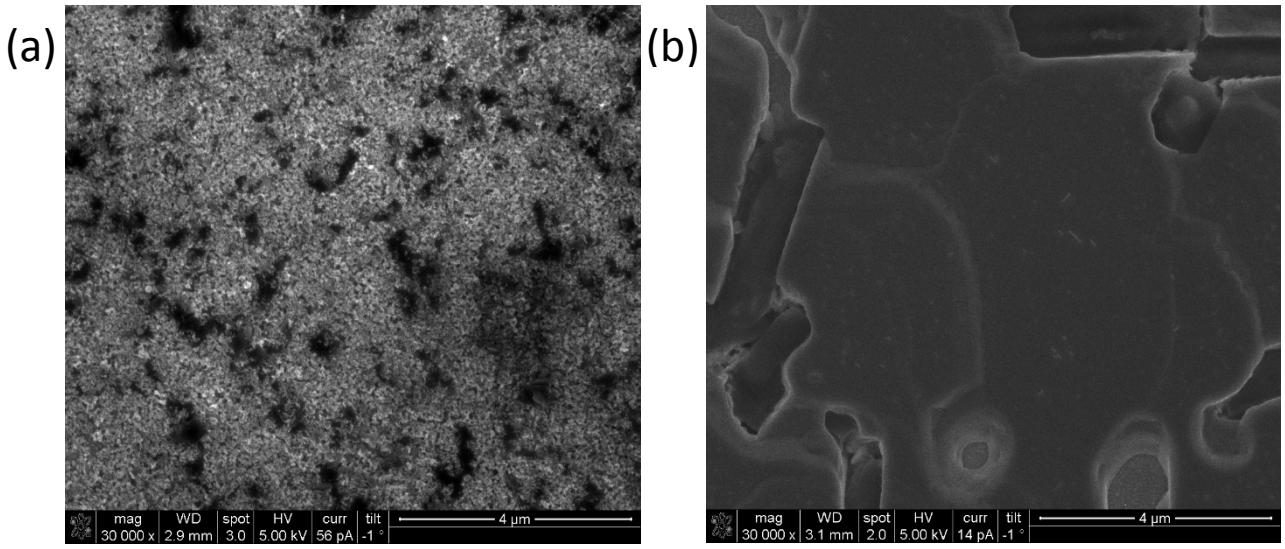

Figure 0-1 SEM image of the PVSK crystal on Al_2O_3 scaffold (a) and planar substrate (b), represent small and big PVSK crystal.

The absorption spectra is very different with the Meso-porous and planar perovskite. The "step like" excitonic absorption peak is observed in the big perovskite crystal sample and becomes very clear under low temperature. While the Meso-porous perovskite with small crystal exhibits distinct free carrier absorption character even at low temperature, as shown in figure 5.2.

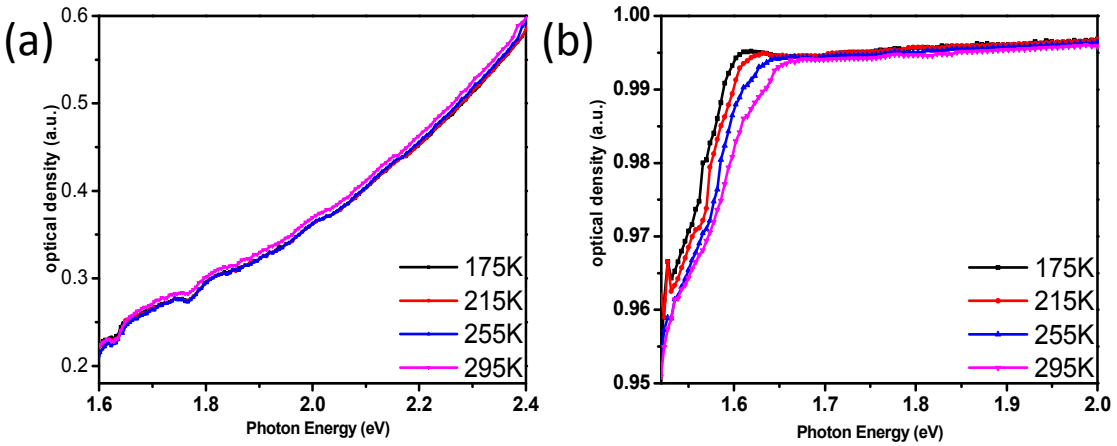

Figure 0-2 Temperature dependent absorption spectra of PVSK crystal on Al_2O_3 scaffold (a) and planar substrate (b).

The temperature dependent absorption spectra indicates that the photo excitation species are very different with different PVSK morphology. The photo excitations in small crystal PVSK are clearly dominated by free carrier, but the big crystal PVSK tends to form exciton upon photo excitation even though they are mostly likely weekly bounded ones.

To provide further evidences of the above argument, we performed the photoluminescence measurement as shown in Figure 5.3. Figure 5.3 (a) shows the PL spectra of the big crystal PVSK and the small PVSK crystal on the meso-porous Al_2O_3. The PL spectra of the PVSK crystal on the meso-porous AL_2O_3 is blue shifted to the higher energy level compared with big PVSK crystal. Exiciton has lower energy level than the free carrier, the energy gap in between is roughly the exciton binding energy. In addition, the big crystal PVSK gives much higher PL intensity, the exciton usually gives much higher emission quantum yield than the free carriers. Both observations are consistent with previous assumption that exciton is more preferred to be formed in big crystal PVSK than in the small size PVSK.

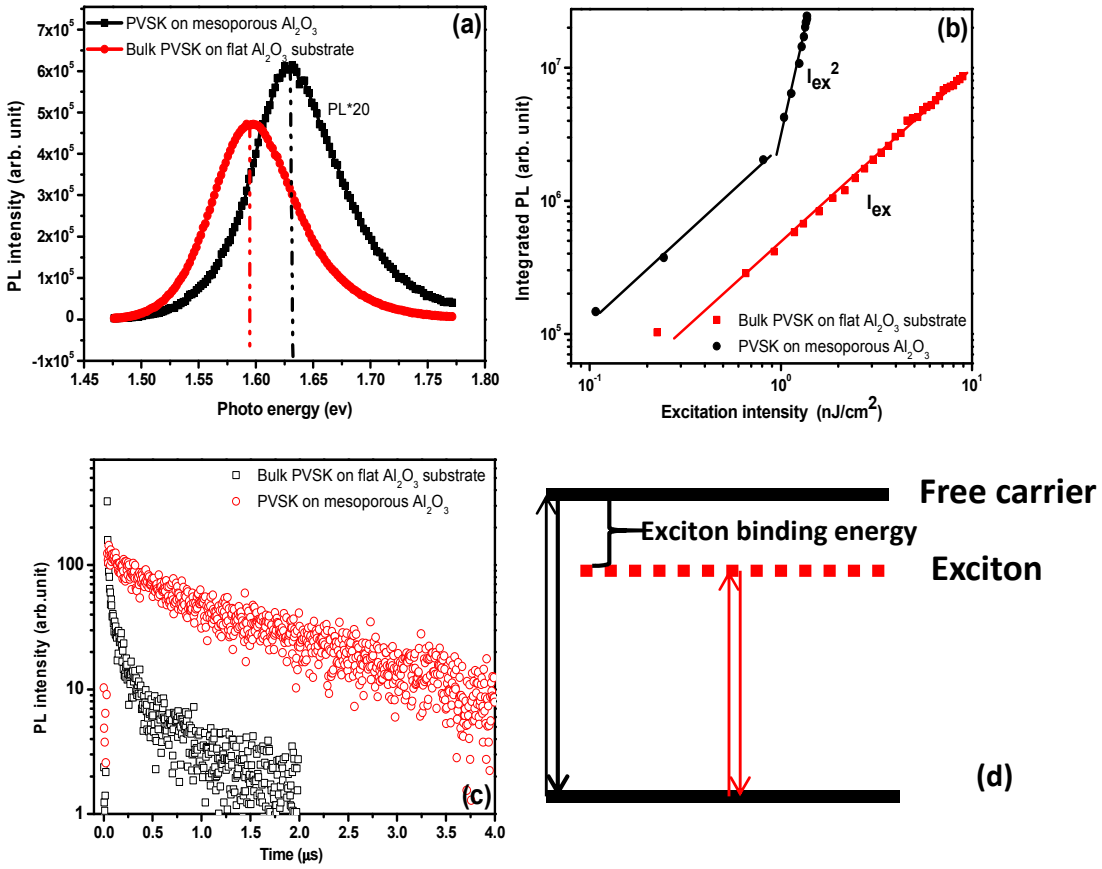

Figure 0-3 PL measurement of the big and small crystal PVSK film. The steady state measurement (a); and the excitation dependence PL measurement (b); the time-resolved PL measurement (c); the band position of free carrier and exciton in PVSK.

The time-resolved PL spectra tells that the charge carrier dynamic are very different in those two samples, the bulk PVSK on flat substrate shows much longer PL lifetime than the meso-porous small size PVSK sample as shown in Figure 5.3(C) . The excitation dependent PL spectra also reveals that the big PVSK crystal shows linear dependence of the excitation intensity, while the small size PVSK exhibits the Quadratic dependence on the excitation intensity. Such observation, once again, points out the free carriers are the dominating photo excitation spices in the small crystal size PVSK, while the electron-hole pairs are more likely to be dominant at the big crystal PVSK samples.

The photo physics of the perovskite semiconductor is still not fully understood yet. The research efforts on this topic will generate profound impacts on guiding future perovskite based optoelectronic device and provide insights to design new "magic" materials. Mance et.al observed the band filling in CH3NH3PbI3 and suggests that free charges accumulated at the band- edge can further reduce the exciton binding energy via columbic screening of photo-generated electron–hole pairs.[3] Although we are not sure about the reason why PVSK show free carrier signature or at least weekly bounded exciton, we speculate that this is originating from the strong molecular dipole in this polar semiconductor. One of the most intriguing parts of the organic inorganic hybrid perovskite semiconductor is the dipole moment induced by the cation, which distinguishes all the other traditional semiconductors. Most inorganic perovskites display spontaneous electric polarization and such phenomenon is particularly pronounced in hybrid halide perovskites.[4] A spontaneous polarization induced built-in electric field might acts to separate the exciton upon photo absorption.[5] This might be one of the physical origins of the low exciton binding energy in halide perovskite materials. The strong lattice polarization has potential advantages for enhanced charge separation and concomitant reduced recombination loss and improved carrier lifetimes.

5.2 Moisture effect on photo physics and photovoltaic device performance

In this study, we discovered a very unique and interesting phenomenon on perovskite. Moisture is assumed to be detrimental to organometal trihalide perovskite, as excess water can damage the crystallinity of the perovskite structure. Here, we report a growth mode for via thermal annealing of the perovskite precursor film in a humid environment (e.g., ambient air) to greatly improve the film quality, grain size, carrier mobility, and lifetime.

Our method produces devices with maximum power conversion efficiency of 17.1% and a fill factor of 80%, revealing a promising route to achieve high quality perovskite polycrystalline films with superior optoelectronic properties that can pave the way towards efficient photovoltaic conversion

The discovery was initially observed during PL measurement. We found the PL lifetime as well as the emission intensity were dramatically increased after exposure to the ambient air. By carefully control of the experimental condition, we finally excluded the possible effect of the Oxygen and concluded that it was the moisture in the air that leads to the improved PL lifetime and PL emission quantum yield. Generally, the improved the PL lifetime and quantum yield indicates an improved film quality with less defects density, which is more suitable for the solar cell devices. We further apply this knowledge to the solar cell device, and find it is a very effective method to improve the photovoltaic performance.

The steady-state photoluminescence (PL) measurement on the pristine, ambient air and moisturized nitrogen exposed perovskite films as shown in Fig. 3a. The perovskite film was spin-coated on PEDOT:PSS layer to emulate the processing in real condition of a p-i-n device. We found that PL intensity is greatly enhanced after treatments, which indicates that the non-radiative decay is significantly suppressed through moisture treatment. Furthermore, time-resolved PL (TRPL) (Fig. 5.4) clearly shows that the PL lifetime improves from ~24 ns for the pristine sample to ~40 ns after exposing in air for 60 minutes. Similarly, with the pristine perovskite film being held in a moisturized nitrogen environment for 10 minutes, the PL lifetime reaches ~50 ns. Dry oxygen exposure showed no photoluminescence intensity and life time change (Fig. 5.4). Here, the PL and the TRPL

measurements show that the non-radiative recombination channels are greatly blocked due to post moisture treatment, which is due to the defects reduction.

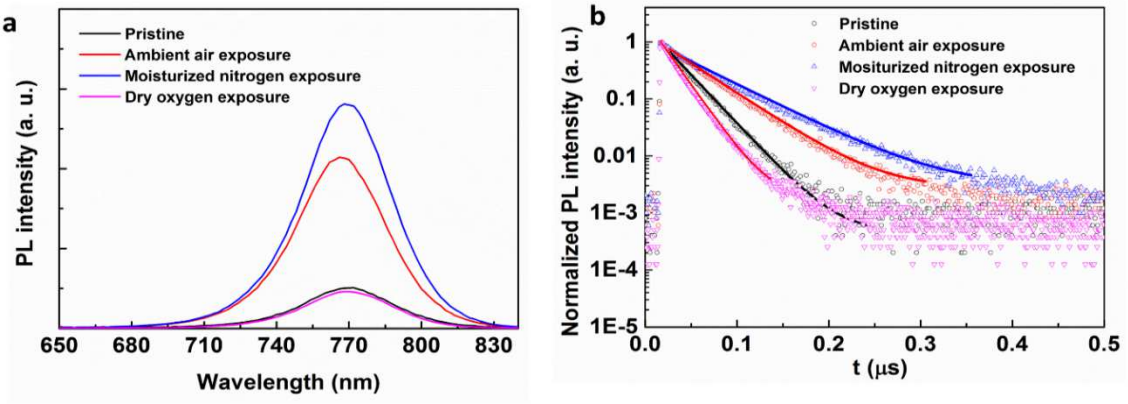

Figure 0-4 Moisture treated perovskite film with improved crystal quality confirmed by steady photoluminescence and transit photoluminescence. (a) Steady-state Photoluminescence (PL) measurement of pristine, ambient air exposed, moisturized nitrogen and dry oxygen exposed perovskite films on PEDOT:PSS layer. (b) Time-resolved PL (TRPL) measurement for the corresponding perovskite films. To investigate the effect of moisture treatment, we used SEM to observe the morphology evolution of a pristine film for different duration of moisture exposure.. SEM images of the film are shown in Figure 5-5 .

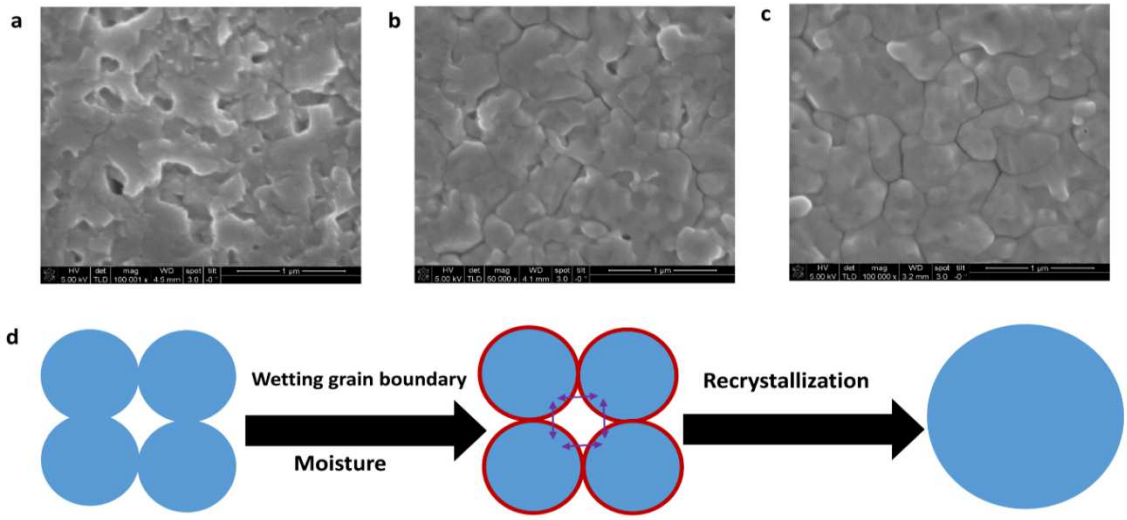

Figure 0-5 Morphology evolution with varying moisture treatment time and proposed mechanism. SEM images of the perovskite film with different moisture treatment time **(a)** 0min, **(b)** 30 min, (**c)** 60 min. (B) Liquid phase sintering as the mechanism for moisture treated perovskite growth.

Initially, the film exhibits sharp grain boundaries and pinholes. After the first 30 minutes moisture exposure, the apparent grain boundaries and pinholes are reduced. The crystal size further increased with an additional 30 minute of moisture treatment. Previous analysis shows that, the CH_3NH_3 group in perovskite $CH_3NH_3PbI_3$ system is strongly solvated by water.[6] During the moisture treatment, the wetted grain boundaries creep as a result of an increased grain boundary mobility. Hence, the grain ripening leads to an increased grain size and reduced pinholes. Such moisture-assisted crystal growth *via* recrystallization mechanism has been found in different crystal systems, ascribed to the grain boundary creep induced by moisture adsorption at grain boundary or surface.[7-8] Generally, moisture-assisted crystal growth, commonly referred to as "liquid phase sintering", involves three major steps, namely rearrangement of crystal domains, dissolution and precipitation of species on the grain boundary (so-called "contact flattening"), and final densification of the solid network. Liquid phase sintering requires a liquid soluble crystal phase, which is observed in the perovskite-water combination.[9] The proposed recrystallization process of $CH_3NH_3PbI_3$ under moisture treatment is shown in Figure 2d. The recrystallization process give rise to a high quality perovskite film, which is critical for optoelectronic devices fabrications.

The improved morphology of perovskite film (increased grain size and improved crystallinity) *via* post moisture treatment dramatically changes the film properties. We here applied this treatment method to the photovoltaic cells with device structure of glass/ITO/PEDOT:PSS/$CH_3NH_3PbI_{3-x}Cl_x$/PCBM/PFN/Al as shown in Fig 5.6.

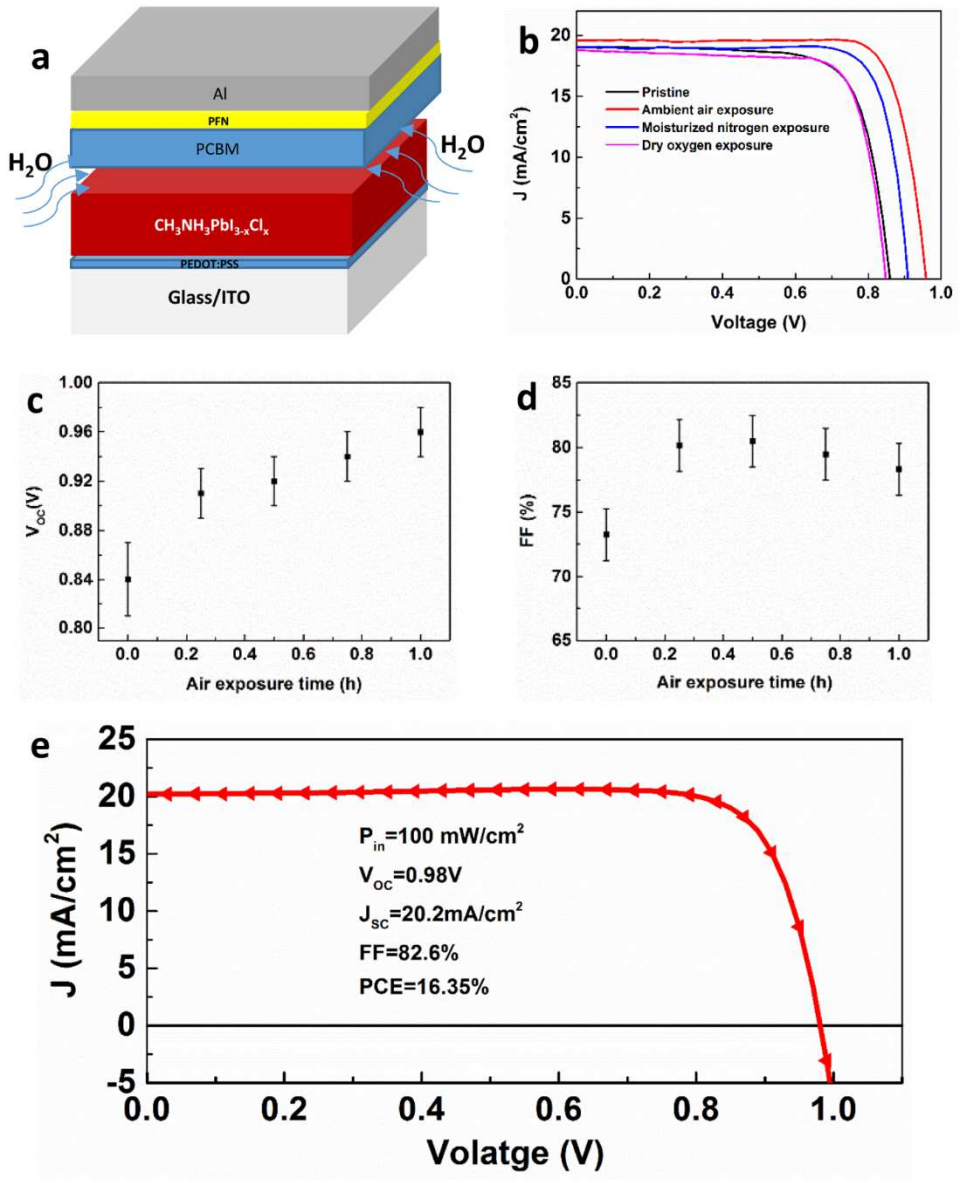

Figure 0-6 Device structure and device performance. (a) The device structure glass/ITO/PEDOT:PSS/$CH_3NH_3PbI_{3-x}Cl_x$/PCBM/PFN/Al. (b) J-V curve of the corresponding devices with the perovskite films treated under different environment, the measurements are carried out in simulated sunlight at 100 mW cm^{-2}. (c) The open circuit voltage (V_{OC}) evolution with air exposure time. (d) The fill factor (FF) evolution with the air exposure time. (e) J-V curve for a best-performance measured at 1 sun condition at 100 mW cm^{-2}.

The PEDOT:PSS and PCBM are the hole and electron transport layers, respectively. Besides, a layer of polyelectrolyte poly[(9,9-bis(3'-(*N* , *N* -dimethylamino) propyl)-2,7-

fluorene)-alt-2,7-(9,9-dioctylfluorene)] (PFN) interfacial layer helps to form an Ohmic contact for electron extraction from PCBM to Al [10], and improve device performance, especially in FF . Before coating PCBM, we exposed the annealed perovskite films into the moisture environment, including ambient air and moisturized nitrogen, and then transfer them back to in N_2 filled glove box for completing the cells fabrication including PCBM/PFN coating and electrode evaporation. The J-V characteristics of the devices based on perovskite films treated in different environment are shown in Fig.5-6 (b). We can see that after exposing the perovskite film to ambient air for one hour, the PCE is increased from 12.3% to 15.2%, especially on Voc from 0.86 V to 0.96 V and FF from 75% to 81%, while the short circuit current (J_{SC}) maintained at 19 mA/cm^2. The best performance of the ambient air post treated device shows 17.1 % PCE with 83% FF. The treatment in moisturized nitrogen also shows the similar enhancement, while the dry oxygen treated perovskite films exhibit a similar device performance as the pristine film. For the moisturized nitrogen environment, it is technically challenging to precisely control the moisture level, and thus a lower device performance is demonstrated in comparison with the ambient air post treatment. Again, the enhancement in device performance is consistent with the growth mechanism discussed in the previous section. Significant performance enhancement is also observed by annealing the as spin-coated perovskite precursor film in ambient air in comparison to moisture-free environment (N_2 or O_2) annealing, further confirming the role of moisture enhancement for device performance (Figure 5.6). The effect of post air exposure time on the V_{OC} and FF are provided in Fig. 5.6(c) and Fig. 5.6(d), respectively. The Voc gradually increases as the exposure time increases from 0.25h to 1h, and the average of Voc is increased to around 0.96 V, the

highest V_{OC} is 1.02V; and the FF increase from 74% to 81%. It should be noted that our results are highly reproducible, the post moisture devices always showed higher performance than that of the pristine devices, which is unambiguously ascribed to the moisture exposure. The photovoltaic device parameters are included in the following table:

Devices	Voc (V)	Jsc (mA/cm^2)	FF (%)	PCE (%)
Pristine	0.86	19.0	75	12.3
Ambient Air exposure	0.96	19.5	81	15.2
	(0.98)	(20.2)	(82.6)	(16.4)
Moisturized nitrogen exposure	0.92	19.1	80	14.1
Dry oxygen exposure	0.85	18.8	76	12.2

Table 0-1 Devices performance based on pristine and post treated perovskite films.

In conclusion, we have found that moisture treatment triggers desirable grain growth mode of the perovskite films in the precursor films *via* a well-controlled moisture exposure, which greatly enhances the bulk and surface properties. The improved film quality leads to improved power conversion efficiency. The moisture induced perovskite grain growth method is not limited to solar cell application but applicable to other electronic devices, such as transistors and sensors. According to recently published results, there is a large discrepancy in reported device efficiency, even though similar processing parameters are adopted. Our finding reveals that moisture is one of the hidden daemons, and thus the method we proposed shall dramatically promote the development of this rapidly-growing field. Although high Voc of ~1 V is the common value from the champion devices reported so far, all these devices are unintentionally processed in ambient air, according to our finding, the moisture effects are inevitably a parameter that requires

strictly control in order to have highly reproducible data, and more importantly, consistent device performances with respect to future application.

5.3 Experimental details

Materials and Characterizations. $PbCl_2$ was purchased from Alfa Aesar. The CH_3NH_3I was synthesized using the approach outlined in the reference 37. The PEODT:PSS and PCBM was purchased from Clevious and Nano-C, respectively. The XRD patterns were collected on a PANalytical X'Pert Pro X-ray powder diffractometer using Cu-Kα radiation (λ=1.54050A). The scanning electron microscope (SEM) images were taken on a Jeooel JSM-6700F. Steady-state photoluminescence (PL) was measured by Horiba Jobinyvon system with an excitation at 600 nm. In the time resolved photoluminescence (TRPL) measurement, the samples were excited by a pulsed laser (PDL 800-B system with an extended trigger), the pulsed laser wavelength and frequency are 632 nm and 1MHz, respectively. The PL photons were counted by Picoharp 300 after pre-amplified by PAM 102.

Device fabrication and measurement. PEDOT:PSS was spin-casted on ITO surface under 4000 rpm, and then annealed at 120 ^{O}C for 15 min in ambient air. The PEDOT:PSS coated substrates were transferred into nitrogen glove box (O_2 and H_2O level lower than 5 ppm [19, 24]) for perovskite coating and annealing. For the perovskite layer, 1:3 ratio of $PbCl_2$:CH_3NH_3I was mixed in *N*, *N*-Dimethylformamide (DMF) solvent. Specifically, the concentration of the $PbCl_2$ and CH_3NH_3I were 0.8M and 2.4M, respectively. The mixture solution was spin coated onto the PEDOT:PSS layer at 1500 rpm, and a thin transparent yellow film (precursor film) forms on the substrates. After annealing at 90^{O}C for 2h in

nitrogen glove box, the film color changed from yellow to brown dark, indicating that the perovskite phase has been formed, and this film was named as pristine perovskite film. After annealing, the pristine perovskite films were post-treated in different environment including ambient air, nitrogen with high level of moisture (moisturized nitrogen) and dry oxygen box, respectively. Before treatment, the annealed samples are cooled to room temperature (~25 ^{o}C). For post ambient air exposure, the annealed (pristine) perovskite films were taken out from nitrogen glove box and left in ambient air (25^{o}C, 35% humidity) for 1h. To study the effect of moisture level on the device performance, the humidity is controlled in a small home-made chamber. The inlet of the chamber supplies water vapor, and the outlet extracts the vapor by a mechanical pump. As the humidity of the chamber stabilized, the annealed samples are placed into the chamber for 1h moisture exposure. The temperature remains at room temperature (20-25 ^{o}C), and a humidity thermometer monitored the humidity and temperature in the chamber. For oxygen exposure, the annealed perovskite film was quickly moved from N_2 glove box into a dry oxygen chamber. To further confirm the role of moisture, the annealed sample was also placed in a moisturized nitrogen environment where perovskite film is placed in a petri-dish with a paper soaked with 1mL of water for 10 minutes. After finishing treatment for perovskite films, the perovskite films were transferred into nitrogen glove box. 2% PCBM in chlorobenzene solution was coated onto the perovskite layer at 1000 rpm. After that, 0.02% PFN in methanol was spin-coated on PCBM at 2000 rpm for 30s. Finally, the device was transferred to vacuum chamber for Al electrode evaporation. The devices area is 0.1 cm^2. *J–V* characteristics of photovoltaic cells were taken using a Keithley 2400 source measure unit under a simulated AM1.5G spectrum. The measurement was performed under the

specific condition (1.2 V→0 V, step, 0.02 V, delay time 20 ms). The accuracy of measurement is considered in supporting information and Figure S14. With an Oriel 9600 solar simulator, the light intensity was calibrated by KG-5 Si diode. The I-V measurements were carried out in nitrogen glove box. UV epoxy (product number OG116, Epoxy Technology) was used to encapsulate the devices. Specifically, three drops of UV epoxy were put onto the devices surface for cover glass adhesion. Then, the UV epoxy was cured by UV lamp for 10 min. The encapsulated devices were taken out for EQE measurement, External quantum efficiencies were measured by Enli tech (Taiwan) EQE measurement system.

5.4 References

1. Sum, Tze Chien, and Nripan Mathews. "Advancements in perovskite solar cells: photophysics behind the photovoltaics." Energy & Environmental Science 7.8 (2014): 2518-2534.
2. D'Innocenzo, Valerio, et al. "Excitons versus free charges in organo-lead tri-halide perovskites." Nature communications 5 (2014).
3. Frontera, Carlos, et al. "Effect of band filling and structural distortions on the Curie temperature of Fe-Mo double perovskites." Physical Review B 68.1 (2003): 012412.
4. Kutes, Yasemin, et al. "Direct observation of ferroelectric domains in solution-processed CH3NH3PbI3 Perovskite Thin Films." The Journal of Physical Chemistry Letters 5.19 (2014): 3335-3339.

5. Liu, Shi, et al. "Ferroelectric Domain Wall Induced Band-Gap Reduction and Charge Separation in Organometal Halide Perovskites." The Journal of Physical Chemistry Letters (2015).
6. Xiao, Manda, et al. "A fast deposition-crystallization procedure for highly efficient lead iodide perovskite thin-film solar cells." Angewandte Chemie126.37 (2014): 10056-10061.
7. Xiao, Zhengguo, et al. "Solvent Annealing of Perovskite-Induced Crystal Growth for Photovoltaic-Device Efficiency Enhancement." Advanced Materials26.37 (2014): 6503-6509.
8. Jeon, Nam Joong, et al. "Solvent engineering for high-performance inorganic–organic hybrid perovskite solar cells." Nature materials (2014).\
9. Urai, Janos L. "Water assisted dynamic recrystallization and weakening in polycrystalline bischofite." Tectonophysics 96.1 (1983): 125-157.
10. Urai, Janos L., et al. "Weakening of rock salt by water during long-term creep." (1986): 554-557.

Chapter 6 Solution-processed hybrid perovskite photodetectors with high detectivity

Photodetectors capture optical signals with a wide range of incident photon flux density and convert them to electrical signals instantaneously. They have many important applications including imaging, optical communication, remote control, chemical/biological sensing and so on. Currently, GaN, Si and InGaAs photodetectors are used in commercially available products. Here we demonstrate a novel solution-processed photodetector based on an organic–inorganic hybrid perovskite material. Operating at room temperature, the photodetectors exhibit a large detectivity (the ability to detect weak signals) approaching 1014 Jones, a linear dynamic range over 100 decibels (dB) and a fast photoresponse with 3-dB bandwidth up to 3 MHz. The performance is significantly better than most of the organic, quantum dot and hybrid photodetectors reported so far; and is comparable, or even better than, the traditional inorganic semiconductor-based photodetectors. Our results indicate that with proper device interface design, perovskite materials are promising candidates for low-cost, high-performance photodetectors.

6.1 Objective and experimental design

Photodetectors that capture light signals and convert them to electric signals are very important functional components in many applications[1-3]. A semiconductor material is essential to absorb the incident photons and create electron and hole pairs upon photo-excitation. And a built-in or applied electric field is necessary to separate the electrons and holes to produce an electric current. Various types of semi-conductor materials have been applied in photodetectors, such as Si, InGaAs, ZnO, GaN, carbon nanotubes, quantum dots,

and conjugated polymers[1-10]. Though certain applications require different features, the key figure-of-merit parameters are responsivity (R), detectivity (D^*), noise equivalent power (NEP), linear dynamic range (LDR), and response speed. As briefly introduced later, we evaluate the photodetector performance based on these parameters.

Recently, a group of organic/inorganic hybrid perovskite materials were reported, with rapid progress in photovoltaic cells[11-15]. Various device architectures have been demonstrated with respectable efficiencies of ~15% from simple solution processes[16-18]. More importantly, the long charge carrier lifetime and diffusion length have been observed from perovskite films showing low recombination of charge carriers in the bulk films. This strongly suggests a huge potential of this class of materials for solar cell and photodetector applications[19-22]. We observed perovskite materials with very high EQE in the spectral range from 300 nm to 800 nm, which is desirable for photodetector purposes. Also it has been proposed that these types of materials have a very low density of defects and traps within the bandgap[23]. It suggests that the saturation current (J_o) of the perovskite-based diodes can be very low. The absorption coefficient (ε) of the hybrid perovskite reaches the order of 10^4 cm^{-1}, which can be ascribed to the direct bandgap nature of the electronic transition. Therefore, a very thin (few hundred nanometers) layer of the material is sufficient for almost complete light absorption. With such a thin film, the travel distance for photogenerated charge carriers is small, and thus the photoresponse should be fast. These characteristics strongly indicate that the hybrid perovskite materials are ideal candidates for photodetector applications.

Given the above-mentioned advantages of the materials properties, we demonstrate a novel solution-processed hybrid perovskite photodetector. By utilizing a water/alcohol

soluble conjugated polymer as the hole-blocking layer, we reduced the dark current density and achieved a very high detectivity for the hybrid perovskite photodetectors. In addition, our devices work at low (or even zero) bias, and show large dynamic linear response range, fast response speed, as well as low noise currents. The parameters are compatible or even better than those of the commercial Si photodetectors. Our results indicate that the hybrid perovskite material is a promising candidate for low-cost and high performance photodetectors.

6.2 Device characterization and results

The device structure of our photodetector is shown in Fig. 5. 1a and the energy diagram of the device is shown in Fig. 5.1b. On top of indium-tin-oxide (ITO) coated glass, an organic-inorganic hybrid $CH_3NH_3PbI_{3-x}Cl_x$ layer was sandwiched between PEDOT:PSS (hole transporting material, p-type layer) and PCBM (electron transporting material, n-type layer). Solar cells based on similar configuration have been demonstrated with fairly good performance in previous reports[24]. To reduce the charge recombination as well as the dark current density under reverse bias (particularly important for photodetectors), 2,9-Dimethyl-4,7-diphenyl-1,10-phenanthroline (BCP) and poly [(9,9-bis(3'-(N,N-dimethylamino)propyl)-2,7-fluorene)-alt-2,7-(9,9-dioctylfluorene)] (PFN) were used as the contact buffer materials. Aluminum was used as the top electrode. Three types of devices were fabricated: PD1 without buffers and PD2 and PD3, with BCP and PFN as cathode buffer layers, respectively. Fig. 1c shows the absorption spectrum of the photodetector (buffer layer and Al electrode are not included). The absorption onsite is at 780 nm and the device has a strong absorption from the near-IR to UV region, which mainly

comes from $CH_3NH_3PbI_{3-x}Cl_x$ (absorption coefficient over 10^4 cm^{-1}). The thickness of the active layer was varied from 200 to 600 nm and it was found that a thickness over 300 nm is enough to absorb most of the photons.

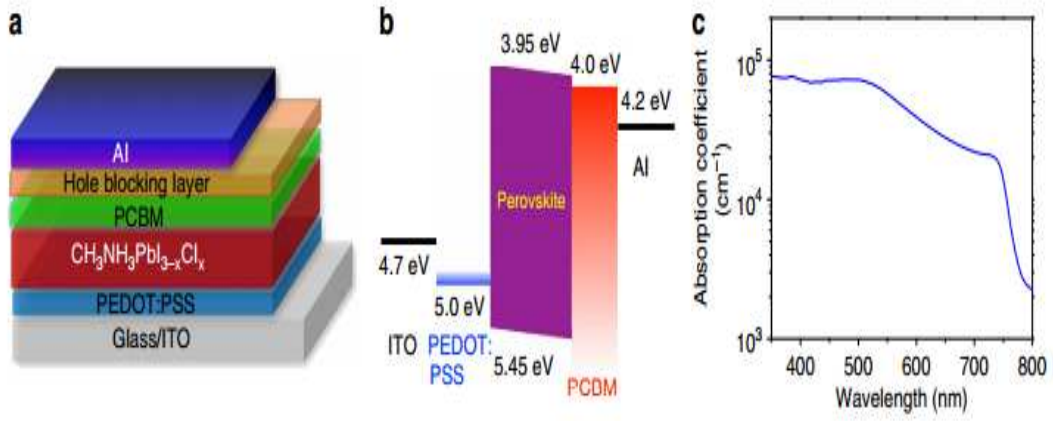

Figure 0-1 Hybrid pervoskite photodetectors. a, Device structure of the hybrid pervoskite photodetector. b, Energy diagram of the pervoskite photodetector under a slight reverse bias. c, UV-visible absorption spectra of the photodetector without the hole blocking layer and the Al electrode.

Detectivity characterization. Responsivity, the ratio of photocurrent to incident-light intensity, indicates how efficiently the detector responds to an optical signal. It is expressed as

$$R = \frac{J_{ph}}{L_{light}} \quad (1)$$

where J_{ph} is the photocurrent and L_{light} is the incident light intensity. Since R is proportional to the quantum yield of the photodetector, it is very important for a photodetector to have a high conversion rate from photons to electrons/holes, or high external quantum efficiency (EQE).

Detectivity is given by

$$D^* = \frac{(Af)^{1/2}}{(R/i_n)} \quad (2)$$

where A is the effective area of the detector, f is the electrical bandwidth, and i_n is the noise current. When the dark current is dominated by the shot noise, D^* can be expressed as

$$D^* = \frac{J_{ph}/L_{light}}{(2qJ_d)^{1/2}} \quad (3)$$

where J_d is the dark current and q is the elementary charge. Evidently the dark current of the diode should be depressed as low as possible to distinguish from very weak optical signals. In order to obtain a small J_d, the semiconductor film should have low trap density, low thermal emission (recombination) rates, and good film quality to avoid any leakage current during operation.

To characterize the photodetector, we used a light emitting diode working in continuous mode as a monochromatic light source. Fig. 6.2a shows the current density-voltage (*J–V*) characteristics measured in the dark and under illumination with λ = 550 nm (power density = 1 mW cm^{-2}). All devices show similar photocurrent densities under light (see Supplementary Figure 6. 2 for the *J–V* curves). Because the photocurrents remain almost constant at different reverse bias (0 to -2 V), a very small (or even zero) voltage can be applied to extract the electrons and holes generated in the detector. The dark *J–V* characteristics, however, vary dramatically. For PD1, a rectification ratio of ~10^2 (±1 V) and a dark current density of 1×10^{-7} A cm^{-2} (at - 100 mV) were obtained. The specific detectivity at 550 nm was then calculated to be 3×10^{11} Jones (Jones = $cmHz^{1/2}$ W^{-1}). The large J_d indicates significant injection under reverse bias. One possible reason is that the contact between the PCBM layer and the Al cathode causes holes injection into the diode.

To verify if hole injection occurs in PD1, a layer of BCP, which is famous for its hole blocking properties due to its deep HOMO level of -6.7 eV[25], was deposited on PCBM. As expected, PD2 shows a smaller J_d and a higher detectivity of 2×10^{12} Jones at -100 mV. Interestingly, when PFN was used, PD3 shows a significantly reduced J_d, a good rectification ratio of $\sim10^5$ (±1 V), and a very high detectivity of 8×10^{13} Jones at -100 mV. Note, the hybrid perovskite photodetectors can also be self-powered and work at 0 bias. If calculated at 0 mV, the detectivity is as high as 4×10^{14} Jones (J_d at 0 mV is lower and getting close to the noise current). PFN has been widely used in organic light emitting diode (OLED) and organic photovoltaic (OPV) devices because it builds up the surface dipole to lower the work function of metal cathode, and improves the electron injection and extraction in those devices[26], respectively. Here, it is found that PFN serves as an excellent hole blocking material for photodetectors. The mechanism is believed to be similar to the OLED and OPV devices. A dipole layer is formed at the PCBM and Al interface, which provides an extra electric field to prevent the hole-injection while enhancing electron-injection. This explains the dramatic increase in forward bias injection of PD3 in comparison with PD1 and PD2 as shown in Fig. 6.2a. The *EQE* and detectivity of the photodetector (PD3) at different wavelengths is shown in Fig. 6.2b. The device has a photo-response from 300 to 800 nm and a peak *EQE* of 80%. From 350 to 750 nm, the detectivity approaches 10^{14} Jones (at -100 mV), which is about one order of magnitude higher than the detectivity of a Si photodetector in the same spectral region (the detectivity of a Si photodetector is shown in Fig. 6.2b for comparison)[9].

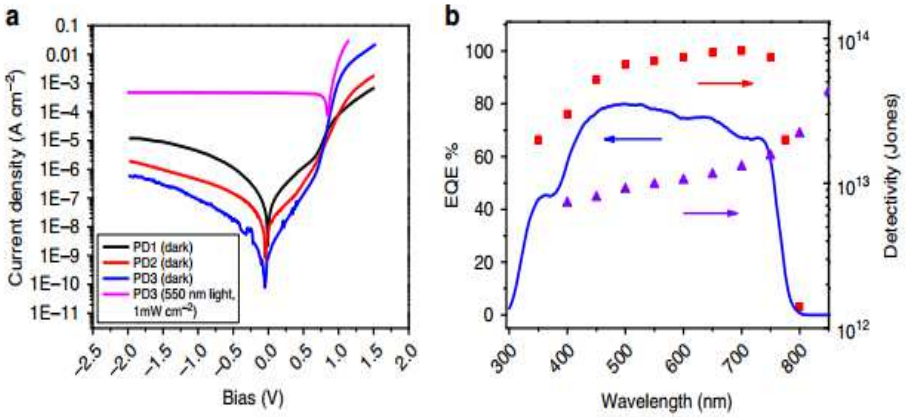

Figure 0-2 Performance of Hybrid pervoskite photodetectors. a, Current density-Votage curves of photodetectors with and without the hole blocking layer. PD1, without hole blocking layers; PD2, with BCP as the hole blocking layer; and PD3, with PFN as the hole blocking layer. b, External quantum efficiency and detectivity of the hybrid pervoskite photodetector at different wavelength. The detectivity of a single crystalline silicon diode (purple triangle) is shown for comparison.

The high detectivity of perovskite photodetectors is mainly due to its extremely low dark current under reverse bias. Interface engineering ensures a good blocking layer to avoid the leakage current, but the dark current is ultimately limited by the recombination current, which is an intrinsic property of the semiconductor material and the heterojuction diode. To further understand this issue, we fit the dark *J–V* curve to extract the dark saturation current density, J_0, a parameter that is directly related to the band-to-band thermal emission and recombination rate in semiconductors. As shown in Fig.6.3, our perovskite detector (PD3) has a very low J_0 of 1.5×10^{-11} mA cm^{-2} (see Methods for detailed calculations), which is much lower than some of the conventional solution-processed semiconductor diodes such as CdTe (8×10^{-11} mA cm^{-2}) and GIGS (6×10^{-7} mA cm^{-2})[27]. Such a small J_0 explains the origin of its high photo-detectivity and also illuminates the reason why very small bandgap-to-V_{OC} losses (~ 0.4 eV) can be achieved with perovskite-based photovoltaics[28].

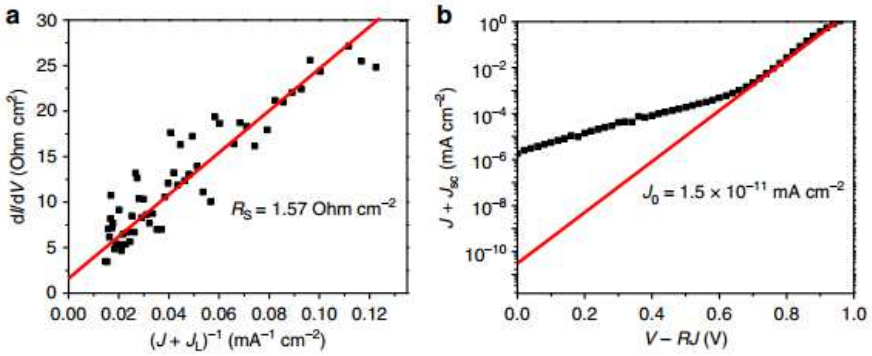

Figure 0-3 Current-Voltage characteristic the photodetectors (PD3). The device structure is ITO/PEDOT:PSS/CH3NH3PbI3-xClx/PCBM/PFN/Al. The original J–V curve is shown in Fig. 6.1c. a, Plot of –dV/dJ vs (J+JL)-1 and linear fitting. b, ln(J+JSC) vs (V-RJ) and linear fitting. Both of fittings are located around corresponding VOC. The J_0 is calculated to be 1.5×10-11 mA cm^{-2}.

Another figure-of-merit for photodetectors is the *LDR*, or photo-sensitivity linearity (typically quoted in dB). Linear dynamic range is given by

$$LDR = 20\log\left(J^*_{ph}/J_d\right) \quad (4)$$

where J^*_{ph} is the photocurrent, measured at a light intensity of 1 mW cm^{-2}. It indicates that within a certain range, the photocurrent has a linear response as the incident light intensity changes. This is important because beyond this range, the intensity of the light signal cannot be detected and calculated precisely.

Fig. 6.4 shows photocurrent versus light intensity for PD3. When illuminated under light, the device shows a linear response within the incident photon flux density range from 10^{17} to 10^{10} number $s^{-1}cm^{-2}$ (or power density range from 1×10^{-1} W cm^{-2} to 1×10^{-8} W cm^{-2}) and a linear dynamic range of over 100 dB. These results are comparable with Si photodetectors (120 dB) and higher than other types of photodetectors such as InGaAs (66 dB). The quantum efficiency remains almost constant at different incident power density (Fig. 4, y-

axis on the right). Thus, we confirm that the hybrid perovskite photodetector is well suited to detect a wide range of incident powers.

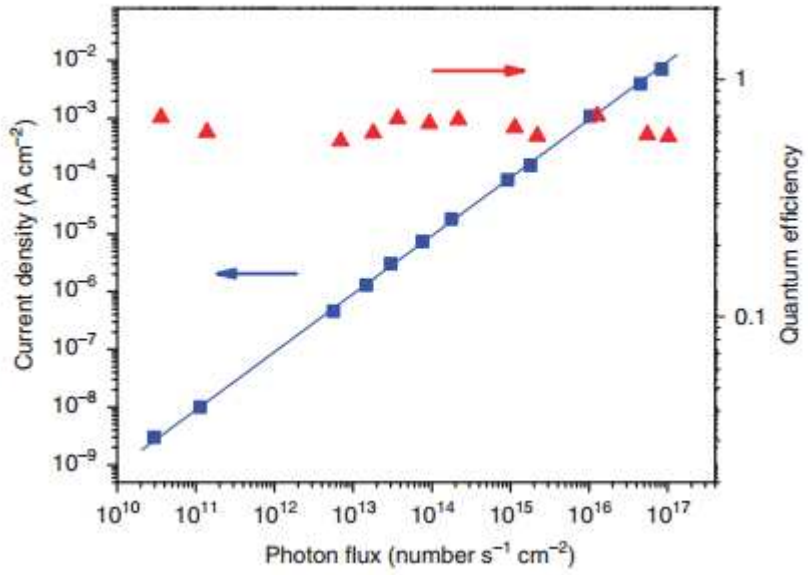

Figure 0-4 Linear dynamic range of the photodetectors (PD3). The device strucuture is ITO/PEDOT:PSS/$CH_3NH_3PbI_{3-x}Cl_x$/PCBM/PFN/Al. The photodetector has a large linear dynamic range of more than 100 dB.

The response speed of a photodetector is strongly related to charge transport and collection. Some devices need optical signals to be collected to enable operation with a certain bandwidth (for example, high frequency optical communication), which requires fast extraction of photo-generated charge carriers. The transient time of free carriers can be controlled by the thickness of the active layer, applied electrical bias, and the choice of interfacial charge transport materials.

The response speed is another important parameter for photodetectors. The measurement of our hybrid perovskite photodetector (PD3) was performed under a 550 nm pulse light from a light emitting diode. The rising and decay of the input pulse signal are

within a few nano seconds as calibrated by a single crystalline Si photodiode (Fig. 6.5a). To achieve sufficient light absorption, small leakage current, and fast response simultaneously, devices with a thickness of ~300 nm are found to be optimal. Devices with an active area of 0.1 and 0.01 cm^2 were measured. Fig. 5a shows the transient photocurrents of the devices measured under 0 bias at a light intensity of ~10 $\mu W\ cm^{-2}$ and at a pulse frequency of 100 kHz (photo response of the silicon diode is shown for comparison). The transient response results for the device with 0.01 cm^2 area shows a rise time (output signal changing from 0% to 70% of the peak output value) of 180 ns and a decay time of 160 ns. The rise time and decay time for a device with 0.1 cm^2 area are both ~600 ns. Fig. 5b shows the transient photocurrents at a pulse frequency of 1 MHz. Clearly, the small area device has rapid response rates and reaches ~ 80% of its maximum, whereas the response of the large area device is relatively slow. Fig. 6.5c shows the normalized response versus pulse frequency for the devices. The 3-dB bandwidth decreased from 2.9 MHz to 0.8 MHz when the device area increased from 0.01 to 0.1 cm^2, because the speed is related to the RC constant of the circuit. It is noted that the response speeds of our perovskite photodetectors presented here are faster than most of the organic, quantum dot, and hybrid photodetectors (typically on the order of millisecond)[4-10] and slightly slower than the silicon diode in Fig. 5a (≤20 ns). The speed is probably limited by the lower charge carrier mobility of the organic layer (PCBM, mobility ~ $10^{-3}\ cm^2\ V^{-1}s^{-1}$)[29], and the RC constant of the circuit[7]. When integrated into a circuit for real world applications, the pixel size should be much smaller and therefore, the response speed of the perovskite photodetectors is predicted to be much faster.

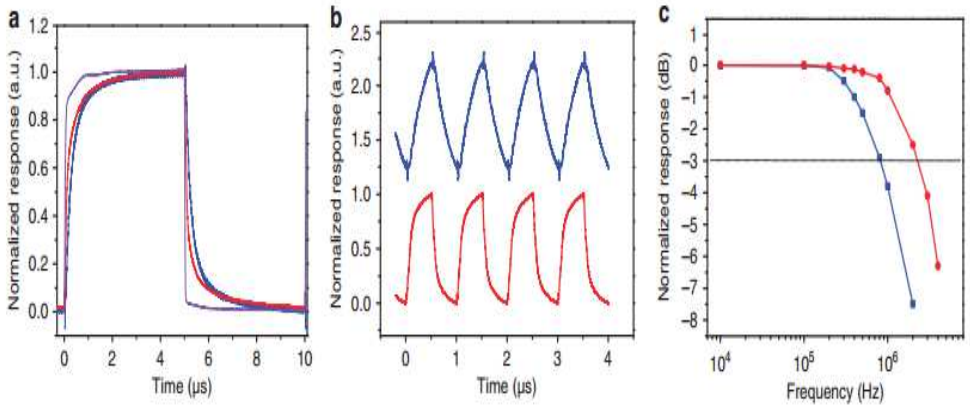

Figure 0-5 Transient photocurrent response of the photodetectors with different device areas. a, Transient photocurrent response at a pulse frequency of 100 kHz with a device area of 0.1 cm^2 (blue line) and 0.01cm^2 (red line). Transient photocurrent response of a silicon diode is shown for comparison. b, Transient photocurrent response at a pulse frequency of 1 MHz with a device area of 0.1 cm^2 (blue line) and 0.01cm^2 (red line). c, Frequency response of the photodetectors with a device area of 0.1 cm^2 (blue line) and 0.01cm^2 (red line).

Noise equivalent power is another important figure-of-merit for photodetectors. It represents the minimum impinging optical power that a detector can distinguish from the noise. It is equal to the reciprocal of D^* and can be expressed as

$$NEP = \frac{(Af)^{1/2}}{D^*} = \frac{i_n}{R} \quad (5)$$

To calculate *NEP* values for the hybrid perovskite photodetector (PD3), noise current of the devices were measured using a lock-in amplifier. The noise spectra at various frequencies are presented in Fig. 6.6a and the noise current plots at different dark current levels are shown in Fig. 6.6b. The noise current decreases at a higher frequency and increases at a larger reverse bias due to the larger dark current. The device shows small noise currents of less than 1 pA $Hz^{-1/2}$, which is about one order of magnitude smaller than that of a silicon diode[30]. The *NEP* of the photodetector is calculated to be 4.6×10^{-12} W at 550 nm (-100 mV, 3 kHz) and 4.2×10^{-12} W at 700 nm (-100 mV, 3 kHz). Very small noise

currents at low bias are key for achieving such small *NEP* values for the hybrid pervoskite photodetectors.

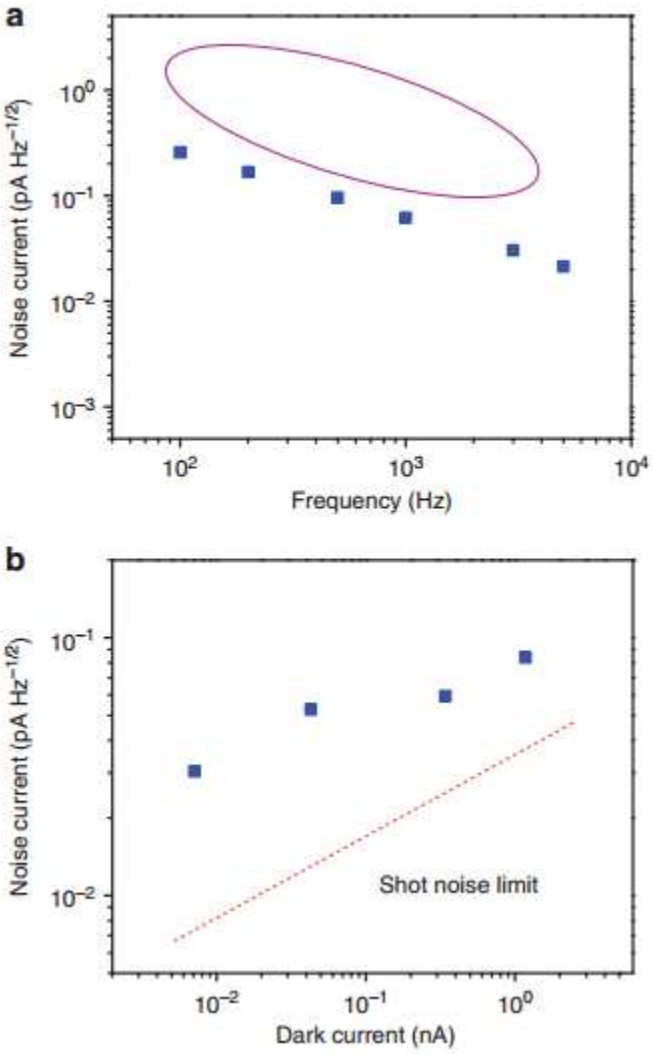

Figure 0-6 Noise current of the photodetectors. a,Measured dark current noise at different frequencies. The purple circle indicates reported values for a silicon photodiode. b, Measured dark current noise at different dark currents. The shot noise limit is also plotted for comparison.

6.3 Discussions and summary

The above results suggest the importance of designing device structure and selecting suitable interface materials for high photodetector performance. In order to

explore the effects of device architecture on the photodetector performance, we also fabricated devices with a "regular" structure: ITO/TiO_2/$CH_3NH_3PbI_{3-x}Cl_x$/p-doped spiro-MeOTAD/Au (PD4)[31]. The photovoltaic performance was found to be similar to the device reported here (~14% power conversion efficiency). However, we noticed that the response speed for such device is rather slow (Supplementary Figure 4). In the transient photocurrent measurements, the device showed a response time of ~30 ms, which is 10^5 times longer than that of the inverted device using PEDOT:PSS and PCBM as the interface materials. Such a low speed is probably due to the slow response of the interface materials, particularly the lithium salt-doped spiro-MeOTAD[31]. Moreover, it was observed that when working in the photovoltaic mode, our inverted device showed a weaker hysteresis effect in the forward bias region, compared to the regular device[31] (Supplementary Figure 5 for more details). The transient photocurrent response speed and the hysteresis effect may correlate with each other, suggesting that interface engineering is important for achieving high-speed photoresponse in photodetectors and minimizing hysteresis in photovoltaic cells. So far, the hysteresis effect in the pervoskite photovoltaics is still under debate, and according to our results and other literature reports; the interface contact and the charge transport layers are probably the key issues.

In summary, we have demonstrated solution-processed high performance photodetectors based on organic-inorganic hybrid $CH_3NH_3PbI_{3-x}Cl_x$ using an "inverted" device configuration. The performance parameters of these photodetectors are comparable to or even better than photodetectors fabricated from vacuum-processed inorganic materials. Such high performance can be attributed to the excellent intrinsic optical and electronic properties of the hybrid perovskite as well as the judicious interface design. We

believe that the hybrid pervoskite materials can be used in a variety of low-cost photodetector applications and our results should inspire new fundamental studies on the properties of such materials.

6.4 Experimental details

Materials. $PbCl_2$ was purchased from Alfa Aesar. [6,6]-phenyl-C_{61}-butyric acid methyl ester (PCBM) was purchased from Nano-C. PEODT:PSS solution was purchased from Clevios. Unless otherwise stated, all of the chemicals were purchased from Aldrich and used as received.

Device fabrication. The device architecture of the photodetector is shown in Fig. 1a. The pre-cleaned ITO substrates were treated with UV-ozone. A thin layer (~30 nm) of PEDOT:PSS (Baytron P VP A1 4083) was spin-coated onto the ITO surface which was pretreated by ultraviolet ozone for 15 min. After being baked at 150 ºC for ~ 10 min, the substrates were transferred into a nitrogen-filled glove box (< 0.1 ppm O_2 and H_2O). For the perovskite layer, $PbCl_2$ and CH_3NH_3I were dissolved in DMF in a 1:3 ratio. Specifically, the concentration of the $PbCl_2$ and CH_3NH_3I were 0.8 and 2.4 M. The solution was spin-coated onto the PEDOT:PSS layer at 800~2000 rpm (film thickness of 200 ~ 600 nm) and then annealed in air at 100 ºC (on a hot plate) for 1 h. After that, the devices were tranfered into a glove box and 2% PCBM in chlorobenzene solution was coated onto the perovskite layer at 1000 rpm. For PD1, the film was then transferred into a thermal evaporator that is located in the same glove box. For PD2, a thin layer of BCP (~ 5nm) was coated on the PCBM layer by thermal evaporation. For PD3, a thin layer of PFN (~ 5 nm) was coated on the PCBM layer by spin coating. The device fabrication was completed by thermal

evaporation of 100 nm Al as the anode under vacuum at a base pressure of 2×10^{-6} torr. The effective area of film was measured to be around 0.10 cm^2 or 0.010 cm^2 depending on the shadow mask that was used.

Current-voltage characterization. The fabricated devices were encapsulated in a nitrogen-filled glovebox by UV epoxy and cover glass. The current density-voltage curves were measured using an Agilent 4155C Semiconductor Parameter Analyzer. The devices were illuminated by monochromatic light from a light emitting diode (550 nm or 700 nm). The light intensity was controlled by varying the voltage on the light emitting diode. The actual light intensity was measured using a power meter. External quantum efficiencies were measured by an Enli tech (Taiwan) *EQE* measurement system.

Dark JV curve Analysis. Based on the solar cell equivalent circuit, the *J–V* characteristics are described by:

$$\mathrm{J} = J_0\left[\exp\left(\frac{e(V-JR_s)}{AK_BT}\right)-1\right]-J_{SC} \quad (1)$$

where J is the current flow through the external load, J_{SC} is the light induced current, (for the dark *J–V* fitting, $J_{SC}=0$). J_0 is the dark saturate current density, V is the applied voltage, A is the ideality factor, K_B is the Boltzmann constant, T is the temperature, and e is the electron charge. Equation (1) can also be written as $\frac{dV}{dJ}=\frac{AK_BT}{e}(J_{SC}+J)^{-1}+R_s$ and $\ln(J_{SC}+J)=\frac{e}{AK_BT}(V-R_SJ)+lnJ_0$. The J_0 can be obtained by fitting the curve of $\ln(J_{SC}-J)$ vs $(V+R_sJ)$, where the R_s is obtained by fitting the curve of dV/dJ *vs* $(J_{SC}+J)^{-1}$. The plot of dV/dJ vs $(J_{SC}+J)^{-1}$ and $\ln(J_{SC}+J)$ *vs* $(V- R_sJ)$ are shown in Fig. 2, respectively.

From linear fitting of Fig. 2, the device exhibited series resistance (~1. 57 Ω cm^2). By linear fitting the ln(J_{SC}+J) vs (V- $R_s$$J$) (Fig. 2), J_0 is calculated as 1.5×10^{-11} mA cm^{-2}.

Transient photocurrent measurements. A light emitting diode (550 nm) was modulated by the function generator as the excitation source. Square waves with different frequencies were applied. The photodetectors were directly connected to the oscilloscope (Tektronix DPO 4104) with an input impedance of 50 Ω.

Noise current measurements. Noise current was directly measured with a lock-in amplifier SR830. The photodetectors were kept in the dark room and shielded in Al foils during measurements.

6.5 References

1. Donati, S. Photodetectors: devices, circuits, and applications. Meas. Sci. Technol. **12**, 653 (2001).
2. Haugan, H. J. Study of residual background carriers in midinfrared InAs⁄GaSb superlattices for uncooled detector operation. Appl. Phys. Lett. **92**, 071102 (2008).
3. Rogalski, A., Antoszewski, J., Faraone, L. Third-generation infrared photodetector arrays. J. Appl. Phys. **105**, 091101 (2009).
4. Jin, Y. Z., Wang, J. P., Sun, B. Q., Blakesley, J. C. & Greenham, N. C. Solution-processed ultraviolet photodetedtors based on colloidal ZnO nanoparticles. Nano Lett. **8**, 1649 (2008).
5. Sukhovatkin, V., Hinds, S., Brzozowski, L. & Sargent, E. H. Colloidal quantum-dot photodetectors exploiting multiexciton generation. Science **324**, 1542 (2009).
6. Guo, F. et al. A nanocomposite ultraviolet photodetector based on interfacial trap-

controlled charge injection. Nat. Nanotech. **7**, 798 (2012).

7. Yao, Y. et al. Plastic Near-Infrared Photodetectors Utilizing Low Band Gap Polymer. Adv. Mater. **19**, 3979 (2007).
8. Chen, H. Y., Lo, M. K., Yang, G., Monbouquette, H. G., & Yang, Y. Nanoparticle-assisted high photoconductive gain in composites of polymer and fullerene. Nat. Nanotech. **3**, 543 (2008).
9. Gong, X. et al. High-Detectivity Polymer Photodetectors with Spectral Response from 300 nm to 1450 nm. Science **325**, 1665 (2009).
10. Arnold, M. S. et al. Broad spectral response using carbon nanotube/organic semiconductor/C60 photodetectors. Nano Lett. **9**, 3354 (2009).
11. Kagan, C. R., Mitzi, D. B. & Dimitrakopoulos, C. D. Organic-inorganic hybrid materials as semiconducting channels in thin-film field-effect transistors. Science **286**, 945 (1999).
12. Kojima, A., Teshima, K., Shirai, Y. & Miyasaka, T. Organometal halide perovskites as visible-light sensitizers for photovoltaic cells. J. Am. Chem. Soc. **131**, 6050 (2009).
13. Lee, M. M., Teuscher, J., Miyasaka, T., Murakami, T. N. & Snaith, H. J. Efficient hybrid solar cells based on meso-superstructured organometal halide perovskites. Science **338**, 643 (2012).
14. Heo, J. H. et al. Efficient inorganic–organic hybrid heterojunction solar cells containing perovskite compound and polymeric hole conductors. Nature Photon. **7**, 487 (2013).
15. Chen, Q. et al. Planar Heterojunction Perovskite Solar Cells via Vapor-Assisted Solution Process. J. Am. Chem. Soc. **136**, 622 (2014).
16. Burschka, J. et al. Sequential deposition as a route to high-performance perovskite-

sensitized solar cells. Nature **499**, 316 (2013).

17. Liu, M., Johnston, M. B. & Snaith, H. J. Efficient planar heterojunction perovskite solar cells by vapour deposition. Nature **501**, 395 (2013).
18. Liu, D. & Kelly, T. L. Perovskite solar cells with a planar heterojunction structure prepared using room-temperature solution processing techniques. Nature Photon. **8**, 133 (2014).
19. Stranks, S. D. et al. Electron-hole diffusion lengths exceeding 1 micrometer in an organometal trihalide perovskite absorber. Science **342**, 341 (2013).
20. Xing, G. et al. Long-range balanced electron- and hole-transport lengths in organic–inorganic $CH_3NH_3PbI_3$. Science **342**, 344 (2013).
21. Stoumpos, C. C., Malliakas, C. D. & Kanatzidis, M. G. Semiconducting Tin and Lead Iodide Perovskites with Organic Cations: Phase Transitions, High Mobilities, and Near-Infrared Photoluminescent Properties. Inorg. Chem. **52**, 9019 (2013).
22. Takahashia, Y., Hasegaw, H., Takahashia, Y. & Inabe, T. Hall mobility in tin iodide perovskite $CH_3NH_3SnI_3$: Evidence for a doped semiconductor. J. Solid State Chem. **205**, 39 (2013).
23. Yin, W.-J., Shi, T. & Yan, Y. Unique Properties of Halide Perovskites as Possible Origins of the Superior Solar Cell Performance. Adv. Mater. DOI: 10.1002/adma.201306281 (2014).
24. You, J. et al. Low-Temperature Solution-Processed Perovskite Solar Cells with High Efficiency and Flexibility. ACS Nano **8**, 1674 (2014).
25. Ikai, M. et al. Highly efficient phosphorescence from organic light-emitting devices with an exciton-block layer. Appl. Phys. Lett. **79**, 156 (2001).

26. He, Z. C. et al. Simultaneous enhancement of open-circuit voltage, short-circuit current density and fill factor in polymer solar cell. Adv. Mater. **23**, 4636 (2011).
27. Hegedus, S. S., & Shafarman, W. N. Thin-film solar cells: device measurements and analysis. Progress in Photovoltaics: Research and Applications **12**, 155 (2004).
28. Snaith, H. J. Perovskites: The Emergence of a New Era for Low-Cost, High-Efficiency Solar Cells. J. Phys. Chem. Lett. **4**, 3623 (2013).
29. Mihailietchi, V. D. et al. Electron Transport in a Methanofullerene. Adv. Funct. Mater. **13**, 43 (2003).
30. Malik, S., Ray, A. K. & Bruce, S. 1/f noise in Langmuir–Blodgett films on silicon. Semicond. Sci. Technol. **20,** 453 (2005).
31. Snaith, H. J. et al. Anomalous Hysteresis in Perovskite Solar Cells. J. Phys. Chem. Lett. **5**, 1511 (2014).